Discovery, Selection and Evaluation of Fast Lithium Ionic Conductors Through *Ab Initio*-Based Computational Methods and Materials Informatics

January 2014

Randy Jalem

Table of Contents

Chapter 1. Introduction

1-1. Fast lithium ionic conductors for all solid state lithium batteries

The next generation of lithium-based energy conversion and storage technologies has been recognized by consensus as being critically dependent on the progress and development in the field related to one particular group of solid state ionic materials: the fast lithium ionic conductors. They are the key towards meeting the ever increasing performance demands of today's market, the mass production of commercial plug-in hybrid electric vehicles and hybrid electric vehicles, and the maximum utilization of clean energy sources. These materials, in the simplest description, have or can contain lithium (Li) ions and allow for significant diffusion of Li ions in their crystal structure at room or low temperature. From a historical perspective, the first successful commercial breakthrough for fast Li ion conduction could be ascribed to Sony Corporation (year 1991) with their high-voltage (around 3.7 V) and high-energy Li_xC_6/non-aqueous liquid electrolyte/$LiCoO_2$ cell [1]. In this set-up, Li is extracted and inserted during charge and discharge process, respectively, within the intercalation cathode $LiCoO_2$. Many commercial batteries now still use $LiCoO_2$ as the cathode component while other compositions include that of Ni and Mn analogues [2], stabilized spinel $LiMn_2O_4$ [3], and olivine-type $LiFePO_4$ [4]. For the anode, the latest high capacity materials are composed of carbon nanostructures with designed morphology such carbon nanotubes [5], carbon nanofibers [6], graphenes [7], and their composites [8-10].

A schematic diagram of the working principles of a Li ion battery is shown in Figure 1-1. As shown, Li ions are shuttled between the cathode and the anode via the electrolyte; the latter functions both as an electronic insulator and an ionic conductor. During a charge process, an external potential is applied, forcing Li ions to migrate from the cathode where the chemical potential is relatively lower, passing through the electrolyte, and ending up at the anode where the chemical potential is higher. For the discharge process, the circuit is closed and Li ions migrate spontaneously from the anode and again through the electrolyte, and then back into the cathode. At the same

time, an external work can be performed (eg. lighting a bulb) as electrons travel through the external circuit during this stage.

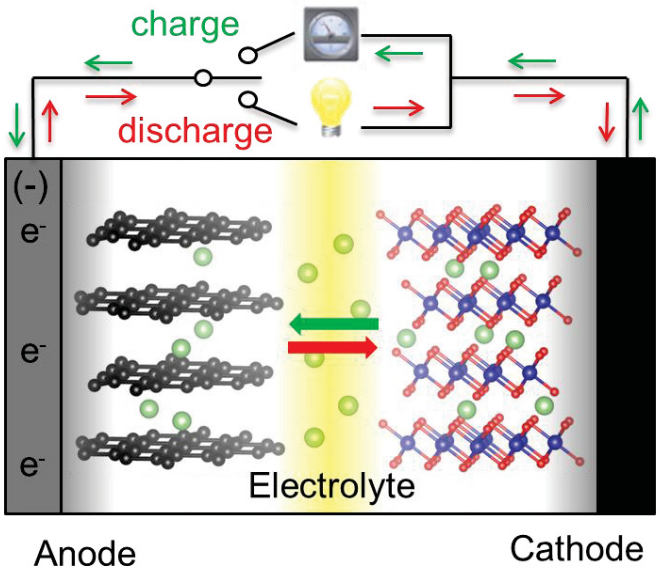

Figure 1-1. A schematic illustration of the working principles of a Li_xC_6 / Electrolyte / $Li_{1-x}CoO_2$ Li ion battery.

Another crucial fast ionic conductor component being mentioned for a working battery is the electrolyte which separates the cathode and the anode and essentially restricts electronic conduction to prevent the battery from short circuiting. In a conventional set-up, this component is based on solutions of one or more Li salts such as $LiPF_6$, $LiBF_6$, and $LiClO_4$ that are dissolved in organic solvents such as ethylene carbonate, dimethyl carbonate, diethyl carbonate [11]. These electrolytes have excellent Li ionic conductivity which can reach on the order of 10^{-2} S/cm. However, it is recognized that such electrolytes are prone to combustion, difficult to miniaturized, and can pose serious environmental concerns if not properly disposed or recycled. Thus, efforts have been focused on replacing them with solid-type electrolytes which can address the aforementioned issues. The resulting battery set-up is often referred to as an all solid state Li ion battery. Unfortunately, there are a number of disadvantages that needs to be solved as well before commercialization. Examples of promising solid electrolytes that have been reported so far, including their limiting factors, are listed in Table 1-1.

Table 1-1. Reported potential solid electrolytes, their Li ionic conductivity, and limiting factors.

Composition	$\sigma_{bulk,300\ K}$ (S/cm)	Limiting factors	Reference
Li-βAl_2O_3	3×10^{-3}	Highly hygroscopic, difficult to prepare as pure phase	Yao et al., 1967 [12]
Li_3N	10^{-3}	Very low decomposition voltage (0.44 V)	Alpen et al., 1977 [13]
$Li_{14}Zn(GeO_4)_4$ (LISICON)	2×10^{-6}	Highly reactive with Li metal, atmospheric CO_2, conductivity decreases with time	Hong, 1978 [14]
$Li_{1.3}Al_{0.3}Ti_{1.7}(PO_4)_3$	7×10^{-4}	Unstable with Li metal (Ti^{4+} reduction)	Aono et al., 1989 [15]
$Li_{0.35}La_{0.55}TiO_3$ (LLT)	1×10^{-3}	Unstable with Li metal (Ti^{4+} reduction), high T preparation, high loss of Li_2O, variance of conductivity with Li concentration, difficulty of controlling Li content	Inaguma et al., 1993 [16]
$Li_{2.9}PO_{3.3}N_{0.46}$ (LiPON)	2×10^{-6}	Moderate conductivity, used in development of thin film battery, prepared using sputtering method in situ	Bates et al., 1993 [17]
$Li_{3.25}Ge_{0.25}P_{0.25}S_4$ (Thio-LISICON)	2.2×10^{-3}	Low electronic conductivity of sulfur prevents a close contact with electrode.	Kanno et al., 2001 [18]
$0.7Li_2S$-$0.3P_2S_5$ glass-ceramics	3.2×10^{-3}	Extremely hydroscopic, reacts with water	Mizuno et al., 2005 [19]
Garnet-type $Li_6BaLa_2Ta_2O_{12}$	4×10^{-5}	Conductivity is not sufficient though stable against Li metal, moisture, and air	Thangadurai et al., 2005 [20]
Garnet-type $Li_7La_3Zr_2O_{12}$	2.44×10^{-4}	High polarization potential	Murugan et al., 2007 [21]
$Li_{10}GeP_2S_{12}$	1.20×10^{-2}	High cost of Ge, air and moisture sensitivity	Kamaya, et al., 2011 [22]

1-2. Search for new fast Li ionic conductors: present issues and challenges

New material discovery in the field of materials science, in general, is still largely driven by significant trial-and-error. Oftentimes, it takes years of research efforts to identify a suitable material for an intended application and optimize it for commercial use. The battery field is no exception to this and progress has been indeed slow due to the vast combinatorial space of chemistries involved in materials design. So far, reported experimental data for fast Li ionic conductors are usually dispersed in the literature and studies have only been able to survey limited search spaces and thus, opportunities for leveraging on them have become very limited.

Efforts to consolidate material information into databases for the benefit of the whole materials community have been done in order to accelerate new materials search and materials design. Two of the well-established resources so far are the crystallographic and thermochemical databases. The former is considered as the basis for crystal structure data interpretation of metals, alloys, and inorganic materials while the latter is a compilation of fundamental thermochemical data such as heat capacity and calorimetric information. The Inorganic Crystal Structure Database (ICSD), for example, contains 161,030 crystal structures as of April 2013 and its entries are mostly reported in journals, only a few are sourced from private communications [23]. However, the thermochemical database, which covers physical and chemical property data, still lags behind massively as compared to the crystallographic database. One dataset, the National Institute of Standards and Technology-Joint Army Navy Air Force (NIST-JANAF) Thermochemical Tables, has only about 1800 entries and already includes both inorganic and organic substances [24]. This large discrepancy presents both a challenge and opportunity for battery researchers.

It would be greatly beneficial if materials can be tested accurately and reliably *in silico* in order to fill gaps in the search space, or beforehand in order to provide informed choices for experimentalists. Computational modeling such as by *ab initio*-based methods can potentially address the issue at hand, as important materials properties can now be predicted with sufficient accuracy (detailed description is available in the Appendix section) [25-29]. Recently, a number of initiatives has been deployed for such a purpose and is now encountering a considerable number of successes. One of these initiatives is the U.S. Materials Genome Initiative, of which the database component called Materials Project has now a total of 34,158 materials; 15,355 of which have their band structures calculated, and 16,016 and 443 of which are identified for conversion and intercalation battery application, respectively [30]. Figure 1-2 shows the number of compounds available on the Materials Project sorted out

according to compound type. The data collection in this database has been derived by using high-throughput computation and latest information age techniques. In this respect, one issue that becomes apparent is that solving material properties of a given material by using *ab initio* codes usually requires several hundreds of central processing unit (CPU) – hours. The solution employed for this is the construction of a massive computational infrastructure and because of this, computations that predict, screen, and optimize materials are made possible at an unparalleled scale and rate. Other issues on the use of *ab initio*-based methods at the core of database construction are the bottleneck processes during its implementation. Some of these include: i.) assessment of target properties that typically involves sequential computation schemes that use output from preceding steps as input in order to proceed, ii.) recurrent failed convergence that needs recalculations with modified convergence parameters, and iii) calculations that inherently requires large SCF iterations for convergence. The problem related to computational time is much more magnified, especially when working with infrastructures of limited or modest computational power, just like as in most research groups nowadays.

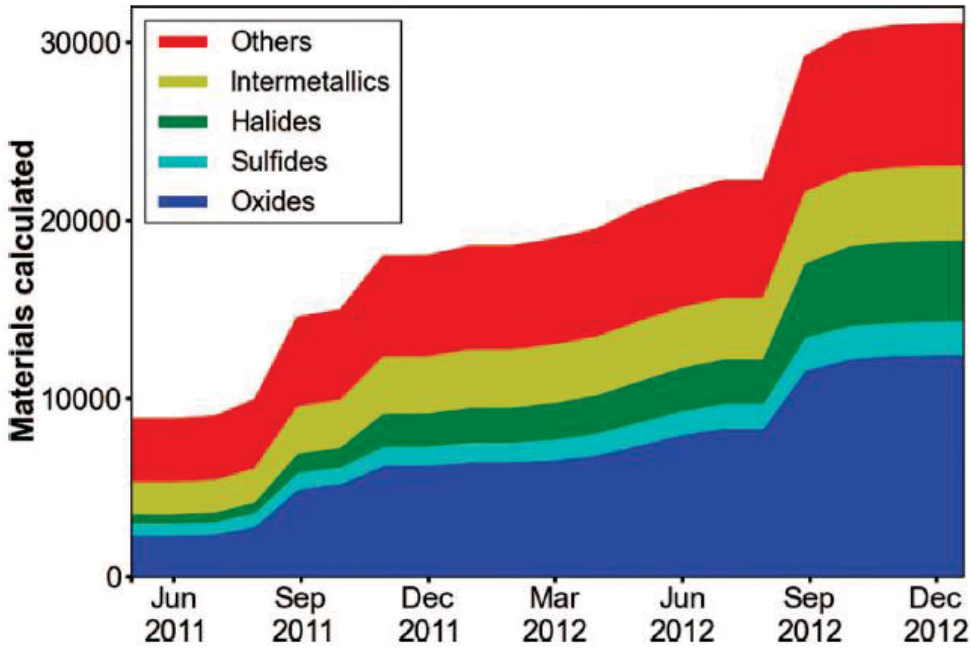

Figure 1-2. Number of calculated materials in Materials Project since its initial release in October 2011.

1-3. Search for new fast Li ionic conductors: related computational strategies

The current challenge in predicting new compounds by computation is actually what to calculate, i.e., the chemical compositions that will likely form compounds and signify enough merit for further investigation. Computational exploration of chemical search spaces using mathematical schemes has been attempted in the past. One study in particular, which presented a way of predicting structures for alloys, outlined a general approach for constructing an informatics-based structure suggestion model based from rigorously mined correlations embodied within experimental data which are in turn used to direct *ab initio*-based methods towards finding stable crystal structure of materials [31]. The approach, formally termed as Data Mining Structure Predictor (DMSP) modeling, used a database of 28,457 entries of experimentally determined structure types in 2,600 binary alloys. Figure 1-3 illustrates the concept view for predicting the structure of a sample target composition $AgMg_3$. First, information is collected for reported structures including additional information for compositions AgMg and Ag_3Mg. This evidence **e** is then used to query the DMSP model to generate a list of ranked candidate structures as shown in Figure 1-3a. To verify the prediction, the formation enthalpies of the top 10 structures and most common reported structures are calculated and compared as displayed in Figure 1-3b. Another similar work followed which focused on large-scale search of new ternary oxides in the $A_xB_yO_z$ system; there were 209 new ternary compounds discovered in the said study [32]. The results are summarized in Figure 1-4, in which the new compounds are shown to be distributed across different chemistries.

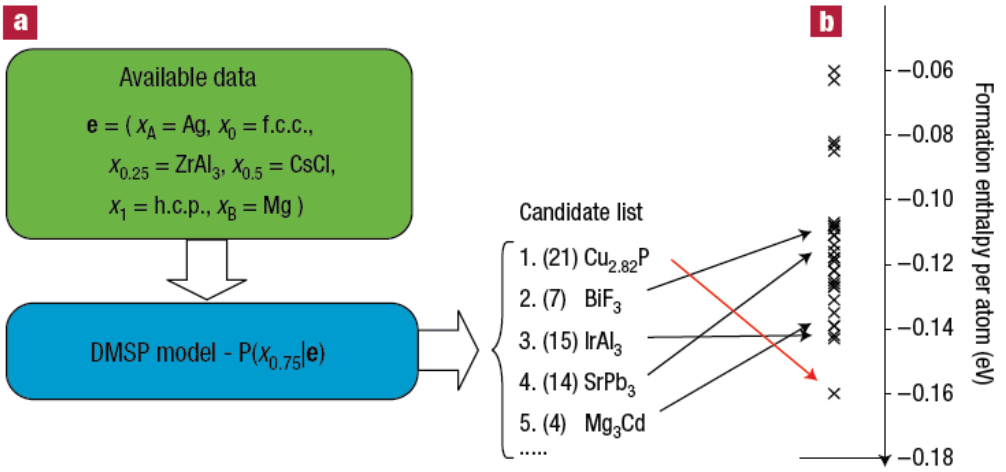

Figure 1-3. (a) Data Mining Structure Predictor (DMSP) modeling for $AgMg_3$ compound on the basis of the limited data available at other compositions (green box). (b) *Ab initio*-derived formation enthalpy of candidate structures are plotted to aid in prediction verification.

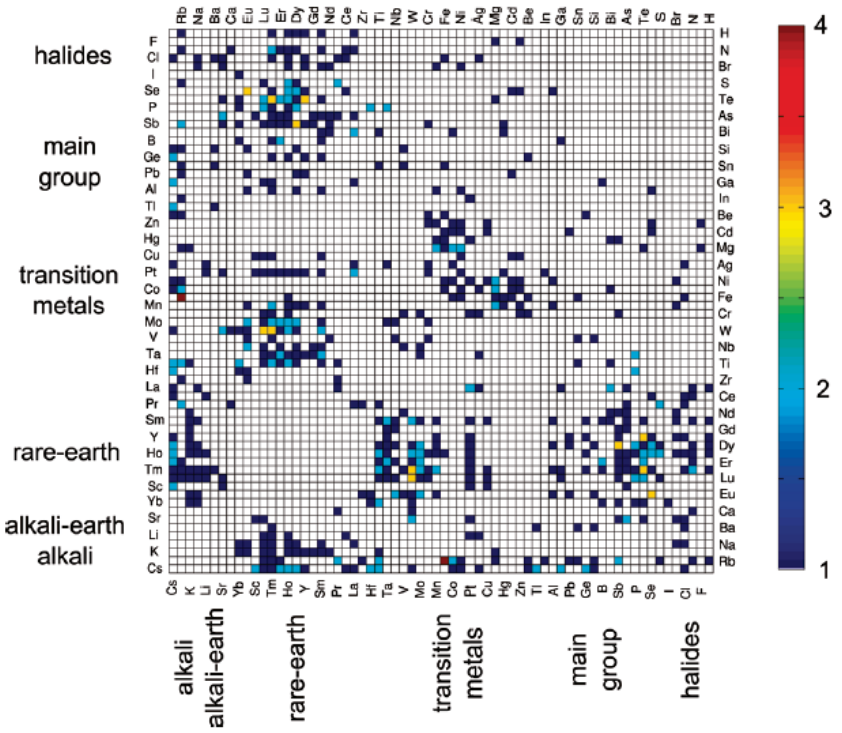

Figure 1-4. Distribution of new compounds across chemical classes. The plot here indicates the number of new compounds discovered in the A-B-O system. Elements are sorted according to their Mendeleev number in order to easily spot different chemical classes.

For battery materials, few calculations for new materials search and evaluation have been conducted in a targeted manner on existing crystal structures. An example of these is the investigation on the electrochemical stability and Li^+ conductivity of the $Li_{10\pm1}MP_2X_{12}$ (M = Ge, Si, Sn, Al or P, and X = O, S or Se) family of fast ionic conductors [33]. All the compositions were calculated by *ab initio* method in the DFT framework. It was aimed at addressing two key limitations of the composition with reported high ionic conductivity ($Li_{10}GeP_2S_{12}$ [34]), namely: the high cost of one of the elemental constituent (Ge) and the air and moisture sensitivity. Another study explored the materials stability within the tavorite search space for cathode application [35]. The relative stabilities of the different compositions are shown in Figure 1-5. The plot predicts which materials pass the thermodynamic stability screen, will not release O_2 at room temperature, and will insert lithium at >1 V vs. Li metal. Meanwhile, yet another published paper has succeeded in using both *ab initio*-based high throughput screening and systematic experimental validation to evaluate a novel alkali carbonophosphate family of compounds as cathodes [36]. This kind of study is especially desired because ultimately, predictions should be proven by experiment and is the only way to make tangible advancements in the field. The effort was able to synthesized seven new compositions with the general formula $Na_3M(PO_4)(CO_3)$ (M = Mg, Mn, Fe, Co, Ni, Cu, Sr) that were predicted first by computations.

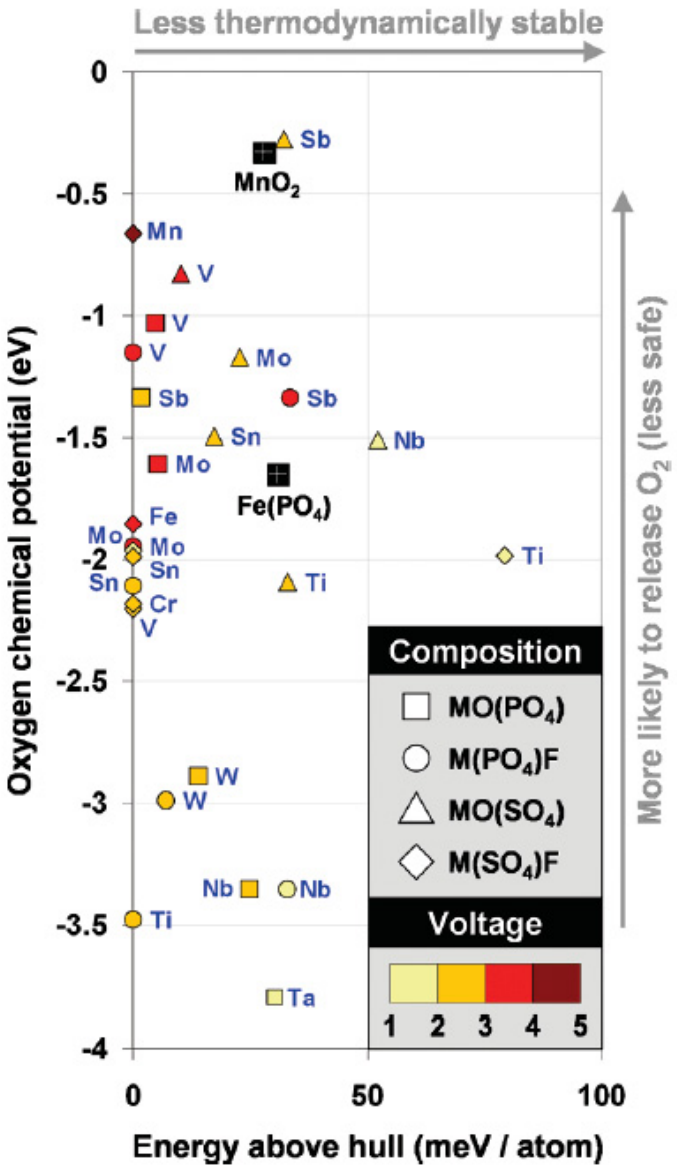

Figure 1-5. Energy relative to the thermodynamic hull and oxygen chemical potential for fully delithiated tavorite materials. The plotted materials pass the thermodynamic screen, are not predicted to release O_2 at room temperature, and are predicted to insert Li at >1 V vs. Li metal. The chemical composition is indicated by the symbol shape, with the redox-active metal labeled at the individual data points. The colors indicated the voltage at which Li is predicted to be inserted vs. Li metal. Spinel MnO_2 and olivine $FePO_4$ are added for reference.

1-4. An emerging paradigm for new battery material discovery and selection

It is not until in recent years that the field of Li ion battery has started taking advantage of *ab initio*-based computations in guiding new materials search or rationalizing data from experimental measurements. It is still greatly underutilized and is yet to gain momentum in its application. When large-scale computational data is combined and made in close collaboration with experiments, a comprehensive strategy for new battery material discovery and selection can be realized that can drive a new paradigm shift in the field. This so-called paradigm shift is shown in Figure 1-6 and can be explained in a path diagram involving material composition, structure, and properties.

The path for relating from structure to property (in black) has been realized in many instances by traditional experiments and simulations. This path is what forms the bottleneck and is allocated with the bulk of the research cost and time resource. Similarly, the path for relating from structure to composition (in black), which has been done through combinatorial experiments, is also characterized by the same issues.

Meanwhile, a new component which can revolutionize materials investigation is the composition-to-structure path (in violet) which mainly relies on computational crystal structure prediction. At present, this path is considered as one of the continuing scandals in the physical sciences and it still remains in general impossible to predict the structure of even the simplest crystalline solids from a knowledge of their chemical composition [37]. With the increasing computational power of computers, this problem is supposed to be solvable now, in which ideally one can simply type in the formula of the chemical and obtain the atomic coordinates of the atoms in a unit cell as output. However, this case is still debatable. The composition-to-structure path, if solved in a brute force manner in which ideally all possible solutions are evaluated per composition, will be severely limited by the available computational hardware as one will have to wrestle with the “curse of dimensionality” especially when the scope is extended to a large number of atoms [38]. Essentially, minimum energy structure search can be imagined as a complex problem related to crystal structure prediction, i.e., finding the most stable (lowest free energy) structure for a given chemical composition at given external conditions (such as pressure and temperature). This involves the evaluation of a very large number of possible distinct crystal structures C defined by the combinatorial

space:

$$C = \binom{V/\delta^3}{N} \prod_i \binom{N}{n_i} \quad (1\text{-}15)$$

where N is the total number of atoms in the unit cell of volume V, δ is a relevant discretization parameter (eg., 1 Å) and n_i is the number of atoms of *i*th type in the cell. Considering the dimensionality of the energy landscape:

$$d = 3N + 3 \quad (1\text{-}16)$$

where $3N - 3$ degrees of freedom are the atomic positions and the remaining six dimension are lattice parameters. Clearly, this global optimization problem is high-dimensional, and simple exhaustive search strategies are undoubtedly unfeasible. A pragmatic approach for this is the use of systematic and efficient optimization and search methods to survey and find local and global basins in the energy landscape of crystal structures. Knowledge of these low energy structures allows one to predict plausible reaction paths and eventually construct phase diagrams that can be used to design materials without relying on experimental input. An example of a search method that is currently employed in the field of materials science is the metadynamics approach [39]. The concept is illustrated in Figure 1-7 wherein the free energy surface (**FES**) is constructed in a set of generalized coordinates **h** (distances, lattice vectors, coordination number, energy, etc) and the search is biased by a history-dependent potential constructed as a sum of Gaussians centered along the trajectory of **h**. The driving force for evolving **h** is derived from $\mathbf{F} + \mathbf{F_g}$, where **F** is the thermodynamic driving force while $\mathbf{F_g}$ comes from a potential constructed as a superposition of Gaussians and is used to penalized a visited configuration from being sampled again. The crossing of the saddle point is detected when $\mathbf{F} \| \mathbf{F_g}$. This method appears to be reasonable enough, but one of its current limitations is the selection of order parameter that will effectively and universally describe the energy landscape of any given system.

Another new component is the multi-directional path for composition, structure, and property which can now be potentially explored using materials informatics. Another facet of the "curse of dimensionality" is encountered when one is trying to visualize a high dimensional materials-related function or data set in which sparsity increases exponentially given a fixed amount of data points. The human brain can only process this high dimension of variables, associations, and data structures in a very limited way and thus, many useful correlations, patterns, and structures embedded in large databases are often easily overlooked and unrecognized. Materials informatics can

process these data into human readable form and can do this efficiently through the use of latest computational algorithms and statistical techniques [40]. The insights collected in this procedure can then be leveraged for designing new materials. Figure 1-8 shows the simplified schematic diagram of how materials informatics can be implemented for knowledge discovery. First, the original data collected from experimental measurements or theoretical simulations are warehoused and organized in databases. Second, a database is then accessed for extraction of data features that are related to the material property or properties of interest. Third, the extracted data are analyzed statistically for pattern recognition. Fourth, the data are further transformed using visualization tools according to the patterns or trends that were identified. Then, the transformed data are subjected to physical interpretation based on well-founded theories and chemical intuition and then validated through experiments. Thereafter, the acquired knowledge is tested and validated through experimentation and computation. The database is then updated with the new collected data. This leads to an iterative cycle where in every cycle, it is possible to get new information.

Table 2 summarizes the present merits and demerits of conventional structure-to-composition path-based, composition-to-structure path-based and property-to-composition (structure) path-based new materials searches. In this thesis work, solutions to the listed demerits for composition-to-structure and property-to-composition (structure) paths are suggested and demonstrated by combining *ab initio* calculation with sophisticated search or optimization techniques as well as materials informatics.

Table 2. Comparison of merits and demerits between the conventional and this study's proposed approaches for materials search.

	Merit	Demerit
Structure-to-composition path (conventional)	Availability of information in existing structural databases	Limited availability of information in existing property databases
Composition-to-structure path (this study)	Systematic search can be done for true novel materials or chemistries without relying on initial assumptions	The free energy surface of possible crystal structures that needs to be evaluated has exceedingly many dimensions Sophisticated and efficient search and optimization techniques are needed to evaluate the free energy landscape
Property-to-composition path (this study)	Highly efficient when performed against computational data Useful insight for material design Patterns or trends from high-dimensional data that would have been missed by the human brain can be extracted and analyzed systematically	Limited availability of information in existing property databases Experimentally derived data requires careful evaluation as the quality varies from one source to another, this could lead to a significant noise in the material property-based data trends or patterns Sophisticated and efficient data mining or machine learning tools are needed

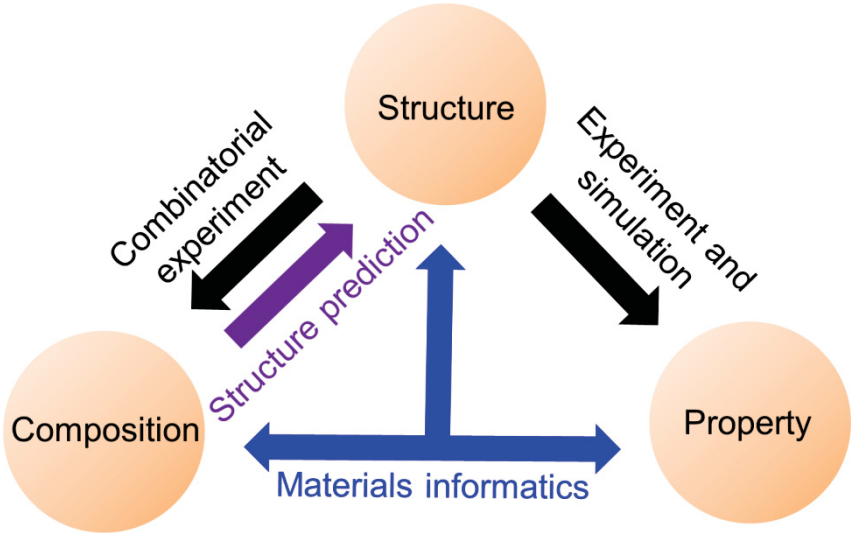

Figure 1-6. An emerging paradigm for the acceleration of battery materials discovery, selection, and evaluation.

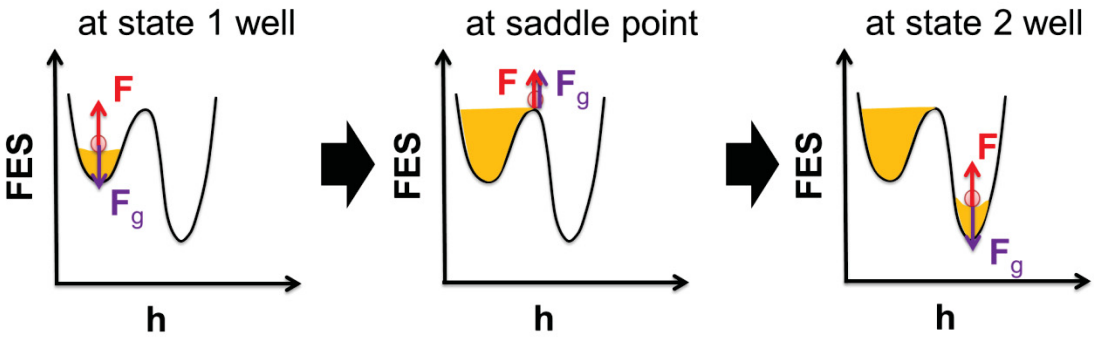

Figure 1-7. The trajectory of a metadynamics simulation generated using coordinate variables **h**.

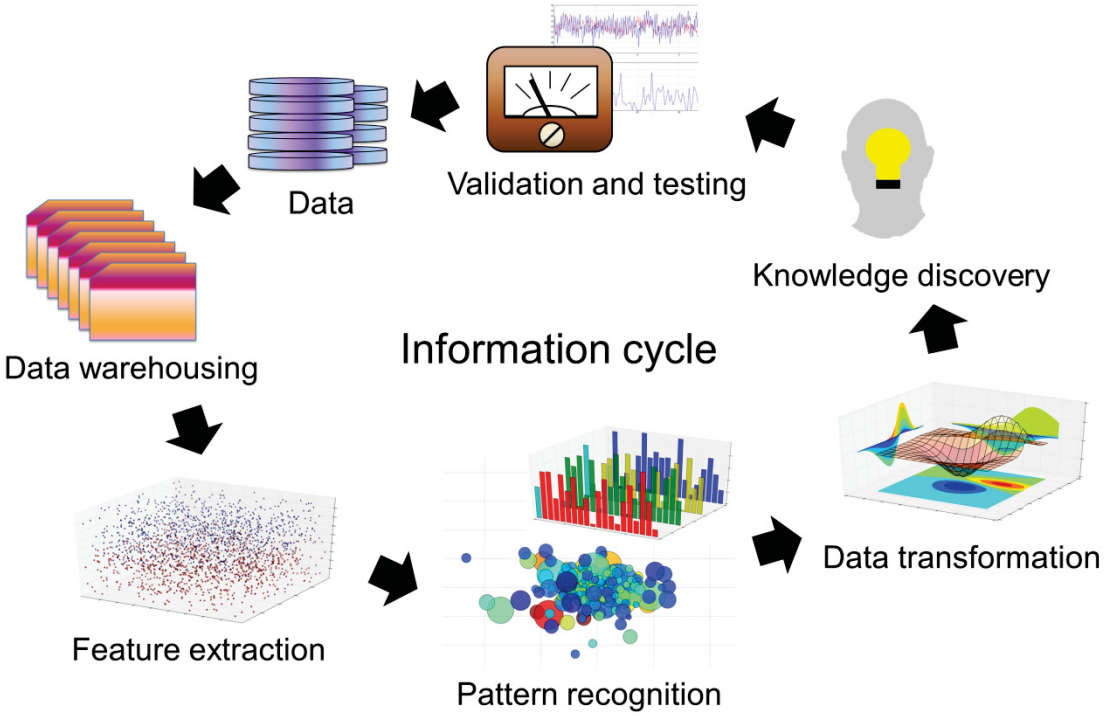

Figure 1-8. The cycle chart of an informatics driven materials science aimed towards knowledge discovery.

1-5. Aim of this thesis

As mentioned in the preceding section, crystal structure prediction and materials informatics are the two new concepts that offer new ways of discovering, selecting, and evaluating reported or new materials in a high throughput fashion or in a targeted manner. However, their widespread use is yet to be seen and still very little is known as to the details of how to apply them for specific problems in the battery field. One of the major reasons is that only few reports that demonstrate their use and effectiveness is available in the literature, particularly in areas of new battery materials search and materials screening. In order to encourage the battery community, there is a need to investigate and clearly outline not only the latest and relevant state of the art schemes and algorithms for crystal structure prediction and materials informatics but as well as establish a clear procedure on how to gain useful information from large scale computational data and use them in order to aid experiments.

The ultimate goal of this thesis is to develop comprehensive solutions derived from latest computational and statistical techniques to address two of the crucial high-dimensional problems in new battery materials discovery, selection and evaluation, namely,: i.) assessment of the thermodynamic stability of materials and ii) target property-driven evaluation of large chemical search spaces. By applying *ab initio*-based computational methods and materials informatics, this study will, respectively,: i.) predict thermodynamically stable crystal structures from starting chemical compositions by an evolutionary-based search method (which will be describe in the succeeding relevant section) and ii) efficiently screen a large chemical search space by building robust prediction models for a given target material property. The study will establish a clear framework for the aforementioned goals and will be demonstrated by the following topics:

1. *Ab initio*-based evolutionary algorithm search of global minimum energy structures in the chemical search space of Li_xCoO_2 intercalation cathode material; and
2. Multivariate method-assisted *ab initio* study of olivine-type $LiMXO_4$

(M^{2+}-X^{5+}, M^{3+}-X^{4+}) and tavorite-type $LiMXO_4F$ (M^{2+}-X^{6+}, M^{3+}-X^{5+}) potential solid electrolyte materials.

1-6. Chapter references

1. M. M. Thackeray, C. Wolverton and E. D. Isaacs, Energy Environ. Sci. 2012, 5, 7854.
2. N. Yabuuchi and T. Ohzuku, J. Power Sources 2003, 119, 171.
3. R. J. Gummow, A. de Kock and M. M. Thackeray, Solid State Ionics 1994, 69, 59.
4. A. K. Padhi, K. S. Nanjundaswamy and J. Goodenough, J. Electrochem. Soc. 1997, 144, 1188.
5. X. X. Wang, J. N. Wang, H. Chang and Y. F. Zhang, Adv. Funct. Mater. 2007, 17, 3613.
6. S. H. Murayama, G. Z. Zhuang, H. Y. Wang, T. Fukutsuka, K. Miyazaki and T. Abe, Carbon 2013, 57, 539.
7. E. J. Yoo, J. Kim, E. Hosono, H. S. Zhou, T. Kudo and I. Honma, Nano Lett. 2008, 8, 2277.
8. J. Zhang, Y. S. Hu, J. P. Tessonnier, G. Weinberg, J. Maier and R. Schogl, Adv. Mater. 2008, 20, 1450.
9. Z. J. Fan, J. Yan, T. Wei, G. Q. Ning, L. J. Zhi and J. C. Liu, ACS Nano 2011, 5, 2787.
10. B. Guo, X. Wang, P. F. Fulvio, M. Chi, S. M. Mahurin and X. G. Sun, Adv. Mater. 2011, 23, 4661.
11. K. Xu, Chem. Rev. 2004, 104, 4303.
12. Y. –F. Y. Yao and J. T. Kummer, J. Inorg. Nucl. Chem. 1967, 29, 2453.
13. U. von Alpen, A. Rabenau and G. H. Talat, App. Phys. Lett. 1977, 30, 621.
14. H. Y. P. Hong, Mater. Res. Bull. 1978, 13, 117.
15. H. Aono, H. Imanaka and G. Y. Adachi, Acc. Chem. Res. 1994, 27, 265.
16. Y. Inaguma, C. Liquan, M. Itoh, T. Nakamura, T. Uchida, H. Ikuta and W. Wakihara, Solid State Commun. 1993, 86, 689.
17. J. B. Bates, N. J. Dudney, G. R. Gruzalski, R. A. Zuhr, A. Choudhury and C. F. Luck, J. Power Sources 1993, 43-44, 103.
18. R. Kanno and M. Murayama, J. Elec. Soc. 2001, 148, A742.

19. F. Mizuno, A. Hayashi, K. Tadanaga and M. Tatsumisago, Adv. Mater. 2005, 17, 918.
20. V. Thangadurai and W. Weppner, Ionics 2006, 12, 81.
21. R. Murugan, V. Thangadurai and W. Weppner, Angew. Chem. Int. Ed. 2007, 46, 7778.
22. N. Kamaya, K. Homma, Y. Yamakawa, M. Hirayama, R. Kanno, M. Yonemura, T. Kamiyama, Y. Kato, S. Hama, K. Kawamoto and A. Mitsui, Nat. Mater. Lett. 2011, 10, 682.
23. ICSD, Inorganic Crystal Structure Database; http://icsd.fizkarlsruhe.de/icsd/, 2013.
24. M. Chase, NIST-JANAF Thermochemical Tables, 4th Edition, 1998.
25. D. –H. Seo, H. Kim, H. Kim, W. A. Goddard III and K. Kang, Energy Environ. Sci. 2011, 4, 4938.
26. Y. Mo, S. P. Ong and G. Ceder, Chem. Mater. 2012, 24, 15.
27. G. Ceder, G. Hautier, A. Jain and S. P. Ong, MRS Bull. 2011, 26, 185.
28. K. Kang, Y. S. Meng, J. Bréger, C. P. Grey and G. Ceder, Science 2006, 311, 977.
29. Y. S. Meng, Y. W. Wu, B. J. Hwang, Y. Li and G. Ceder, J. Electrochem. Soc. 2004, 151, A1134.
30. A. Jain, S. P. Ong, G. Hautier, W. Chen, W. D. Richards, S. Dacek, S. Cholia, D. Gunter, D. Skinner, G. Ceder and K. A. Persson, Apl. Materials 2013, 1, 011002.
31. C. C. Fischer, K. J. Tibbetts, D. Morgan and G. Ceder, Nat. Mater. 2006, 5, 641.
32. G. Hautier, C. C. Fischer, A. Jain, T. Mueller and G. Ceder, Chem. Mater. 2010, 22, 3762.
33. S. P. Ong, Y. Mo, W. D. Richards, L. Miara, H. S. Lee and G. Ceder, Energy Environ. Sci. 2013, 6, 148.
34. N. Kamaya, K. Homma, Y. Yamakawa, M. Hirayama, R. Kanno, M. Yonemura, T. Kamiyama, Y. kato, S. Hama, K. Kawamoto and A. Mitsui, Nat. Mater. 2011, 10, 682.
35. T. Mueller, G. hautier, A. Jain and G. Ceder, Chem. Mater. 2011, 23, 3854.
36. H. Chen, G. Hautier and G. Ceder, J. Am. Chem. Soc. 2012, 134, 19619.
37. J. Maddox, Nature 1988, 335, 201.
38. R. E. Bellman, in Adaptive Control Processes, Princeton University Press, Princeton, NJ, 1961.
39. A. Laio and F. L. Gervasio, Rep. Prog. Phys. 2008, 71, 126601.
40. K. Rajan, Mater. Today 2005, 8, 38.

Chapter 2. Global minimum energy structure search in Li_xCoO_2

2.1. Background of the study

The O3 layered structure $LiCoO_2$ is the first commercial and one of the most commonly used active cathode material for secondary Li batteries due to its good cycling performance during charge and discharge reactions, which involve the electrochemical removal and insertion of Li ions [1-3]. This fast Li ion conductor which belongs to the R-3m space group and rhombohedral symmetry (see Figure 2-1) has an open circuit voltage (OCV) of ~4 V vs. Li metal [4]. The stacking of O-Co-O slabs are distinguished as ABCABC… ordering. The related intercalation mechanism shows the CoO_2 host framework being almost unchanged during the delithiation process in the compositional range is $1/2 < x < 1$ (x in Li_xCoO_2). However, some small, yet discernible, structural change can be distinguished in the range $0 < x < 1/2$ and can be viewed as a stacking fault perpendicular to c-axis caused by simple gliding of the Co octahedron layer, eventually leading to continuous capacity fading. This emphasizes the important relationship between changes in the host structure and electrochemical cyclability [5-6].

In recent years, large-scale battery development for electric vehicles and stationary energy storage devices has been poured with investment and is becoming increasingly attractive in the today's society; the latter technology is now being used more as backup for conventional power sources. With the impending effect of climate change causing more typhoons and erratic weather conditions each year, potentially inflicting more devastation to existing power grids and infrastructures, the importance of back-up power systems are becoming increasingly important. The same case is true for areas which frequently experience high-magnitude earthquakes. Therefore, it is imperative that standby back up energy devices are reliable and stable even at long periods of time.

Back-up batteries are usually kept in a fully charged state for up to 10 years. During standby mode, the electrochemically delithiated phase of layered Li_xCoO_2 ($x < 1$) is in a metastable state, and with longer time scale, formation of more stable phases are conceivable and can lead to the eventual degradation of the device itself. Therefore, it is necessary to evaluate the cathode material with respect to its long-term storage stability. The thermodynamic ground state and metastable structures should be investigated for different Li ion contents of the host Li_xCoO_2 layered structure. However, experiments for such of studies have been limited because of the difficulty in evaluating the structural change from the metastable to ground-state phase over several years. This

technical challenge needs to be addressed in order to systematically study the structure of Li_xCoO_2. A practical approach for this issue would be to use structural prediction techniques with energy evaluation in DFT framework to determine the thermodynamic ground state of any given composition. In this work, the evolutionary approach [7] is used to effectively sample the Li_xCoO_2 energy landscape to search the global minimum energy structures at different Li content x. This technique has already been used in the prediction and confirmation of novel materials [8-10].

2.2. Structural description

Li, Co, and O Wyckoff positions in $LiCoO_2$ are assigned as 3a octahedral, 3b octahedral, and 6c sites, respectively. The ratio c/a = 4.989 is larger than that of an ideal cubic-close-packed lattice, where c/a = 4.899. As more Li is extracted, insterslab repulsion is increased and the c/a ratio is further increased [11]. At x = 1/2, shearing of the rhombohedral oxygen lattice occurs which sets the onset for monoclinic distortion. This translation also significantly changes the lattice angle β [3] and Li ion ordering in rows is reported to become favorable [12]. Thermodynamically, a spinel phase with Li ions in the 8a tetrahedral sites will eventually form at this composition; this formation is observed after extensive charge/discharge cycling processes [13-14]. At x = 0, further shearing leads into the hexagonal packing of oxygen ions with ABAB sequence of O-Co-O slabs along the c-axis; this is referred to as O1 (P-3m1) structure [15-16].

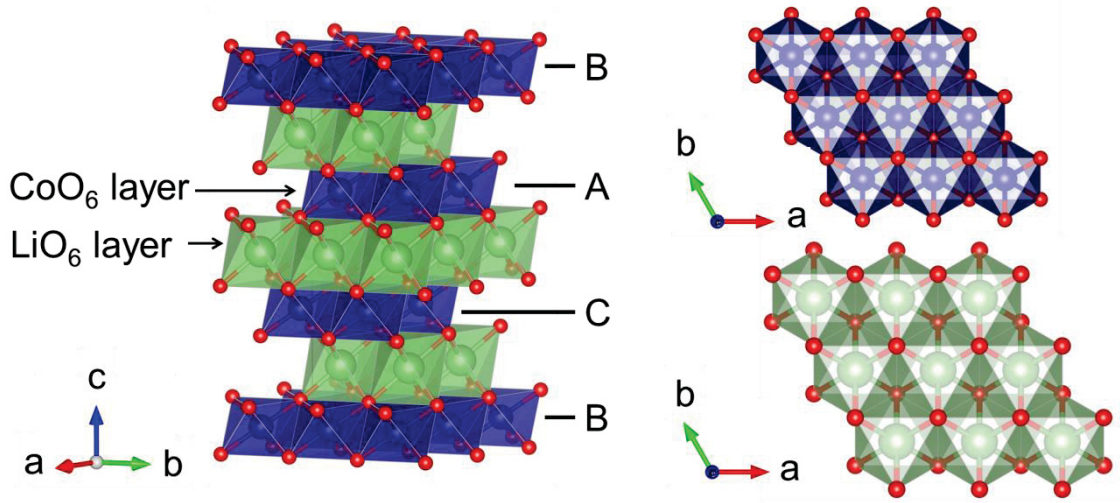

Figure 2-1. A 2 x 2 x 1 supercell of R-3m $LiCoO_2$ with highlighted stacking of the O-Co-O slabs in ABCABC… ordering. Blue and green octahedra layer are CoO_6 and LiO_6 units, respectively. Planar view of the CoO_6 and LiO_6 layers are also shown.

2.3. Structure search by evolutionary algorithm

Evolutionary algorithm treats structural variables as physical numbers and incorporates "learning from history", i.e., the offspring structures will have resemblance to the more successful structures from previous sampling. This is carried out in three stages: i.) the selection of the low-energy structures to become parents of the new generation, ii.) the survival of the fittest structures, and iii.) the tweaking of structures by variation operators. These variation operators are basically the recipe for creating offspring structures from parent structures.

There are three common types of variation operators. The first one is the heredity operator which produces offspring structures from planar slabs cut from two parent structures. The second one is the lattice mutation operator which creates offspring structures through large deformation applied to a parent structure. The third one is the permutation operator which swaps chemical identity in pairs of chemically different atoms. The simplified representation of the three operators is indicated in Figure 2-2.

It is necessary that the population of structures be kept diverse enough to avoid trapping in local minima. To measure diversity, it is important to detect similar structures so they can be removed from the structure pool, thereby ensuring that radically different solutions can be obtained. One way to do this is through a structure fingerprint function, $FP(R)$:

$$FP(R) = \frac{V_{uc}}{N_{uc}B}\sum_{i\epsilon uc}\sum_{j\epsilon euc}\frac{Z_i Z_j}{4\pi R_{ij}^2}\delta\left(R - R_{ij}\right) \tag{2-1}$$

where $i \neq j$, Z are atomic number of atoms i and j, R is the distance between atoms i and j, V_{uc} is the volume of the unit cell, N_{uc} is the number of atoms in the unit cell, and B is the bin width used to discretized $FP(R)$ to obtain the fingerprint vector. $\delta\left(R - R_{ij}\right)$ is a Gaussian-smeared delta function, absorbing numerical errors and making $FP(R)$ a smooth function. Since $FP(R)$ describes the correlations between atomic positions, it can be used as well to characterize the structure's order parameter Π:

$$\Pi = \frac{B}{\lambda}|FP(R)|^2 \tag{2-2}$$

where λ is characteristic length (eg., a cubic root from volume per atom for a given system).

With a means to measure structural similarity, structures can be compared using the abstract cosine distance D_{ij}:

$$D_{ij} = \frac{1}{2}\left(1 - \frac{FP_i \cdot FP_j}{\|FP_i\|\|FP_j\|}\right). \tag{2-3}$$

D_{ij} are distances measure the structural dissimilarity and can only take values between 0 and 1[2]. The metric for diversity can then be evaluated using the function called collective quasientropy, S_{coll}:

$$S_{coll} = -\langle(1 - D_{ij})\ln(1 - D_{ij})\rangle \quad (2\text{-}4)$$

After structure relaxation, the locally optimized structures are compared and ranked in order of their free energies. For the parent selection step, the probability P of selecting a structure is determined by its fitness rank i, e.g. in a linear scheme:

$$P(i) = P_1 - (i - 1)\frac{P_i}{c}\ , \sum_{i=1}^{c} P(i) = 1 \quad (2\text{-}5)$$

where c is a selection cutoff.

The detailed scheme for the implementation of evolutionary algorithm in combination with structure relaxation is displayed in Figure 2-3 [17].

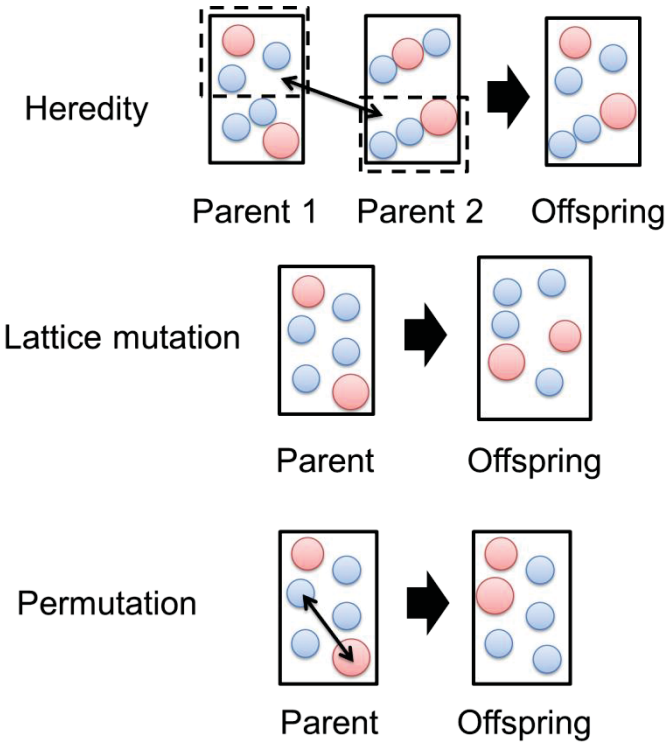

Figure 2-2. Concept view of variation operators in evolutionary algorithm.

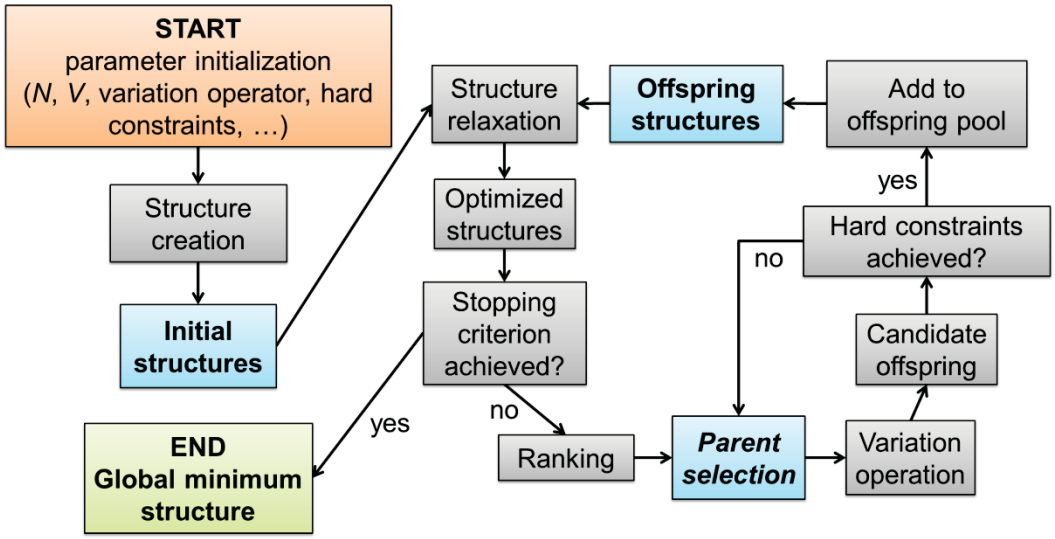

Figure 2-3. Flowchart of evolutionary algorithm in combination with structure relaxation for search of global minimum energy structure.

2.4. Computational details

The evolutionary variable-cell simulations were carried out for the LixCoO2 using the Universal Structure Predictor: Evolutionary Xtallography (USPEX) code [17-21]. Several compositions were explored: x = 0, 1/4, 1/3, 1/2, 2/3, 3/4, and 1. Atomic stoichiometry was observed, for example, Co:O = 1:2, 2:4, 4:8 in CoO2, Li:Co:O = 1:4:8, 2:8:16 in $Li_{1/4}CoO_2$, Li:Co:O = 1:3:6, 2:6:12 in $Li_{1/3}CoO_2$, and Li:Co:O = 1:2:4, 2:4:8, 4:8:16 in $Li_{1/2}CoO_2$. With the initial population randomly generated beforehand, about 20 structures were allowed to compete in each generation. When the lowest energy structure remained the lowest for 25 consecutive generations, or after 50 generations, the simulation was terminated. Since evolutionary algorithm is a heuristic method, the exploration per composition was repeated 6 times.

For the underlying energy calculation, *ab initio* method was used with conditions of 0 K and 0.1 MPa performed within the DFT framework of the generalized gradient approximation (GGA) [22], as implemented in the Vienna Ab Initio Simulation Package (VASP) [23]. Three local optimization levels were set, with accuracy increasing at each level. For the first level (coarse), the setting is as follows: plane-wave cutoff energy set to the maximal minimum of the pseudopotentials, break condition for the ionic relaxation loop set to 2×10^{-1} eV, total energy error threshold at 3×10^{-3} eV. For the second level (intermediate), the setting is 450 eV, 1×10^{-2} eV, and 1×10^{-3} eV, respectively. For the third level (normal), the setting is 450 eV, 1×10^{-3} eV, and 1×10^{-4} eV, respectively. The global minimum energy structure at the end was further relaxed with a setting of 500 eV, 1×10^{-3} eV, and 1×10^{-4} eV, respectively. The k-point resolution was set to at least 800. The valence electrons, according to projector augmented-wave (PAW) potentials, were defined as s1p0 for Li, d8s1 for Co, and s2p4 for O [24-25]. The functional described in the Perdew-Burke-Ernzerhof parameterization for solids (PBEsol) was used to treat the exchange and correlation interactions [26-27]. The KPLOT software was used to evaluate the symmetry of the searched structures [28].

2.5. Results and discussion

2-5-1. Structure population and diversity

A benchmark study was first carried out using two compositions which are already extensively investigated through experiments (x = 1 and x = 1/2). The purpose of this is to establish the validity of the input parameters for the structural prediction as well as for the energy evaluation using *ab initio* DFT. The results are summarized from Figure 2-2a to 2-2d; the figure shows the enthalpies of the generated structures, predicted global minimum energy structures, population diversity (quasientropy, S_{coll}) [29], and calculated XRD plots, respectively. As indicated, the prediction for the two compositions, $LiCoO_2$ and $LiCo_2O_4$, reproduced the experimentally reported thermodynamics phases which are the O3 and spinel configurations, respectively. Using the characteristic fingerprint functions of the different structures generated in the simulated competition, the diversity of structures from all generations was also evaluated as given by the S_{coll} plot [30]. For both compositions, the S_{coll} metrics suggested a relatively retained degree of diversity for the majority of the sampling except for the first few generations where the diversity is higher. This implies that the search has effectively "zoom in" or focused on the energy basin where global minimum energy structures are located.

For the $LiCoO_2$ composition, the simulated competition was carried out successfully after 27 generations with stable S_{coll} values. In the first generation, the lowest energy structure (LES1) that was formed already has the topological O3-like layered configuration except that the symmetry was monoclinic with lattice angle $\beta = 82.180°$. In addition, the correct alternate layering of the Li and Co cations with respect to the c-axis was already obtained even at this very early stage. Even when LES1 was re-optimized with higher precision settings, it did not change into a hexagonal symmetry in which $\beta = 90°$, which is the recognized most stable phase, suggesting a high energy barrier for the said transformation. Thus, LES1 can be considered as a configuration which resides near the energy funnel containing the O3 configuration. Of the lowest energy structures in each generation, the cobalt oxide layer did not change significantly during the structural competition, which made it an important high-order fragment during structural evolution. The calculated range of the Co-O bond length in the lowest energy structures was 1.930-1.940 Å. The subsequent mutation operation was then effectively able to cross the energy barrier for the LES1 → O3 reaction and the

final structure was confirmed to be indeed that of the hexagonal O3 phase (R-3m) with β = 90°. The Co-O and Li-O distances for the global minimum energy structure O3 are 1.910-1.912 Å and 2.070-2.100 Å, respectively, and are in reasonable agreement with previous experimental reports [31].

For the $Li_{1/2}CoO_2$ composition, the calculation search leading to the spinel phase formation as the global minimum structure (Figure 2-2d) proceeded for 38 generations before termination. The S_{coll} values are also confirmed to be stable (Fig. 2-2b). Just like in the case of $LiCoO_2$, the lowest energy structures for $LiCo_2O_4$, for each generation, have face-centered-cubic oxygen packing and this observation was also found even in the first generation (Figure 2-3). The difference between the former and the latter is how the constituent cations are ordered within the voids of the oxygen array. The LES1 for $LiCo_2O_4$ prediction (generation 1) is noted to have the cation positions permutated to form a reverse variant with a more negative enthalpy (generation 4). Partial reorganization of the Co atoms then formed Li-Co mixed layers (generation 7). This configuration then transformed into an O3-like layered variant with uniform Li and Co layers (generation 8). Finally, the spinel phase was successfully evolved (generation 15 and 38). The optimized Co-O and Li-O distances are 1.880-1.890 Å and 1.914-1.916 Å, respectively. Moreover, the validity of the results are further established with the emergence of the O3-like layered phase. This configuration is an important metastable state as it can be formed during an electrochemical Li extraction.

Another observation is the similarity of the calculated XRD patterns (Figure 2-4) for the O3 layered $LiCoO_2$ (R-3m) and the spinel $LiCo_2O_4$ (Fd-3m) structures. This can be attributed to the similarity in the oxygen packing between the two phases and the low scattering factor of Li ions which makes their detection difficult during measurements [32].

Based from the successful prediction of global minimum structures at x = 1 and x = 2, it was verified that: (i) the use of evolutionary approach with multiple starting structures is a justified and an effective approach for finding minimum energy structures, and (ii) the settings for structural relaxation was appropriate to obtain global minimum structures.

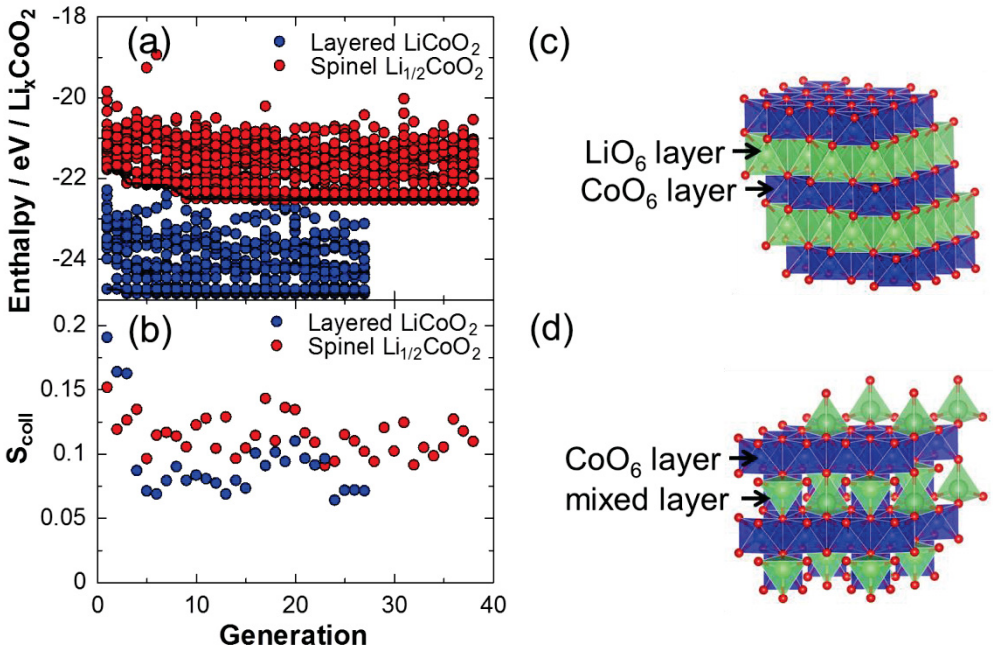

Figure 2-2. (a) Calculated enthalpies of generated structures, and (b) population diversity (quasientropy) as functions of generation. The lowest energy structures are (c) O3 layered phase ($LiCoO_2$, R-3m) and (d) spinel phase ($LiCo_2O_4$, Fd-3m). Blue, green, and red spheres are Co, Li and O atoms, respectively.

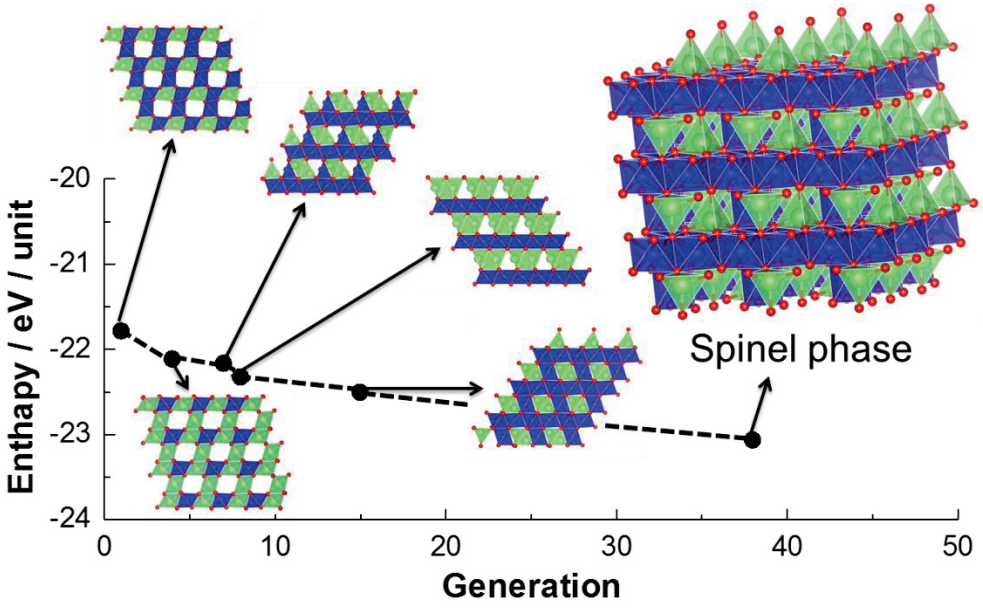

Figure 2-3. Planar view of the structural evolution of the lowest energy structures using $Li_2Co_4O_8$ ($Li_{1/2}CoO_2$ unit) composition leading to the spinel (Fd-3m) phase formation. Structural motifs are displayed for generation 1, generation 4, generation 7, generation 8, generation 15, and generation 38. Blue, green, and red spheres are Co and Li, and oxygen atoms, respectively.

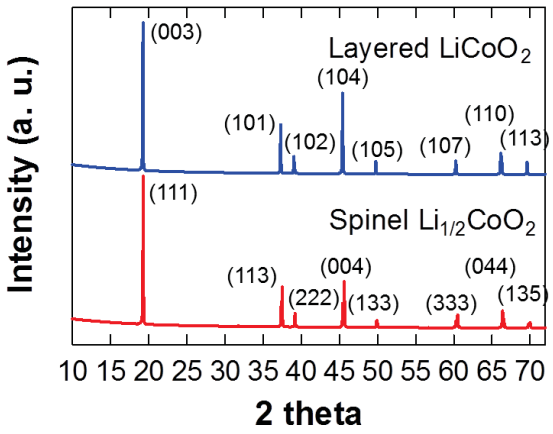

Figure 2-4. XRD patterns of for layered $LiCoO_2$ and $Li_{1/2}CoO_2$ with assigned peaks.

2-5-2. Topology of predicted minimum energy structures

Shown in Fig. 2-5 is the reduced energy landscape derived from the distribution of about 1000 generated structures at each surveyed Li_xCoO_2 compositions and leading to lowest energy layered phases. The energy surface is defined in here by average order parameter (see equation 2-2) and volume per atom basis. Based from these contour plots, the evolutionary approach is noted to be effective in locating a number of local minima as well as finding the major energy basins at different compositions. These basins can be characterized as locus of points representing structures with high symmetry. It is now apparent that structures with relatively high average order (degree of symmetry) have more negative enthalpies, and thus are more stable, than those with lower order or more random arrangement of atoms [33]. Meanwhile, cell volume is determined to be weakly correlated with structural stability and an optimized value exists with respect to composition. At $x = 0$, the prediction resulted into an intermediate O1 structure, with hexagonal closed-packing and a Co-O distance of 1.859-1.862 Å (Fig. 2-5a). The same O1 stacking was also determined with face-sharing of Co and Li octahedra for the global minimum structure at $x = 1/7$ (Fig. 2-5b); Co-O and Li-O distances are 1.850-1.886 Å and 2.030-2.477 Å, respectively. A monoclinic structure (C2/c) was noted at $x = 1/2$ with $\beta = 101.815°$ (Fig. 2-5c) and with Co-O and Li-O distances to be about 1.865-1.888 Å and 2.002-2.672 Å, respectively. This structure is characterized by coherent zigzag Li chains in the intercalation layer and Li vacancy ordering as reported by Reimers et al. [3] and Horn et al [12]. Meanwhile, O3 stacking and no O1 stacking was observed for the rest of the intermediate compositions at $1/2 < x < 1$.

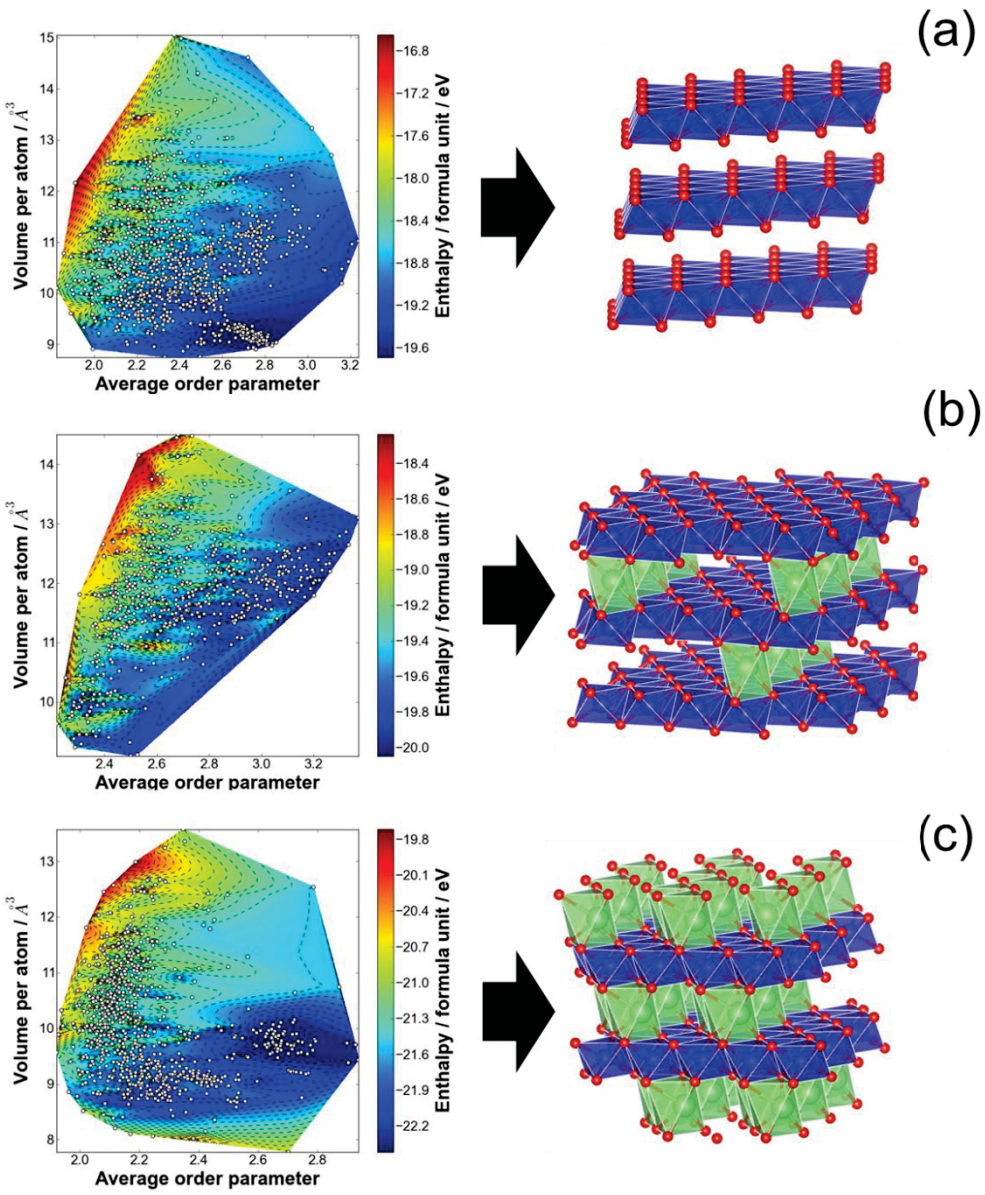

Figure 2-5. Crystal structure prediction by evolutionary algorithm leading to layered Li_xCoO_2 phases. Energy landscape sampling is shown for (a) O1 structure (P-3m1), (b) O1 structure at x = 1/7, and (c) monoclinic structure (C2/c) at x =1/2. Green and blue octahedra are Li and Co atoms, respectively.

New non-layered phases in the composition $x < 1/2$ that showed more negative enthalpies than their layered counterparts are given in Figure 2-6. Again, a strong (weak) correlation is established between average order (cell volume) and stability. These non-layered structures have a similar topology with rutile-like configurations (Pnnm, P42/mnm) with (1 × 1) tunnels at $x = 0$ (Figure 2-6a) and ramsdellite-like configurations (C2/m, P2/m) at $x = 1/4$ and $x = 1/3$ (Figures 2-6b and 2-6c) with (3 × 1)-(1 × 1) and (2 × 1)-(1 × 1) tunnels, respectively. For the rutile-like variant, the Co-O distance was calculated in the range of 1.843-1.845 Å, whereas the ramsdellite-like variant had Co-O and Li-O distances of 1.814-1.922 Å and 1.789-2.194 Å, respectively. As previously mentioned, a possible transformation pathway for these non-layered host structures is through Co migration from the CoO_6 layer into an octahedral environment in the Li layer. The tunnels in the structure can be regarded as part of the original Li plane. On the other hand, the structures at $x = 1/4$ and $x = 1/3$ need coherent stacking faults along the c-axis for them to form from their layered phases. These new configurations are comparable with those found in MnO_2 compounds [34]. The same case is apparently justified for spinel $LiCo_2O_4$, in which Co ions need to migrate into the Li plane to form the lowest energy configuration. At $1/2 < x \leq 1$, only O3 stacking were predicted. Assuming that spinel formation is kinetically limited, the results are complementary to the established range of electrochemical stability for layered $LiCoO_2$.

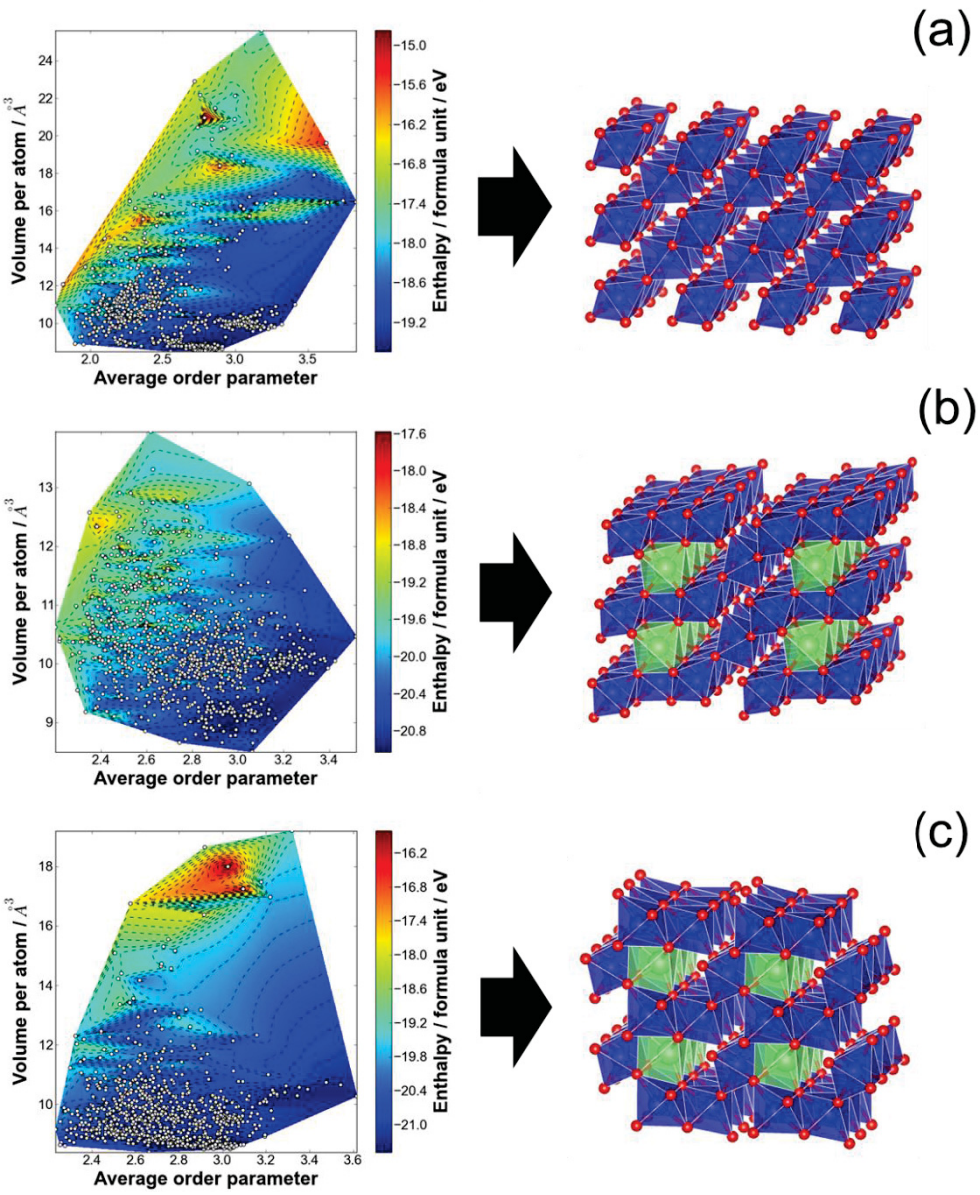

Figure 2-5. Crystal structure prediction by evolutionary algorithm leading to non-layered Li_xCoO_2 phases. Energy landscape sampling is shown for: (a) rutile-like structure (P42/mnm) with (1 × 1) tunnels at x = 0, and (b, c) ramsdellite-like structure with (3 × 1)-(1 × 1) tunnels and (2 × 1)-(1 × 1) tunnels at x = 1/4 and at x = 1/3, respectively. Green and blue octahedra are Li and Co atoms, respectively.

2-5-3. Relative stability of predicted minimum energy structures

Stability of the phases in $LixCoO_2$ can be completely described by the knowledge of the free energies at every investigated Li content x. At low temperatures in which T ~ 0 K and entropy S ~ 0, the ground state energies found from *ab initio* DFT energy evaluation can be used to approximate the phase diagram. Once these energies are derived, the formation energy ΔE of a particular phase can then be calculated as a cohesive energy relative to the composition-weighted average cohesive energies of the end member compositions [16]:

$$\Delta E(x) = E(x) - xE(x = 1) - (x - 1)E(x = 0) \quad (2\text{-}1)$$

where $E(x)$ is the total energy of the configuration per Li_xCoO_2 formula unit, $E(x = 1)$ is the energy of $LiCoO_2$ in the O3 host, and $E(x = 0)$ is the energy of CoO_2 in the O1 host. When plotted versus composition x, the convex hull curve for Li_xCoO_2 can be generated. This plot is displayed in Figure 2-5. The concept of formation energy describes the relative stability of a predicted structure against separation into the $LiCoO_2$ fraction and the (1 – x) CoO_2 fraction. When $\Delta E(x)$ is negative, the formation of a particular compound is said to be favored. This is represented by the location of the point $(x, E(x))$ with respect to the convex hull, in which a point below the hull means favored while a point above means an unfavored formation.

For the kinetically controlled layered phases, their convex hull is indicated by the solid tie line. Meanwhile, another convex hull, shown as a hatched tie line, represents the thermodynamic ground reaction route for the Li_xCoO_2 system. From interpreting the plot, the layered structures are expected to decompose and transform into more stable variants, except at x = 1. In addition, spinel $LiCo_2O_4$ will coexist with layered $LiCoO_2$ at $1/2 < x < 1$. At $0 < x < 1/2$, spinel $LiCo_2O_4$ and a rutile-like structure are predicted to be the end member compositions.

It becomes obvious that the midpoint composition at x = 0.5 forms an important end member structure and is crucial towards understanding $LiCoO_2$ cathode stability. From a closer inspection of the topology, layer to spinel transformation can be imagined as a reaction in which the onset is facilitated by Co ion migration. This can occur during excessive cycling and implies that the other predicted non-layered structures could be formed via a similar route. However, this migration is not yet understood well. Surveying the literature, one useful report that could shed light about this issue is an *ab initio* calculation study

which suggested a spinel or spinel nucleus formation from layered configuration; the mechanism is assisted by a charge-disproportionation reaction [35]:

$$2Co^{3+}_{octahedral} = Co^{2+}_{tetrahedral} + Co^{4+}_{octahedral} \quad (2\text{-}2)$$

where $Co_{octahedral}$ and $Co_{tetrahedral}$ are the octahedrally and tetrahedrally coordinated Co ions, respectively. In this process, $Co_{tetrahedral}$ is surrounded by Li trivacancy nearest neighbors in the Li plane has a high static migration energy barrier of 1.5 eV. In Co^{2+} species has an unfavorable outer electron configuration (d7) for complete covalent bonding when at the triangular (activated state) and the tetrahedral position in the Li plane. As a consequence, the change in ligand field stabilization energy for tetrahedral coordination is expected to be unfavorable as well [36]. This, in turn, leads to the kinetic frustration of the spinel phase formation. In contrast, at x < 1/2, Co ion migration is suggested to be a favorable reaction owing to the destabilization of the layered structure in relation to the Madelung energy minimization [37]. This harmonizes with the results for several non-layered structures that were predicted to be favorable, examples include the rutile-like and the ramsdellite-like variants. Thus, it is highly likely that when the charge state of $LiCoO_2$ cathodes at x < 1/2 are kept for sufficiently long enough time, metastable to non-layered phase formation should occur. The critical parameters that could facilitate this reaction are Co size factor effect and Li vacancy configuration.

A thermodynamics study on the thermal degradation of charged Li battery cathodes was conducted by Wang et al [38]. From the calculated Li-Co-O_2 ternary diagram, it was suggested that for partially delithiated Li_xCoO_2, the favorable thermodynamic end route is spinel phase formation, specifically Co_3O_4 and O_2 gas products. Referring to this results, the stability of the predicted non-layered structures were evaluated by calculating the reaction energies given by [39]:

$$Li_xCoO_2(\text{predicted}) \rightarrow \frac{(1-x)}{3}Co_3O_4 + xLiCoCo_2(\text{layer}) + \frac{(1-x)}{3}O_2 \quad (2\text{-}3)$$

The calculated reaction energies for x = 0 (rutile-like), x = 1/4 (ramsdellite-like), x = 1/3 (ramsdellite-like), and x = 1/2 (spinel) were +0.754, +0.584, +0.548, and +0.597 eV / Li_xCoO_2 unit, respectively. These suggest that all the predicted non-layered phases are thermodynamically stable against the oxygen evolution reaction. Therefore, these phases are reasonably important over the course of long-term storage of the delithiated layered variants of Li_xCoO_2. However, the reaction energy calculation scheme employed based on reaction 2-3 does not take into account any discrepancy associated to inherent errors from GGA formalism

such as over-binding in the O_2 molecule and correlation effects in the 3d orbitals [40, 41, 42]. Therefore, some of the calculated reaction energies could still shift to the exothermic region, i.e., negative reaction energies.

The rutile-like CoO_2 phase has not been reported yet experimentally, and it is possible that some of the predicted non-layered structures are not the actual ground-state phases but metastable phases. However, since the cathode can oftentimes be subjected to severely restricting conditions, formation these structures cannot be completely ruled out. For instance, spinel $LiCo_2O_4$ can be formed under repeated electrochemical cycling of $LiCoO_2$ [13-14] or during chemical delithiation of a low temperature phase of $LiCoO_2$ [43-44]. Similarly, the predicted non-layered phases may also form as a result of long-term storage under charged state.

2.6. Conclusions

The lowest energy minimum structures in the Li_xCoO_2 composition ($0 \leq x \leq 1$) were successfully investigated using the hybrid evolutionary algorithm with *ab initio* DFT energy evaluation. Specifically, the following results are determined in the study:

1) The different transformations of Li_xCoO_2 during the Li deintercalation were correctly predicted.
2) New non-layered host structures at $x < 1/2$ were predicted to be more favorable than their layered counterparts.
3) Formation of non-layered configurations is suggested to be facilitated by Co ion migration from the CoO_6 layer into the octahedral sites of the LiO_6 layer at low Li concentration ($0 \leq x \leq 1/2$).
4) Co ion migration can be aided by the destabilization of the Co octahedron layer as more electrons are drawn out during Li delithiation.
5) The predicted non-layered structures were thermodynamically stable against decomposition or oxygen evolution.

2.7. Future work and direction

The following points are the suggested for the future work of the study:

1) a detailed mechanistic investigation of the Co ion migration for the highly delithiated phases.
2) exploration of the cathode stability across different compositions (Ni, Mn, Fe, and their solid solutions) with layered-type and fully-lithiated base configurations.

2.8. Chapter references

1. T. Ohzuku and A. Ueda, J. Electrochem. Soc., 1994, 141, 2972.
2. K. Mizushima, P. C. Jones, P. J. Wiseman and J. B. Goodenough, Mater. Res. Bull., 1980, 15, 783.
3. J. N. Reimers and J. R. Dahn, J. Electrochem. Soc., 1992, 139, 2091.
4. M. K. Aydinol, A. F. Kohan and G. Ceder, Phys. Rev. B, 1997, 56, 1354.
5. D. Aurbach, B. Markovsky, A. Rodkin, E. Levi, Y. S. Cohen, H. –J. Kim and M. Schmidt, Electrochim. Acta, 2002, 47, 4291.
6. Y. Zhang, C. Y. Chung, L. X. Sun and M. Zhu, Mater. Chem. Phys., 2008, 107, 254.
7. S. M. Woodley, P. D. Battle, J. D. Gale and C. R. A. Catlow, Phys. Chem. Chem. Phys., 1999, 1, 2535.
8. Y. Ma, M. I. Eremets, A. R. Oganov, Y. Xie, I. Trojan, S. Medvedev, A. O. Lyakhov, M. Valle and V. Prakapenka, Nature, 2009, 458, 182.
9. A. R. Oganov, Y. M. Ma, Y. Xu, I. Errea, A. Bergara and A. O. Lyakhov, Proc. Natl. Acad. Sci. U.S.A., 2010, 107, 7646.
10. A. R. Oganov, J. Chen, C. Gatti, Y. –Z. Ma, Y. –M. Ma, C. W. Glass, Z. Liu, T. Yu and O. O. Kurakevych, Nature, 2009, 457, 863.
11. A. Honders, J. M. der Kinderen, A. H. van Heeren, J. H. W. de Wit and G. H. J. Broers, S1olid State Ionics, 1985, 15, 265.
12. Y. S.- Horn, S. Levasseur, F. Weill and C. Delmas, J. Electrochem. Soc., 2003, 150, A366.
13. H. Gabrisch, R. Yazami and B. Fultz, J. Electrochem. Soc., 2004, 151, A891.
14. H. Gabrisch, R. Yazami and B. Fultz, J. Power Sources, 2003, 119-121, 674.
15. G. G. Amatucci, J. M. Tarascon and L. C. Klein, J. Electrochem. Soc., 1996, 143, 1114.
16. A. Van der Ven, M. K. Aydinol, G. Ceder, G. Kreese and J. Hafner, Phys. Rev. B, 1998, 58, 2975.
17. C. W. Glass, A.R. Oganov and N. Hansen, Comput. Phys. Commun., 2006, 175, 713.
18. Q. Zhu, A. R. Oganov, A. O. Lyakhov, CrystEngComm. 2012, 14, 3596.
19. A. R. Oganov, C.W. Glass and S. Ono, S. Earth Planet. Sci. Lett., 2006, 241, 95.
20. A. O. Lyakhov, A. R. Oganov and M. Valle, Comp. Phys. Comm. 2010, 181, 1623.
21. H. Wang, Q. Li, H. Wang, H. Liu, T. Cui and Y. Ma, J. Phys. Chem. C, 2010, 114, 8609.
22. J. P. Perdew and Y. Wang, Phys. Rev. B, 1992, 45, 13244.

23. G. Kresse and J. Furthmüller, Phys. Rev. B, 1996, 54, 11169.
24. P. E. Blochl, Phys. Rev. B, 1994, 50, 17953.
25. G. Kresse and D. Joubert, Phys. Rev. B, 1999, 59, 1758.
26. J. P. Perdew, Adrienn Ruzsinszky, G.I. Csonka, O.A. Vydrov, G.E. Scuseria, L.A. Constantin, X. Zhou and K. Burke, Phys. Rev. Lett., 2008, 100, 136406.
27. G. I. Csonka, J.P. Perdew, A. Ruzsinky, P.H.T. Philipsen, S. Lebègue, J. Paier, O.A. Vydrov and J.G. Ángyán, Phy. Rev. B, 2009, 79, 155107.
28. R. Hundt, J.C. Schön and M. Jansen, J. Appl. Cryst., 2006, 39, 6.
29. A. R. Oganov, A. O. Lyakhov and M.Valle, Acc. Chem. Res., 2011, 44, 227.
30. M. Valle and A. R. Oganov, Acta Crystallogr. Sect. A, 2010, 66, 507.
31. D. Carlier, A. Van der Ven, C. Delmas and G. Ceder, Chem. Mater., 2003, 15, 2651.
32. E. Rossen, J. N. Reimers and J. R. Dahn, Solid State Ionics, 1993, 62, 53.
33. A. O. Lyakhov, A. R. Oganov, H. T. Stokes and Q. Zhu, Comput. Phys. Commun. 2013, 184, 1172.
34. J. –B. Li, K. Koumoto and H. Yanagida, J. Mater. Sci., 1988, 23, 2595.
35. J. Reed, G. Ceder and A. Van der Ven, J. Electrochem. Solid-State Lett., 2001, 4, A78.
36. J. B. Goodenough and A. L. Loeb, Phys. Rev., 1955, 98, 391.
37. R. Brec, E. Prouzet and G. Ouvrard, J. Power Sources, 1993, 43-44, 277.
38. L. Wang, T. Maxisch and G. Ceder, Chem. Mater., 2007, 19, 543.
39. J. R. Dahn and E. W. Fuller, Solid State Ionics, 1994, 69, 265.
40. L. Wang, T. Maxisch and G. Ceder, Phys. Rev. B, 2006, 73, 195107.
41. A. Jain, G. Hautier, S. P. Ong, C. J. Moore, C. C. Fischer, K. A. Persson and G. Ceder, Phys. Rev. B, 2011, 84, 045115.
42. K. Miwa and A. Fukumoto, Phys. Rev. B, 2002, 65, 155114.
43. R. J. Gummow, D. C. Liles and M. M. Tackeray, Mat. Res. Bull., 1993, 28, 235.
44. R. J. Gummow, D. C. Liles and M. M. Thackery, Mat. Res. Bull., 1993, 28, 1177.

Chapter 3. Multivariate method-assisted *ab initio*-based new material search of olivine-type $LiMXO_4$ solid electrolytes

3-1. Background of the study

The development of solid electrolytes for all-solid-state rechargeable Li ion batteries has now become a major area of interest. This is primarily driven by the materials' advantages as compared to conventional electrolytes: nonflammability, operating stability because of an oxide-based composition, corrosion resistance (which leads to high safety), a wide range of operating temperatures, and longer service life. However, there are an extremely limited number of identified materials that are considered to be of potential because of problems with the diffusion of Li ions within the framework structure. Some of the oxides that were reported as potential solid electrolytes are garnet-type $Li_5La_3Ta_2O_{12}$, perovskite-type $(Li,La)TiO_3$, Liβ-Al_2O_3, LISICON, and NASICON [1−5]. Finding suitable new solid electrolyte materials will provide the next major advance in this field. In finding good solid electrolytes, the main issue is the low polarizability of Li^+ and O^{2-} which leads to the strong interaction between neighboring ions in a densely packed crystal structure [6].

In search of new solid electrolyte materials, a logical approach would be to survey existing structure types that are form naturally because they ensure some degree of stability in terms of configuration. In connection with this, one of the most commonly forming oxides that can be considered is the olivine group. The olivine structure, indicated in Figure 3-1, has the typical orthorhombic symmetry, belongs to the Pnma space group, and has a slight distortion in the close-packed arrays of oxygen ions. Oxides with olivine structure have been experimentally confirmed, one example is the $LiFePO_4$ composition, and was reported to be capable of high lithium bulk mobility and ultrafast charging/discharging capabilities. These indicate the possibility of olivine-type materials to be used as fast Li ionic conductors [7]. However, electronic conductivity has prevented olivine-type materials with transition metals from being considered as practical solid electrolytes [8−10]. An olivine-type electrolyte material, when successfully developed with high lithium bulk mobility and suppressed electronic conductivity, would be a major technological advance, especially if it is paired with attractive cathode materials of the same structure such as $LiFePO_4$ since reduction of interfacial resistance can be engineered.

An exploration of the $LiMXO_4$ olivine search space, to determine the best

compositions for use as a fast Li ionic conductor, would be an interesting study that can potentially lead to new battery materials discovery. The composition would be, based on main group M octahedral atoms (Group 2, Group 3, lanthanides, and Group 13) and X tetrahedral atoms (Group 14 and Group 15). There is a total of 72 M−X pairs that can be considered and most of the compositions are not yet reported.

In this study, the technical difficulty arising from computational expense for a large number of isostructural compounds is addressed by using informatics driven exploration of the olivine search space. This is carried out by combining *ab initio* methods and a multivariate analysis technique called partial least squares (PLS) regression. The latter technique has been widely adopted in other areas of research but has not been applied yet in the battery field [11−13].

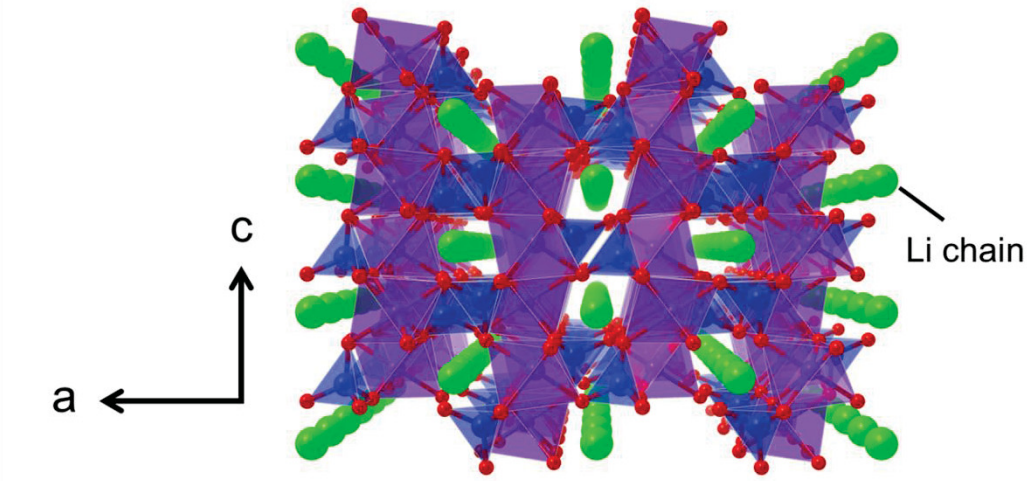

Figure 3-1. Schematic view of the olivine structure. Green spheres are the Li atoms arranged along the b-channel, violet octahedra are MO_6 units, and blue tetrahedra are XO_4 units.

3-2. Multivariate method: partial least squares (PLS) regression

Partial least squares (PLS) analysis is a method for constructing prediction models when the descriptors for a response or set of responses are many and highly collinear. Its prerequisite notions is that the I observations described by K dependent variables are stored in a $I \times K$ matrix denoted Y, the values of J predictors on the I observations are collected in the $I \times J$ matrix X. The goal is to predict Y from X and to describe their common structure. PLS searches for a set of components (called latent variables) that performs a simultaneous decomposition of X and Y with the constraint that these components explain as much as possible of the covariance between X and Y. A regression step is then performed where Y is predicted by using the decomposition in X. An algorithm for this is called the nonlinear iterative partial least squares (NIPALS) algorithm which focuses on maximizing the variance of the dependent variables explained by the independent variables. A PLS model will have a structural part, which explains the relationships between latent variables, a measurement component which reflects how the descriptors and the latent variables are related, and weight relations components which are used for case values estimation for the latent variables.

The NIPALS algorithm starts from two given data blocks, the $I \times J$ matrix X for independent variables and the $I \times K$ matrix Y for dependent variables. The matrix operation then follows according the following procedure:

1. Select a J-weight vector w, e.g., a non-zero row of X, and normalize it to length 1.
2. Enter the loop:
    a. Compute a score vector,
    $$t = Xw. \tag{3-1}$$
    b. Compute a Y-loading vector,
    $$q = Y^{\mathrm{T}}t. \tag{3-2}$$
    c. Compute a Y-loading vector,
    $$u = Yq. \tag{3-3}$$
    d. Compute a new weight vector,
    $$w_1 = X^{\mathrm{T}}u. \tag{3-4}$$
    Scale w_1 to length 1.
    e. If $|w - w_1| < \epsilon$, where ϵ is a predefined error threshold, convergence is achieved, otherwise set $w = w_1$ and go back to step a.
3. Use the latest t and u to construct a latent variable.
4. Construct the succeeding latent variable:

a. Compute the loading vector,

$$p = X^{\mathrm{T}}t/t^{\mathrm{T}}t. \tag{3-5}$$

b. Adjust X,

$$X_{\mathrm{new}} = X - tp^{\mathrm{T}}. \tag{3-6}$$

c. Compute the regression of Y onto t,

$$b = Y^{\mathrm{T}}t/t^{\mathrm{T}}t. \tag{3-7}$$

d. Adjust Y,

$$Y_{\mathrm{new}} = Y - tb^{\mathrm{T}}. \tag{3-8}$$

e. Set $X = X_{\mathrm{new}}$ and $Y = Y_{\mathrm{new}}$.

f. If the variance of the dependent variables explained by the independent variables is maximized, i.e., the root mean square error (RMSE) does not improved upon addition of new latent variables (overfitting), terminate the iteration, otherwise continue with the latent variable construction (go to step 1).

Figure 3-2 shows the conceptual view of PLS method [14, 15].

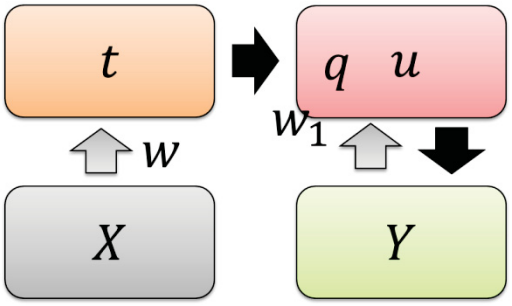

Figure 3-2. Schematic outline of PLS method showing the relationships between relevant matrices as derived from the data blocks X (independent variables or descriptors) and Y (dependent variables or response).

3-3. Computational details

The atomistic model was initialized based on the projected augmented wave (PAW) method [16] through the Vienna *Ab Initio* Simulation Package (VASP) [17]. Olivine compositions with published structural data were taken from the Inorganic Crystal Structure Database (ICSD). The atomic coordinate set of the known materials was used in the structural optimization of virtual compositions [18]. Figure 3-3 shows the different M-X pairs considered in the study.

For the structural optimization step, an energy cutoff of 500 eV is chosen to ensure that the total energies are converged within 3 meV per formula unit. A 2 × 3 × 3 Monkhorst-Pack kpoint grid in a unit cell led to a reasonable convergence and an error of <1 meV/$LiMXO_4$ unit in the total energy. Moreover, the calculated error for the optimized lattice parameters was about ~1.5% on the average and is well within the standard generalized gradient approximation (GGA) error when using the parametrization of Perdew−Burke−Ernzernhof for solids (PBEsol) for the exchange correlation energy [19].

For the Li ion migration pathway and Li diffusion barrier energy (EA), the nudged-elastic-band (NEB) method [20] was used and results were compared with available experimental data [21]. For the NEB method, a 1 × 2 × 2 supercell with a formula unit of $Li_{15}M_{16}X_{16}O_{64}$ (1 Li vacancy created along the diffusion channel), and numerical integration was performed over the Brillouin zone by sampling the Γ point. The error level related to convergence condition was determined to be within 30 meV/formula unit.

All the multivariate analyses were carried out using the JMP statistical software.

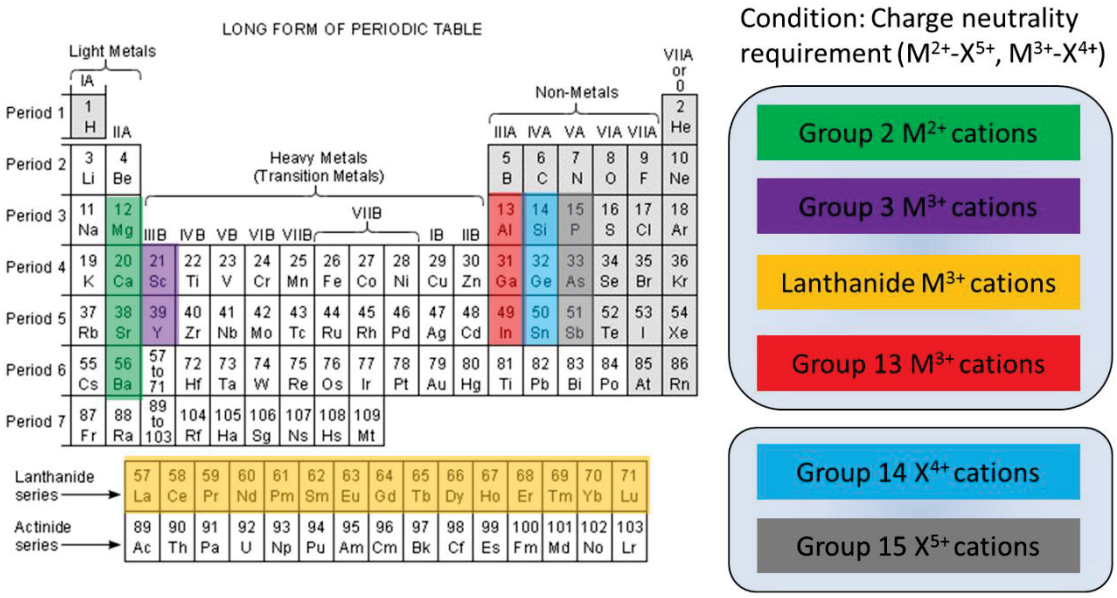

Figure 3-3. Sampling of the olivine-type $LiMXO_4$ search space.

3-4. Results and discussion

3-4-1. Structural variation across the olivine-type $LiMXO_4$ search space

In the $LiMXO_4$ olivine structure, the distortion in the M octahedron can be explained by two main factors: (i) M ions being off-center, which is expressed relative to the tilt of the octahedron from the a-axis (see Figure 1b) and (ii) the variation of θ, the largest internal O−M−O angle, relative to the b-axis (see Figure 1c).

The DFT framework was used to calculate the different crystal structure lattice parameters for all the compositions (Figure 3-5). When different cation pairs constitute the skeleton host structure, observing how the structural parameters change may clarify the determining factors in the value of the Li-ion hopping energy. Figure 3-5a shows the direct relationship between the unit-cell volume and the ionic size (Shannon radii) of the inserted cations in both the M and X sites [22]. For simplicity, the different $LiMXO_4$ samples are denoted by their M−X pairing. The largest volume was determined for $LiBaSbO_4$ (434.87 $Å^3$), and the smallest volume was found for $LiAlSiO_4$ (255.13 $Å^3$). $LiBaSbO_4$ consists of large ions, whereas the $LiAlSiO_4$ consists of relatively small-sized ions. The main cluster of data points belongs to pairs containing rare-earth cations, with a volume that gradually increases with the ionic size of M. Further investigation into the variation along the major axes (Figures 3-5b to 3-5d) revealed that lattice parameter a changes with volume, implying that the volume could be governed primarily by the expansion or contraction in the a axis, as suggested by the distortion shown in Figure 3-4a. The alternating Li and M octahedron along the a-axis are expected to have strong repulsion because they are both highly ionic, especially for large M. This repulsion also will result in M becoming more off-center and farther from the Li channel, directly affecting the value of a. The lattice parameter b is directly influenced by the largest internal angle, θ (Figure 1c). Because the variation in θ causes a strain component along the b-axis, increasing or decreasing it should also alter the value of lattice parameter b. Furthermore, no significant variation in lattice parameter b was observed for different cation sizes of X. The contribution along the b-axis from the X tetrahedra may have been minimal; these sites are generally regarded as interstices for small, strong directionality cations, which cause minimal strain along the major directions. Furthermore, there is no abrupt change in lattice parameter c for different M ioni cradii, where the bulk of the distortion was already taken in along the a- and b-axes. Another important observation here is that large-sized M ions

often lead to more distortion of the related octahedron from the coordinated oxygen ions. As evidence, we calculated the shape unideality factor for polyhedrons, formally defined by the quadratic elongation ⟨λ⟩ of the form [23]:

$$\langle\lambda\rangle = \frac{1}{n}\sum_{1}^{n}\left(\frac{l_i}{l_0}\right)^2 \tag{3-9}$$

where l_i and l_0 are the center-to-vertex distance of the actual and regular polyhedron of the same volume, respectively. ⟨λ⟩ is dimensionless, giving a quantitative measure of distortion that is independent of the effective polyhedron size. For the M octahedron with Group 2 cations such as Mg-P, Ca-P, Sr-P, and Ba-P pairs, the ⟨λ⟩ values are 1.0318, 1.0538, 1.1157, and 1.1574, respectively. Conversely, X cations of Group 13, such as Ca-P, Ca-As, Ca-Sb, Ba-P, Ba-As, and Ba-Sb pairs, follow a similar pattern but to a lesser extent: 1.0032, 1.0080, 1.0203, 1.0008, 1.0017 and 1.0127, respectively. Later, we will discuss these numerical values, among others, and use them to extract the underlying factor(s) to build a prediction model for the Li ion hopping energy, which is characteristic of a particular composition.

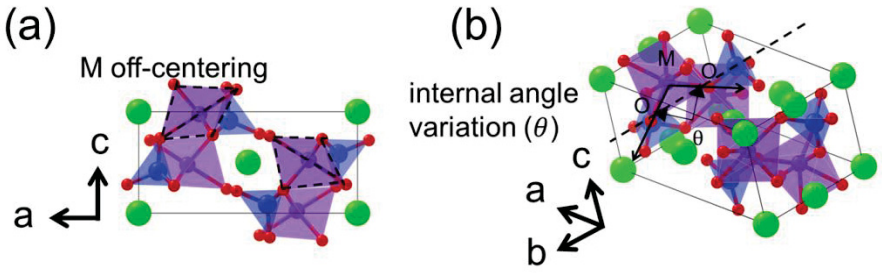

Figure 3-4. (a) 2D view of olivine structure highlighting the off-centering of M cation due to repulsion from the Li channel, and (c) projection view highlighting the variation of the largest internal O−M−O angle, θ, relative to the b-axis. Green spheres represent Li atoms, purple octahedra represent M atoms, and blue tetrahedra represent X atoms.

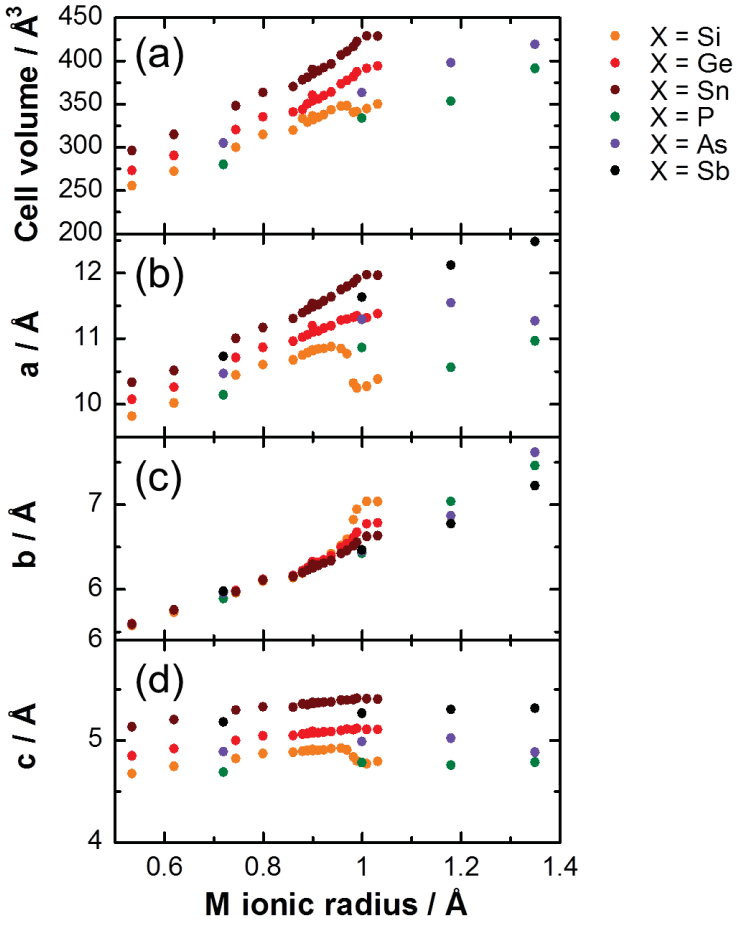

Figure 3-5. Structural data across the olivine $LiMXO_4$ search space: (a) cell volume, (b) lattice parameter a, (c) lattice parameter b, and (d) lattice parameter c of the DFT-relaxed structures, sorted according to X tetrahedral cation.

3-4-2. Li ion migration pathway and its correlation with structural information

The Li ion diffusion barrier EA was computed for several M-X pairs by the NEB method. Different intermediate positions were calculated along the projected distance between two stable Li sites. The threshold value for fast Li ionic conduction was based on the Li ion diffusion barrier energy reported for the $(Li,La)TiO_3$ perovskite material, which is ~0.30 eV, since it has one of the highest experimental Li-ion conductivity value of the oxides (~1×10^{-3} S/cm at 300 K) [3]. A vacancy-driven mechanism along a 1D-diffusion channel was determined for olivine-type cathodes and this diffusion process is adopted in the present study for olivine-type solid electrolytes. Several related studies has been carried out for $LiFePO_4$, an olivine-type material, by using DFT method [24], force-field method [9], and neutron diffraction [25]. Although this 1D conduction is likely to limit conductivity in polycrystalline pellets, this issue can be addressed by controlling the alignment of the grains to minimize inter-grain resistance. Another possible limiting factor is the existence of antisite defects that can give rise to pathway blocking, which eventually could further decrease conductivity [26, 27].

The transport properties of the olivine structure are thought to be largely determined by topology where Li inter-chain routes (see Figure 3-1), which utilize interstitial sites for Li-ion migration, become much more difficult, compared to intrachain motion, because of the very close proximity of Li ions along the chains, as opposed to between chains. A complex energy landscape also exists between chains caused by the two types of polyhedron neighbors (in our study, ionic M octahedra and covalent X tetrahedra). Shown in Figure 3-6 is the pathway of a migrating Li ion in the Li intra-chain as calculated by DFT. The starting and end point (vacancy) are indicated as positions 1 and 2, respectively. Two possible intermediate routes via interstitials along the diffusion channel exist. The first one is through the interstitial site (dashed yellow outline) face-shared with the first-nearest tetrahedral cation X_1 while the second one is through the interstitial site (solid yellow outline) edge-shared with the second-nearest octahedral M cation M_2. The path curvature can then be described as minimizing the long-range interaction between the mobile Li ion and X cation by maximizing their interatomic distance through passage into the immediate interstitial site near the M cation.

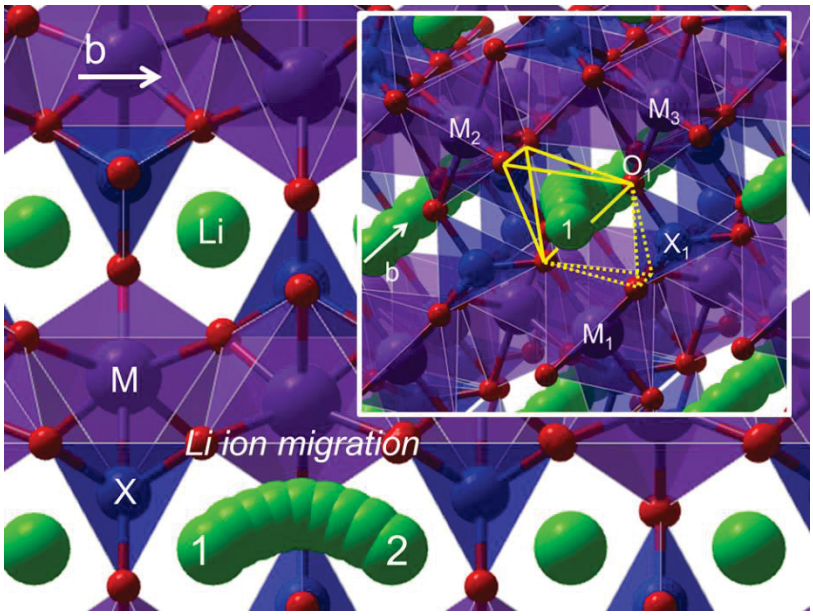

Figure 3-6. DFT-derived Li ion migration (from position 1 to position 2) passing through an interstitial route in olivine-type $LiInGeO_4$. Inset shows the projected view of the path with two possible routes: via tetrahedral site near X1 tetrahedron (dashed yellow outline) and via tetrahedral site near M2 octahedron (solid yellow outline).

To further understand the reason for the preference of Li between two conceivable paths (see Figure 3-5 inset), structural data related to the local environment of the path for several ICSD reported compositions are collected and plotted in Figure 3-7. The energy profiles for a migrating Li ion are displayed as well (panel a of Figure 3-7). As can be noticed, the Li−X_1 distance (panel d in Figure 3-7), when Li is still at position 1, is ~1 Å shorter than Li−M_2. Another point is that the X_1-related route has a face-shared interstitial site with the X_1 tetrahedron while the M_2-related route has an edge-shared interstitial site with the M_2 octahedron. With these factors, the X_1-related route is expected to be energetically unfavorable owing to the expected increased Li−X Coulombic interaction from the decreasing Li−X_1 distance and energy penalty of face sharing in that route. On the other hand, the interatomic distances for Li−O_1 and Li−M_2 decrease up to path midway (see panels b and c in Figure 3-7). For Li−O_1, the variation in the distance profile is relatively small which indicates that the Li octahedral cages are relatively unchanged at different M and X ions. For Li−M_2, the variation is much more obvious, which could be directly attributed to the varying size and distortion of the M octahedron itself. The M_3−X_1 distance only showed a slight increase along the pathway (panel e in Figure 3-7). With the edge sharing of the intermediate tetrahedral pass with the M_2 octahedron, the interaction of the mobile Li with the framework cation should be lesser than in the X_2-related path.

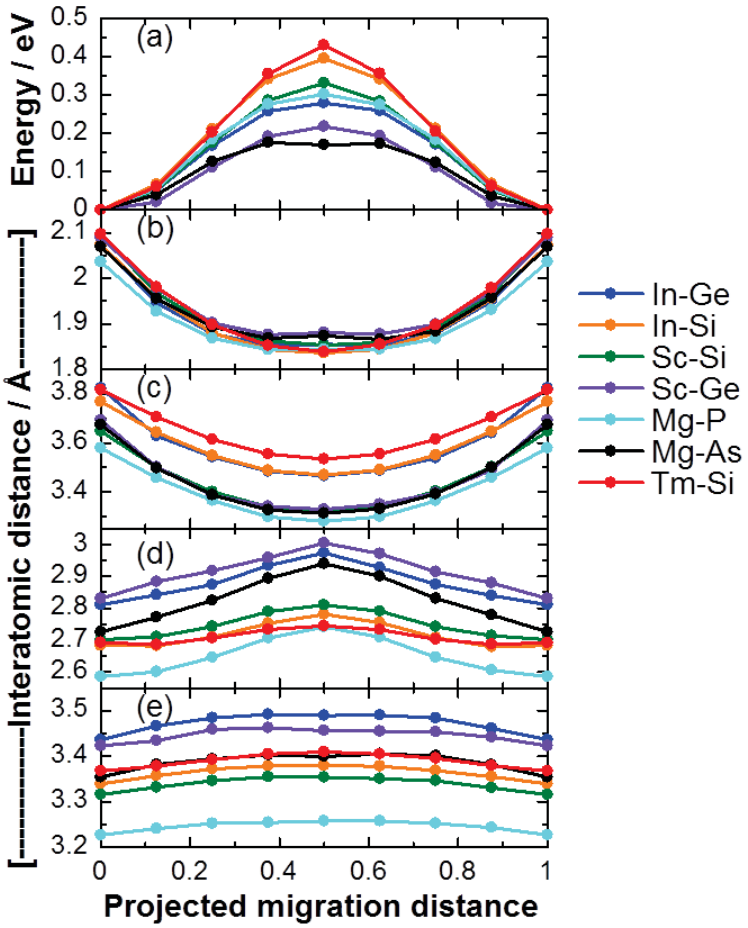

Figure 3-7. Energy and interatomic distance profiles of ICSD-derived $LiMXO_4$ compositions (from NEB method) with (a) EA profiles and the corresponding nearest neighbor interatomic distances during Li ion migration ((b) $Li{-}O_1$, (c) $Li{-}M_2$, (d) $Li{-}X_1$, and (e) $M_3{-}X_1$ distance profiles).

Establishing a sensible relationship between structure-related information and EA must be clarified at this point in order to justify the creation of a reasonable prediction model for the latter. One way to do this is by first investigating the correlation that exists between chemistry and structural variation. The Born effective charge calculation results are compiled in Table 3-1 for M-X combination taken from two elemental groups. It is confirmed here that the dynamic charge of the X cations is considerably smaller than their nominal charge, which confirms the strong covalent character of X−O bonds. For the M cation, the case is opposite where the actual charge tends to be larger than the nominal value. It would be related to the polarizability of M and the partially covalent interaction between M and O which is responsible for the anomalous effective charges and for the anisotropy observed in the oxygen charge tensor [28, 29]. For the Li cation, the dynamic charge is almost isotropic, which is reflective of its low polarizability and similarity with other oxides containing alkali metals [30]. It now becomes apparent that larger M tends to have higher polarizability and this could explain the observed M distortion and M off-centering (see Figure 3-4a). Also, M octahedron tends to have more distortion than the X tetrahedron. Since the pathway maximizes the Li−X_1 distance by passing through an M_2 edge shared interstitial site, the M octahedron distortion, as a function of M cation size, may have a direct influence on the Li migration path.

Table 3-1. DFT-calculated Born effective (dynamic) charges of selected $LiMXO_4$ compositions.

Composition	Effective charge		
	Li	M	X
$LiAlSiO_4$	+1.09	+3.06	+3.04
$LiAlGeO_4$	+1.10	+3.09	+3.21
$LiAlSnO_4$	+1.12	+3.01	+3.66
$LiGaSiO_4$	+1.11	+3.34	+3.05
$LiGaGeO_4$	+1.12	+3.38	+3.20
$LiGaSnO_4$	+1.14	+3.33	+3.59
$LiInSiO_4$	+1.12	+3.41	+2.94
$LiInGeO_4$	+1.14	+3.44	+3.10
$LiInSnO_4$	+1.15	+3.40	+3.33

It is also worthwhile to check other factors that might directly affect the

value of EA. One of these other factors is the steric hindrance of the interstitial oxygen cage edge-shared with M_2 octahedron. However, this factor cannot account for the variation in EA, since the change in Li−O distance with different M during Li migration is negligible (panel b in Figure 3-7). Another factor is the electrostatic repulsive interaction between Li and M_2 (panel c in Figure 3-7) over the course of migration. This repulsive interaction increases as the interatomic distance of Li−M_2 decreases at the transition state. In other words, EA increases with the reduction of the Li−M_2 distance. However, the order of EA (panel a in Figure 3-7) seems to be independent of the Li−M_2 distance (panel c in Figure 3-7). Therefore, the electrostatic repulsive interaction cannot be considered as the critical factor that affects EA. Another factor that can be taken into account is the local lattice distortion effect. To validate this claim, the local lattice distortion that accompanies the actual Li migration process must be quantified. This quasi-volume associated with the path for the migrating Li ion can be estimated from the sum of the polyhedral cages when a moving Li ion is at an initial stable site, when the Li ion is at the interstitial site near with M_2, and when it is at the final position (see Figure 3-6). The path volumes at the initial state (V_i) and the transition state (V_t), respectively, are calculated as follows:

$$V_i = \mathrm{Poly1}_i + \mathrm{Poly2}_i + \mathrm{Poly3}_i \quad (3\text{-}10)$$

$$V_t = \mathrm{Poly1}_t + \mathrm{Poly2}_t + \mathrm{Poly3}_t \quad (3\text{-}11)$$

where Vi and Vt are the quasi-volume of the path at the initial state and the transition state, respectively. The path volume is taken as the sum of Poly1, Poly2, and Poly3, which are the Li ion octahedron volume, interstitial tetrahedron volume, and neighboring octahedron Li vacancy volume, respectively, during the initial and transition state. The findings are given in Figure 3-8 (with the three polyhedrons shown in the inset) using Al-Ge, Ga-Ge, and In-Ge pairs. The volume difference $\Delta V = V_t - V_i$ of the two states is shown to be positive and increasing with increasing M size, suggesting that Li-ion migration is accompanied by significant local lattice distortion. It also indicates that at larger M size, the degree of lattice distortion is increased. Such types of distortion usually involve an energy penalty and complements well with the observed EA variation.

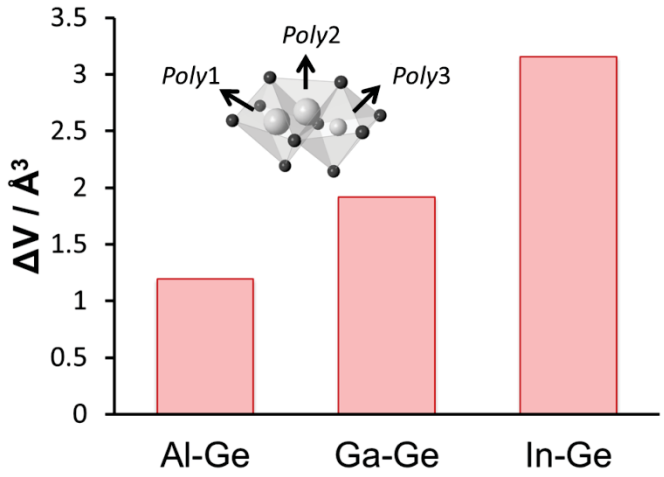

Figure 3-8. Variation in the local lattice distortion along the Li-ion migration pathway expressed in terms of volume difference of the quasi-volume of the path between the transition state (mobile Li ion at interstitial site) and the initial state (before migration). Inset describes the path volume as the sum of the polyhedrons Poly1, Poly2, and Poly3. Large gray spheres in Poly1 and Poly2 depict Li ions while the small gray sphere in Poly3 depicts a Li vacancy. Poly1 is occupied with Li ion at the initial state and empty at the transition state. Poly2 is empty at the initial state and is occupied at the transition state. Sample pairs are Al−Ge, Ga−Ge, and In−Ge.

Among the ICSD compositions, the following are determined to be potential for solid electrolyte use: $LiMgAsO_4$ (0.17 eV), $LiScGeO_4$ (0.22 eV), $LiInGeO_4$ (0.28 eV), and $LiMgPO_4$ (0.30 eV). In here, $LiMgAsO_4$ and $LiScGeO_4$ have not been investigated yet as battery materials. The composition $LiInGeO_4$ has been evaluated theoretically by Rajkumar et al., with similar results [31]. The composition $LiMgPO_4$ was electrochemically characterized by Fehr et al., with EA determined to be about 1.45 eV which is consistent with Li diffusion barrier with additional contribution for Li vacancy formation [32]. The present DFT EA values does not include this contribution.

Towards a successful solid electrolyte candidate material, aside from EA, other factors must be evaluated as well. These are electrical conductivity, stability for forming the olivine framework, and vacancy content, which mediates Li ion hopping in the diffusion channel. Since the substituted M cations here are non-transition metals, electrical conduction should be minimal in all the investigated $LiMXO_4$ compositions and the bulk of the conduction should originate mainly from the ionic component. In terms of stability, some of the compositions being sampled have experimental information in ICSD, some of which are calculated to have low EA values. These are $LiInGeO_4$, $LiScGeO_4$, $LiMgPO_4$, and $LiMgAsO_4$. Some of the non-reported olivine-type materials may be synthesized via hydrothermal methods or high-pressure conditions, and so on. For the vacancy creation in the Li channels, the introduction of aliovalent dopant cations either in the M or X site is suggested. Instances where large fractions of blockage in 1D diffusion in the olivine structure are observed, i.e., antisite defects could be dominated by mobility of other species which allow crossover between different 1D channels. Even with this alternative route, this blocking is likely to reduce the overall Li mobility as well [33].

3-4-3. Prediction model building for EA

DFT-based methods have been known to accurately determine structural parameters [34-36]. Leveraging on this, the entire olivine-type $LiMXO_4$ search space (see Figure 3-2) is then calculated in order to extract structural information that can be used as input variables for EA model building. For use in supervision during model training, some of the stabilized compounds (15 M−X pairs) were then evaluated in terms of EA along the energetically favored b-axis by the NEB method [21]. The input variables extracted from DFT-relaxed unit cells can be categorized under the following: lattice parameters, Born effective charges, intra-polyhedron parameters, and inter-polyhedron parameters.

The underlying assumption for the EA prediction model in this study is that the energy when a Li ion is in an activated state during migration depends on the surrounding configuration and can be described by the information of the stabilized lattice model with no diffusion computed by first principles. With this parameterization, rapid calculation of EA is achievable for any arbitrary composition. For simplicity, the different input variables in here will be hereafter called original variables (OVs). By linearly combining these variables, EA can be formalized as [37]:

$$EA = \sum_{i=1}^{n} \beta_i X_i + \beta_0 \quad (3\text{-}12)$$

where EA represents the Li-ion hopping energy, X_i represents the OVs, β_i represents the model coefficients describing the degree of contribution of each variable to the value of EA, and β_0 is the intercept of the function, which can be determined directly from the model fit. Details regarding the OVs are listed in Table 3-2. Visual representation for the inter-polyhedron-based variables within the olivine structure is displayed in Figure 3-9.

Table 3-2. Description and code assignment for the different original variables taken from relaxed $LiMXO_4$ unit cells.

Symbol	Description
a	lattice parameter a
b	lattice parameter b
c	lattice parameter c
v	unit cell volume
b1	born effective charge of Li cation
b2	born effective charge of octahedral M cation
b3	born effective charge of tetrahedral X cation
l1	average bond length of Li octahedron
p1	polyhedral volume of Li octahedron
i1	distortion index of Li octahedron
e1	quadratic elongation of Li octahedron
v1	bond angle variance of Li octahedron
c1	effective coordination number of Li ion
l2	average bond length of M octahedron
p2	polyhedral volume of M octahedron
i2	distortion index of M octahedron
e2	quadratic elongation of M octahedron
v2	bond angle variance of M octahedron
c2	effective coordination number of M cation
l3	average bond length of X tetrahedron
p3	polyhedral volume of X tetrahedron
i3	distortion index of X tetrahedron
e3	quadratic elongation of X tetrahedron
v3	bond angle variance of X tetrahedron
c3	effective coordination number of X cation
d1	Li octahedron-M octahedron distance at edge sharing
d2	Li octahedron-X octahedron distance at edge sharing
d3	M octahedron-X tetrahedron distance at edge sharing
a1	Li-O-M angle at edge sharing
a2	Li-O-X angle at edge sharing
a3	M-Li-X angle at edge sharing
d4	M octahedron-X tetrahedron distance at corner sharing

d5	Li octahedron-M octahedron distance at corner sharing
d6	Li octahedron-X tetrahedron distance at corner sharing
a4	M-O-X angle at corner sharing
a5	Li-O-M angle at corner sharing
a6	Li-O-X angle at corner sharing
d7	M-M octahedron pair distance at corner sharing
d8	M-M octahedron pair distance near midplane
d9	M-M octahedron pair distance along diagonal axis
a7	O-O-O angle at corner-shared M octahedron pair
d0	X-X tetrahedron pair distance near midplane

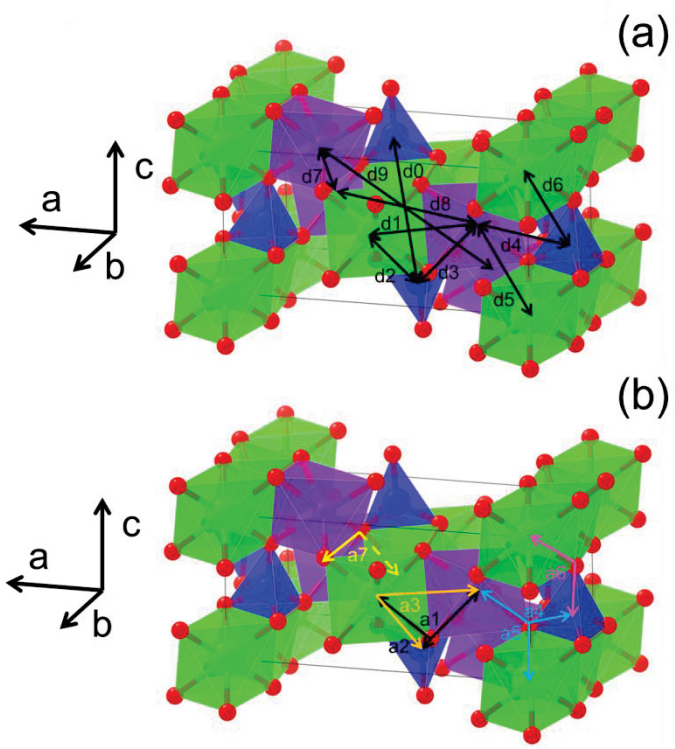

Figure 3-9. Inter-polyhedron parameters within the $LiMXO_4$ unit cell that were used in EA model building.

In PLS modeling, the OVs are projected onto a new space to form latent variables (LVs) in that space. This procedure captures the multidimensional direction in this X space that can explain the maximum multidimensional variance direction in the EA space. The final model showed that 84.13% of the variation in the response variable Y (in this case, EA) can be explained by LV1 and 96.26% can be explained by three LVs (root-mean-square error, RMSE = 0.316). The fit of the model shown in Figure 3-10 shows good accordance between PLS and DFT. In other words, the use of linear function formalism is justified to reproduce the DFT EA.

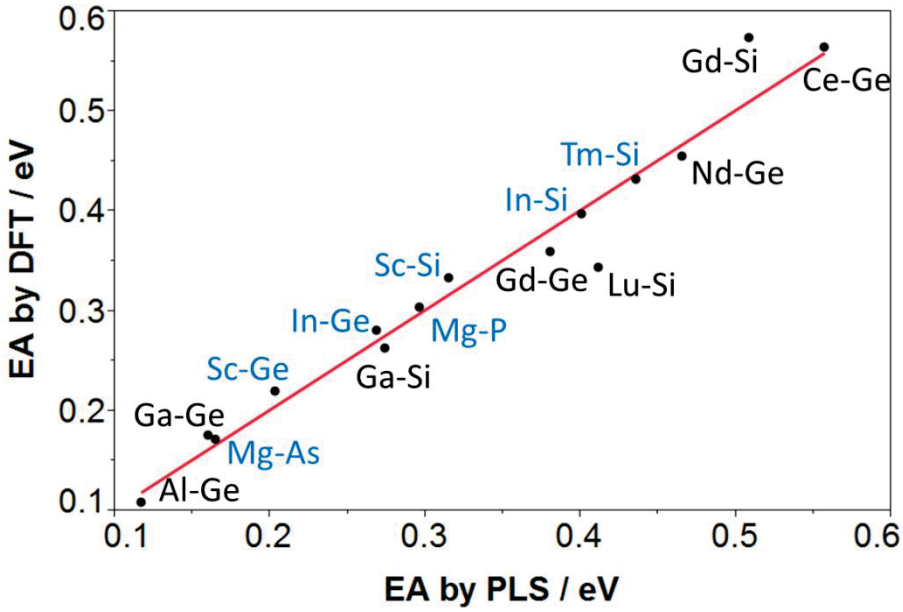

Figure 3-10. Fitting quality of PLS model-predicted EA for different $LiMXO_4$ compositions with respect to DFT EA values. Blue data points represent compositions with published experimental data in ICSD.

In order to validate the prediction model for EA, a test dataset was evaluated using compositions that were not included in the actual model building. The results are listed in Table 3-3 for the DFT-derived and PLS-derived EA values and their energy differences. Indeed, there is a significant predictive power based from the five tested samples, namely, $LiAlSiO_4$, $LiDyGeO_4$, $LiYSiO_4$, $LiHoSiO_4$, and $LiSmGeO_4$. The energy difference between DFT and PLS results falls within 35 meV. Among the compositions, $LiAlSiO_4$ is of practical interest for experimental testing due to the low EA (~0.2 eV) and cheap constituent elements.

Table 3-3. Comparison of DFT-derived and PLS-derived EA values for M−X pairs which are excluded from the model building step.

Composition	EA (eV)		
	DFT	PLS	difference
$LiAlSiO_4$	0.1958	0.2296	-0.03379
$LiDyGeO_4$	0.3366	0.3388	-0.00225
$LiYSiO_4$	0.5150	0.4824	-0.03253
$LiHoSiO_4$	0.4773	0.4552	+0.02526
$LiSmGeO_4$	0.3937	0.4190	-0.02526

After model has been test and validate, EA prediction can now be performed for the rest of the $LiMXO_4$ compositions. The results are displayed in Figure 3-11, with data points sorted according to the M and X ionic radii. The plot shows the dependence of the Li-ion hopping energy on the ionic size of M and X. An increase in the size of M increases the EA, whereas an increase in the size of X leads to a decrease in EA. Collectively, results from both DFT calculations and PLS predictions showed low EA values for small-sized Group 13 M cations (Al and Ga). Large-sized Group 2 cations (Sr and Ba) and most lanthanide ions gave large barrier energy values. With respect to our benchmark material, $LiAlSiO_4$, $LiAlGeO_4$, $LiGaSiO_4$, $LiGaGeO_4$ and LiGaSnO4 can be treated as candidate materials with predicted EA values of 0.23, 0.12, 0.28, 0.16, and 0.01 eV, respectively. From the standpoint of mineral resource abundance, compositions containing Al and Si should be regarded as a priority for new material synthesis.

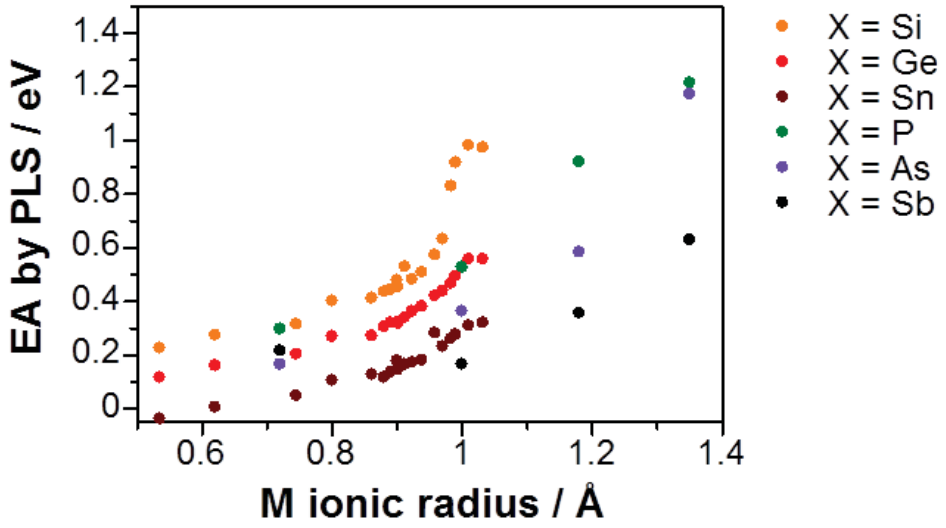

Figure 3-11. PLS model-predicted EA for different $LiMXO_4$ compositions sorted with respect to X cation type.

Since the prediction for EA was initially based on model training with 42 OVs, it is apparent that analyzing the underlying structure of the PLS model becomes an arduous task. Therefore, OVs that are of low importance should be identified and removed from the model itself and this can be carried out by evaluating two important criteria: one is the OV absolute coefficients used to fit the DFT EA values and the other one is the parameter for variable importance in projection (VIP) for the LV construction [38]. The model coefficient plot and VIP plot for the reduced final model (only 33 OVs left) are illustrated in Figures 3-12a and 3-12b, respectively. In here, there is no appreciable change observed after deletion of unimportant OVs to the ordering of VIP between the first and the reduced final model.

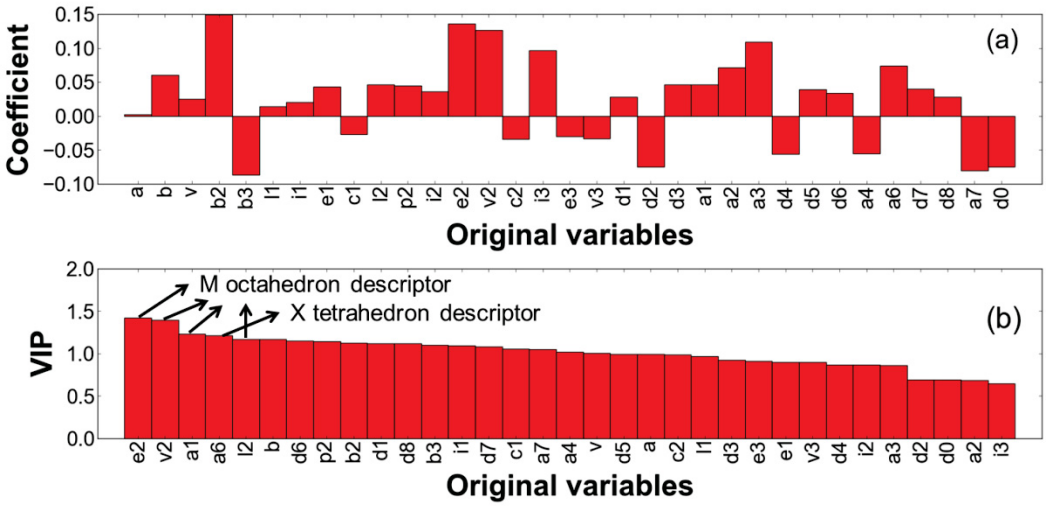

Figure 3-12. (a) Model coefficient plot and (b) variable importance in projection (VIP) plot of the remaining 33 original variables for the final PLS model (9 deleted unimportant variables).

Another merit of PLS-based modeling is the built-in procedure for deducing factors that directly affect the EA value from the list of OVs used. In the present model, major contributions to EA primarily came from M octahedron descriptors, as based on Figure 3-12, the three highest OVs are e2 – quadratic elongation for M octahedron, v2 – bond angle variance of the M octahedron, and a1 – Li−O−M angle at the edge-sharing octahedra along the diffusion channel. It is also worth noting that, according to the X-loading plots in Figure 3-13, LV1, which contributes the largest magnitude for EA, has been built from OVs that are also closely related to M octahedron descriptors. These agree well with our proposed crucial parameter for Li-ion migration, which is the local lattice distortion around the M octahedron.

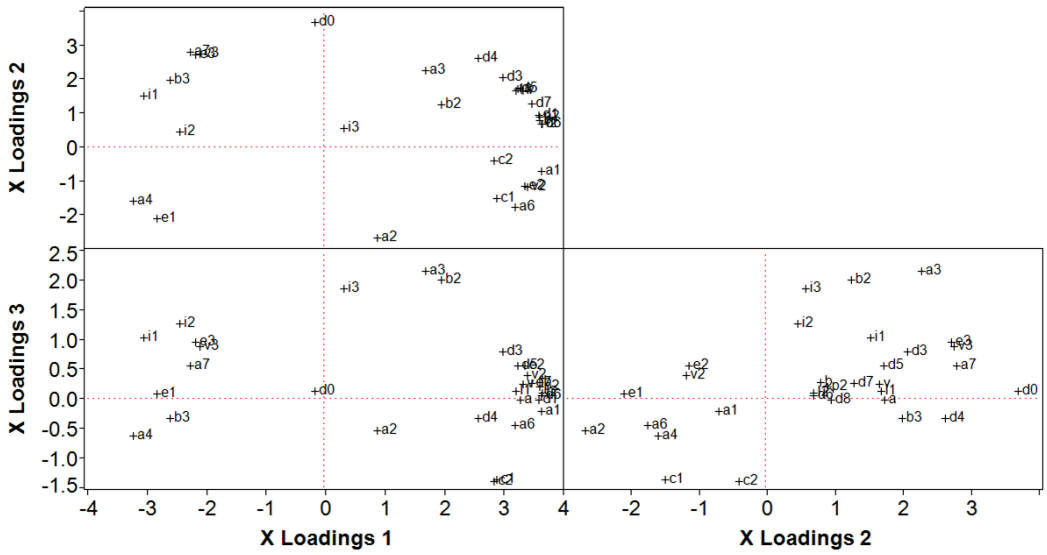

Figure 3-13. X loading plots for the final PLS-derived model for EA showing contribution of the OVs to the three latent variables (LVs), namely: LV1 (X Loadings 1), LV2 (X Loadings 2), and LV3 (X Loadings 3), respectively.

3-5. Conclusions

In summary, a robust model for the prediction of the Li ion hopping energies (EAs) within the olivine-type $LiMXO_4$ search space was successfully formulated using a combination of *ab initio*-based methods and PLS technique. Specifically, the following results are determined in the study:

1) An increase in the ionic size of M results in a significant distortion of the M octahedron, which, in turn, leads to an increase in the energy-penalizing local lattice distortion around the migration pathway and during the actual Li ion hop.
2) Promising compositions with low EA values (< 0.30 eV) include ICSD-reported materials such as $LiMgAsO_4$, $LiScGeO_4$, $LiInGeO_4$, and $LiMgPO_4$, and virtual compositions such as Li(group 13)XO_4 and $LiCaXO_4$.
3) Original variables (OVs) that have major contribution to the value of EA belong to M octahedron descriptors such as e2 – quadratic elongation for M octahedron, v2 – bond angle variance of the M octahedron, and a1 – Li−O−M angle at the edge-sharing octahedra along the diffusion channel.

3-6. Future work and direction

The following points are the suggested for the future work of the study:

1) Systematic survey of suitable dopants (low solution energies) for the identified candidate olivine-type $LiMXO_4$ solid electrolytes in order to activate their intrinsic fast Li ion conduction.
2) Computational phase stability studies of identified candidate olivine-type $LiMXO_4$ compositions.

3-7. Chapter references

1. V. Thangadurai, W. Weppner, Adv. Funct. Mater. 2005, 15, 107.
2. Y. Inaguma, C. Liquan, M. Itoh, T. Nakamura, T. Uchida, H. Ikuta and M. Wakihara, M. Solid State Commun. 1993, 86, 689.
3. U. V. Alpen, H. Schulz, G. H. Talat and H. Böhm, H. Solid State Commun. 1977, 23, 911.
4. H. Y. –P. Hong, Mater. Res. Bull. 1978, 13, 117.
5. J. B. Goodenough, H. Y. –P. Hong and J. A. Kafalas, Mater. Res. Bull. 1976, 11, 203.
6. J. T. S. Irvine, A. R. West, in High Conductivity Solid Ionic Conductors, Takahashi, T., Ed., World Scientific Publishing Co.: Singapore, 1989.
7. B. Kang and G. Ceder, Nat. Lett. 2009, 458, 190.
8. F. E. Zhou, M. Cococcioni, K. Kang and G. Ceder, Electrochem. Commun. 2004, 6, 1144.
9. M. S. Islam, D. J. Driscoll, C. A. J. Fisher and P. R. Slater, Chem. Mater. 2005, 17, 5085.
10. D. Dai and M. –H. Whangbo, Inorg. Chem. 2005, 44, 2407.
11. C. H. Spiegelman, J. F. Bennett, M. Vannucci, M. J. McShane and G. L. Cote, Anal. Chem. 2000, 72, 135.
12. F. Marini, A. Roncaglioni and M. J. Novič, Chem. Inf. Model. 2005, 45, 1507.
13. K. Sunnerheim, A. Nordqvist, G. Norlander, A. –K. B. Karlson, C. R. Unelius, B. Bohman, H. Nordenhem, C. Hellqvist and A. J. Karlén. Agric. Food Chem. 2007, 55, 9365.
14. A. Lorber, L. E. Wangen and B. R. Kowalski, J. Chemometrics 1987, 1, 19.
15. M. Haenlein, Und. Stat. 2004, 3, 283.
16. G. Kresse and D. Joubert, Phys. Rev. B 1998, 59, 1758.
17. G. Kresse and J. Furthmüller, Phys. Rev. B 1996, 54, 11169.
18. ICSD, Inorganic Crystal Structure Database; http://icsd.fizkarlsruhe.de/icsd/, 2006.
19. G. I. Csonka, J. P. Perdew, A. Ruzsinszky, P. H. T. Philipsen, S. Lebègue, J. Paier, O. A. Vydrov and J. G. Ángyán, Phys. Rev. B 2009, 79, 155107-1.
20. H. Jonsson, G. Mills and K. M. Jacobsen, K. M. Nudged Elastic Band Method for Finding Minimum Energy Paths of Transitions, in Classical and Quantum Dynamics in Condensed Phase Simulations; B. J. Berne, G. Ciccotti and D. F. Coker, Eds.; World Scientific: Singapore, 1998.
21. I. Kishida, Y. Koyama, A. Kuwabara, T. Yamamoto, F. Oba and I. Tanaka, J. Phys. Chem. B 2006, 110, 8262.

22. R. D. Shannon, Acta Crystallogr., Sect. A: Cryst. Phys. Diffr., Theor. Gen. Crystallogr. 1976, 32, 751.
23. K. Robinson, G. V. Gibbs and P. H. Ribbe, Science 1971, 172, 567.
24. D. Morgan, A. Van der Ven and G. Ceder, Electrochem. Solid-State Lett. 2004, 7, A30.
25. S. Nishimura, G. Kobayashi, K. Ohoyama, R. Kanno, M. Yashima and A. Yamada, Nat. Mater. 2008, 7, 707.
26. R. Malik, D. Burch, M. Bazant and G. Ceder, Nano Lett. 2010, 10, 4123.
27. J. Yang and J. S. Tse, J. Phys. Chem. A 2011, 115, 13045.
28. P. Ghosez, J. –P. Michenaud and X. Gonze, Phys. Rev. B 1998, 58, 6224.
29. M. Veithen and P. Ghosez, Phys. Rev. B 2002, 65, 214302.
30. W. Zhong, R. D. King-Smith and D. Vanderbilt, Phys. Rev. Lett. 1994, 72, 3618.
31. T. Rajkumar, M. Nakayama and M. Nogami, Solid State Commun. 2010, 150, 693.
32. K. T. Fehr, R. Hochleitner, E. Schmidbauer and J. Schneider, Phys. Chem. Miner. 2007, 34, 485.
33. S. F. Yang, Y. N. Song, P. Y. Zavalij and M. S. Whittingham, Electrochem. Commun. 2002, 4, 239.
34. G. Hautier, C. Fischer, V. Ehrlacher, A. Jain and G. Ceder, Inorg. Chem. 2011, 50, 656.
35. G. Hautier, C. Fischer, A. Jain, T. Meuller and G. Ceder, Chem. Mater. 2010, 22, 3762.
36. S. M. Woodley and R. Catlow, Nat. Mater. 2008, 7, 937.
37. P. Geladi and B. R. Kowalski, Anal. Chim. Acta 1986, 185, 1.
38. I. –G. Chong, C. –H. Jun, Chemom. Intell. Lab. 2005, 78, 103.

Chapter 4. Multivariate method-assisted *ab initio*-based new material search of tavorite-type $LiMXO_4F$ solid electrolytes

4-1. Background of the study

Similar with Chapter 3, this study aims to find new solid electrolytes by taking inspiration from structural frameworks that forms naturally in the earth's crust. Recent studies have reported tavorite-type structures as candidate battery materials [1-2]. This class of materials has the general formula $AMTO_4X$, where A is occupied by an alkali or alkaline-earth element, M is a metal, T is a p-block element, and X can be any anion such as O, F, or OH. It is characterized by MO_4X_2 octahedron and TO_4 tetrahedron that are alternately vertex-linked to form chains in one dimension. So far, most evaluated compositions in this group are those with transition metals that can form redox couples and were intended as cathodes [3-9]. Logical solid electrolyte candidates would be those analogs without transition metals such as $LiAlPO_4F$ and $LiMgSO_4F$ [10,11]. Figure 4-1 shows the schematic view of the tavorite structure $LiMXO_4F$. In this illustration, the Li cations are disordered at half occupancy in splitting sites within the framework tunnels defined by MO_4F_2 and PO_4 polyhedra. At present, tavorite materials with nontransition metals have not yet been intensively investigated and their Li ionic conduction behavior is still poorly understood. So far, only the Li ion conduction in $LiMgSO_4F$ has been reported with experimental measurement, showing poor conductivity with an order of 10-3 S/cm (~800 K) and activation energy of 0.94 eV [11].

This chapter deals with the efficient exploration of the tavorite-type $LiMXO_4F$ chemical search space by combining *ab initio*-based calculations and neural networks in order to determine compositions that are potential for solid electrolyte application in an all-solid state Li ion battery set-up. The search criterion will be based on the Li diffusion barrier of the representative bottleneck pathway within the tavorite framework. The compositions that will be evaluated would be based on main group M octahedral atoms (group 2, group 3, lanthanides, and group 13) and X tetrahedral atoms (group 15 and group 16), leading to, again, a total of 72 compositions.

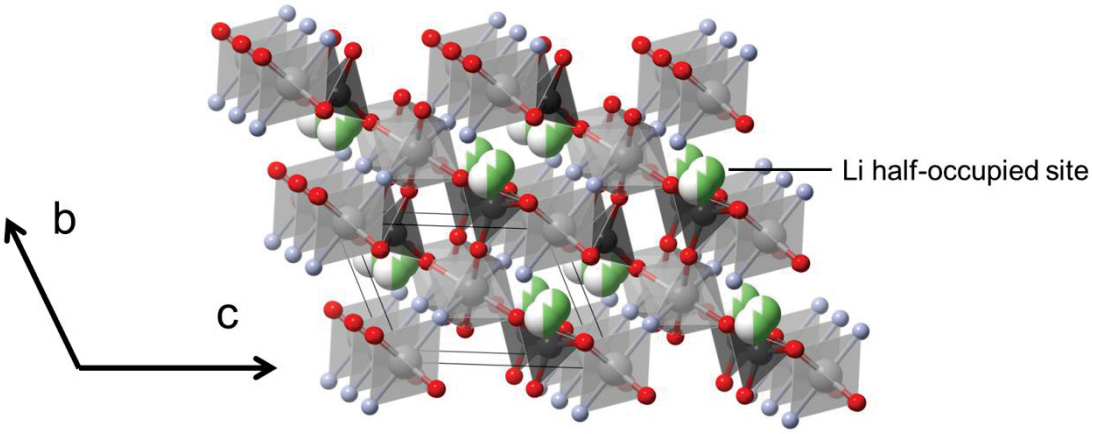

Figure 4-1. Schematic view of the tavorite structure. Green/white spheres are half occupied Li/vacancy atoms arranged in a zigzag manner along the a-channel, light gray octahedra are MO_4F_2 units, and dark gray tetrahedra are XO_4 units.

4-2. Multivariate method: neural network (NN) analysis

Another information processing or prediction modeling tool is the neural network (NN) method. It mimics the learning process of the human brain with its interconnected assembly of simple processing elements called neurons or nodes. The processing ability of the network is stored in connection weights obtained by a process of learning from a set of training patterns. A typical NN architecture is the single hidden layer feed-forward NN described by the statistical formula:

$$\hat{Y}_l = \sigma^{(2)}\left(\sum_{k=1}^{K} w_{2kl}\sigma^{(1)}\left(\sum_{j=1}^{J} w_{1jk}X_j + \theta_j\right) + \theta_k\right) \quad (4\text{-}1)$$

where $\hat{Y}_l$ is the predicted dependent or response variable set, $\theta^{(1)}$ and $\theta^{(2)}$ are the activation functions, θ_j and θ_k are the intercept values (constant) in the model, w_{1jk} and w_{2kl} are the connection weights for the hidden output layers and response output layers, respectively, and X_j is the independent or input variable set. In the hidden and output layers, the inputs for the basis functions are given by:

$$v_k = \sum_{j=1}^{J} w_{1jk}X_j + \theta_j \quad \text{and} \quad (4\text{-}2)$$

$$v_l = \sum_{k=1}^{K} w_{2kl}\sigma^{(1)}(v_k) + \theta_k, \quad (4\text{-}3)$$

respectively. One of the learning algorithms employed is the back-propagation technique. This approach compares the network output to the target output, and the randomly initialized weights are updated accordingly in the direction so as to reduce the error between them. The forward pass generates the network's output activities and is generally the least computation-intensive but the more time consuming backward pass involves propagating the error initially found in the output node back through the network to assign errors to each preceding nodes that contributed to the initial error; the goal here is to minimize this error value summation until a predetermined threshold is met:

$$e_l = Y - \hat{Y}_l \quad (4\text{-}4)$$

$$E_l = {e_l}^2/2 \quad (4\text{-}5)$$

where *e* is the actual error and *E* is the sum of square error for the target output value *y*. From here, the weights w_{2kl} at the hidden layer are updated by gradient descent based on the calculated E_l. Applying chain rule:

$$\partial E_l/\partial w_{2kl} = (\partial E_l/\partial e_l)(\partial e_l/\partial \hat{Y}_l)(\partial \hat{Y}_l/\partial v_l)(\partial v_l/\partial w_{2kl}) \quad (4\text{-}6).$$

Equation 4-6 can be simplified with:

$$\partial E_l/\partial e_l = e_l \quad (4\text{-}7)$$

$$\partial e_l/\partial \hat{Y}_l = -1 \quad (4\text{-}8)$$

$$\partial Y_l/\partial v_l = d[\sigma^{(2)}(v_l)]/dv_l = \sigma'(v_l) \quad (4\text{-}9)$$

$$\partial v_l / \partial w_{2kl} = \sigma^{(2)}(v_l) \tag{4-10}$$

Thus, the change in E_l with respect to w_{2kl} becomes:

$$\partial E_l / \partial w_{2kl} = -e_l \sigma'(v_l) \sigma^{(2)}(v_l) \tag{4-11}$$

From equation 11, the weights can be updated by:

$$\Delta w_{2kl} = -\eta(\partial E_l / \partial w_{2kl}) = \eta e_l \sigma'(v_l) \sigma^{(2)}(v_l) = \eta \delta_l \sigma^{(2)}(v_l) \tag{4-12}$$

with the local gradient at the node:

$$\delta_l = e_l \sigma'(v_l) \tag{4-13}$$

where Δw_{2kl} is the weight change from hidden layer node k to output layer node l, η is the learning rate which much be $0 < \eta \leq 1$, and δ_l is the local gradient at the output layer node l. Meanwhile, the local gradient δ_k for the hidden layer nodes can be derived as:

$$\delta_k = -\partial E_l / \partial v_k = -[\partial E_l / \partial \sigma^{(1)}(v_k)][\sigma'(\sigma^{(1)}(v_k)] \tag{4-14}$$

With E_l taken from the output layer:

$$E_l = 1/2 \, (\textstyle\sum_l e_l{}^2) \tag{4-15}$$

The derivative $\partial E_l / \partial \sigma^{(1)}(v_k)$ can be evaluated as:

$$\partial E_l / \partial \sigma^{(1)}(v_k) = \textstyle\sum_l e_l \, (\partial e_l / \partial v_l) \, (\partial v_l / \partial \sigma^{(1)}(v_k)) \tag{4-16}$$

where:

$$\partial e_l / \partial v_l = \partial (Y - \hat{Y}) / \partial v_l = -\partial \hat{Y} / \partial v_l = -\sigma'(v_l) \tag{4-17}$$

and at a particular single node at the output layer:

$$\partial v_l / \partial \sigma^{(1)}(v_k) = \partial (w_{2kl} \sigma^{(1)}(v_k) / \partial \sigma^{(1)}(v_k) = w_{2kl} \tag{4-18}.$$

Parallel with equation 15, the expression becomes:

$$\partial E_l / \partial \sigma^{(1)}(v_k) = -\textstyle\sum_l e_l \sigma'(v_l) w_{2kl} = -\sum_l \delta_l w_{2kl} \tag{4-19}.$$

Applying equation 19 to 14:

$$\delta_k = \sigma'(v_k) \textstyle\sum_l \delta_l w_{2kl} \tag{4-20}$$

Finally, the weights for hidden layer are updated similar to equation 11 by:

$$\Delta w_{1jk} = \eta \delta_k \sigma^{(1)}(v_k) \tag{4-21}.$$

Figure 4-2 shows the schematic outline of a three-layer feed-forward NN architecture [12].

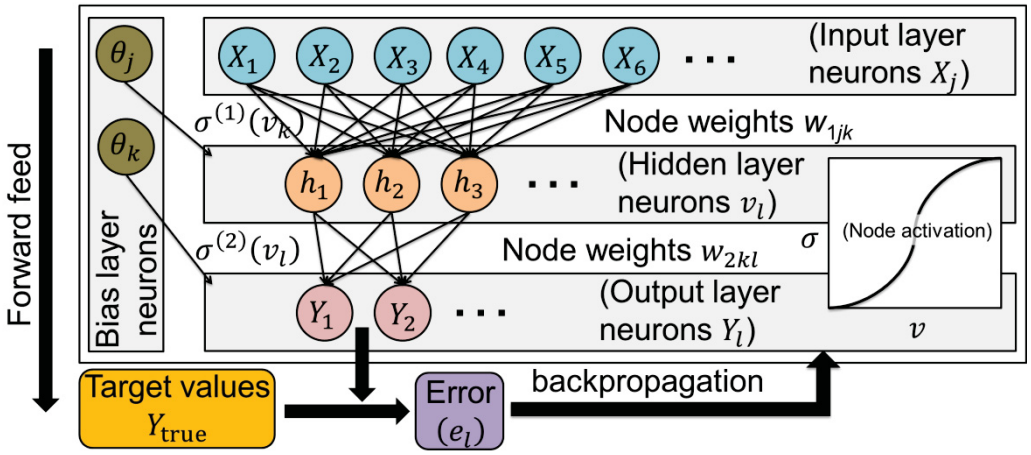

Figure 4-2. A three layer $(j-k-l)$ feedforward neural network architecture. The circles are assigned as computational nodes which integrate input from the preceding layer and transmit a signal to the next layer. Arrows represent weighted connections (w_{1jk} and w_{2kl}) between nodes. Modulation of incoming signals is carried out by activation functions σ.

4-3. Computational details

Atomistic modeling was initialized within the density functional theory (DFT) framework using projected augmented wave (PAW) method [13] as implemented in Vienna *Ab Initio* Simulation Package (VASP) [14]. Standard generalized gradient approximation (GGA) using the parametrization of Perdew−Burke−Ernzernhof for solids (PBEsol) was used for the exchange correlation energy [15]. Published structural information on experimentally synthesized ordered tavorite compounds were taken from the Inorganic Crystal Structure Database (ICSD) [16]. For the virtual compositions, the coordinate set from the reported ones were used as template for the subsequent relaxation and evaluation of Li diffusion barrier. Figure 4-3 shows the different M-X pairs considered in the study. Spin-polarized calculation with an energy cutoff of 500 eV was carried out and allowed the total energies to converged within 3 meV per formula unit (f. u.). A 5 × 4 × 3 Monkhorst-Pack kpoint grid in a 16-atom unit cell showed a reasonable convergence and an error of <1 meV/f. u. in the total energy. Berry phase method was used for the Born effective charge calculation in order to evaluate ionicity/covalency of cation bonds [17]. The nudged-elastic-band (NEB) method [18] was used to determine migration pathway and energy; the calculation was done with a 1 × 2 × 2 supercell. Numerical integration was performed over the Brillouin zone by sampling the Γ-point. Convergence was determined to be within 30 meV/f. u.

For the NN architecture, a single hidden layer network with 3 hidden nodes and a single external attribute (EA) is evolved with a fixed learning rate of η = 0.1 [19]. The partition for the training set is 2/3 of the total sampled compositions and the remaining 1/3 is allocated for the validation set. The training order (combinations for the training and validation sets) is randomly varied for 6 times during the model building step. About 20 compositions are initially used for EA sampling. The data set is preprocessed by standardization (mean = 0 and standard deviation = 1) to equalize the scaling; this allows the assignment of the excitatory or inhibitory effects to the correct outputs.

A hyperbolic tangent function is used for node activation [20]:

$$(e^{2v} - 1)/(e^{2v} + 1), \tag{4-22}$$

where v is described in equations 4-2 and 4-3. This transforms values between -1 and 1, and is the centered and scaled form of the logistic function. In order to mitigate the overfitting and ensure that the final model can be generalized to cases it has not been trained on, a penalty term for the error function is introduced during training using the expression [21]:

$$P = \lambda p(\beta_i), \tag{4-23}$$

where P is the penalty function, λ is a small positive weight decay constant based on the generalization error derived using the first validation set, $p(\beta_i)$ is the function of the parameter estimates, and β_i is the weight for i neural nodes, which includes that for the hidden and output layers. The absolute penalty function is used with $p(\beta_i)$ [22],

$$p(\beta)_i = \sum |\beta_i|. \quad (4\text{-}24)$$

Because there is no *a priori* knowledge of the number of local minima on the error landscape [23], it is crucial that sufficient sampling is conducted aside from varying the training order. Therefore, the fitting process is restarted 10,000 times for each training order and using different random starting points for the node weights. The penalty function (equation 7) ensures that variables which contribute more than the others to the predictive ability of the model are weighted more, whereas the other functions are reduced to zero. Hence, this term can also minimize the influence of highly collinear variables on the final model.

During training and out-of-sample validation, the models are evaluated using the coefficient of determination, R^2, which is the proportion of the variability in a data set that is accounted for by the statistical model, and the root mean square error (RMSE), which is the difference between the values predicted by the model and the values actually observed. The equations describing R^2 and RMSE are as follows:

$$R^2 = 1 - (\sum_{i=1}^{n}(y_i - \hat{y}_i)/\sum_{i=1}^{n}(y_i - \bar{y})) \quad (4\text{-}25),$$

$$\mathrm{RMSE} = [(\sum_{i=1}^{n}(y_i - \hat{y}_i)^2/n]^{1/2} \quad (4\text{-}26),$$

where y_i is the accurate DFT external attributes (EA, CE), $\hat{y}_i$ is the external attributes predicted by multivariate modeling, and $\bar{y}$ is the mean external attribute values, for n samples. The calculated RMSE is also called the cross-validation (CV) score for the out-of-sampling estimates. The convergence criterion is set relative to the change in the value of the objective function, stopping the iteration when the error falls below 10^{-8} eV. The run with the best validation statistic is then chosen as the final model.

The causal index (CI) method [24] is used for analyzing input variable relevance. The CI method is a qualitative, heuristic approach for rule extraction, expressed by

$$\mathrm{CI} = \sum_{k=1}^{h} w_{lk} w_{kj}, \quad (4\text{-}27)$$

where h is the number of hidden nodes, w_{lk} are weights linking the hidden node k to the output node l, and w_{kj} are the weights linking input node j to hidden node k. The indices reveal the direction (positive or negative) and relative contribution of each input variable to a given output.

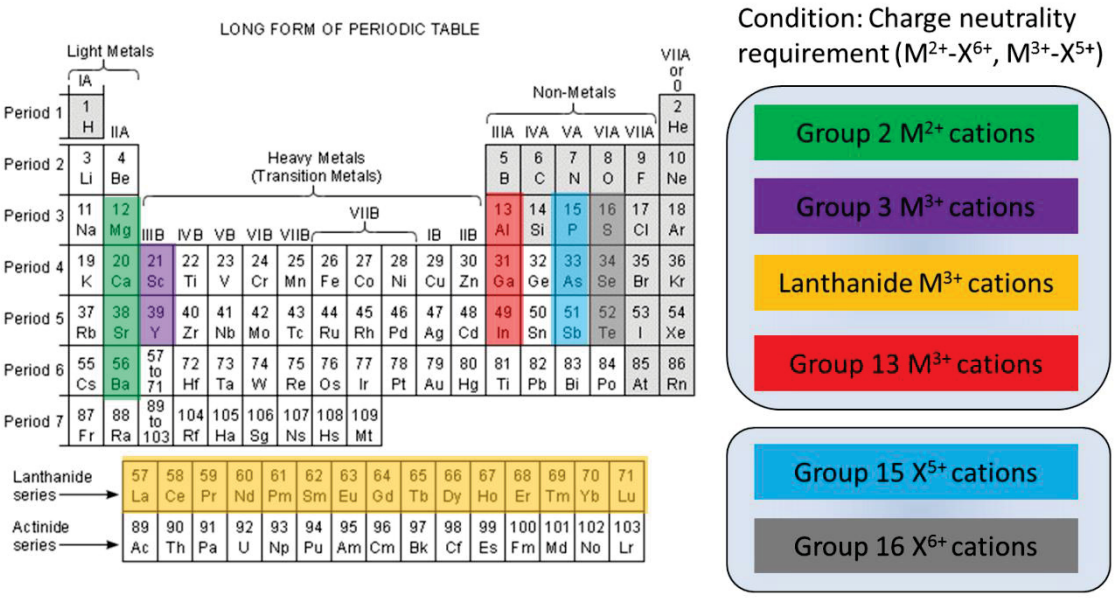

Figure 4-3. Sampling of the tavorite-type $LiMXO_4F$ search space.

4-4. Results and discussion

4-4-1. Structural variation across the tavorite-type $LiMXO_4F$ search space

Figure 4-4a shows the direct relationship between the unit-cell volume and the ionic size (Shannon radii) of the inserted cations in both the M and X sites. Except for lattice parameter a, a strong positive correlation is observed for volume, b, and c with M ionic size. The largest volume was determined for $LiBaTeO_4F$ (250.37 $Å^3$), and the smallest volume was found for $LiAlPO_4F$ (159.04 $Å^3$). The main cluster of data points from 0.88 – 1.03 Å M ionic size belongs to pairs containing rare-earth cations. However, an exception within this cluster of points is noticeable, i.e., a discontinuity in the trend is observed for compositions containing the elements of the second half of the rare earth cation group and Sb tetrahedral cation. This can be attributed to the severe distortion in these aforementioned compositions due to the simultaneous accommodation of large-sized M and X cations. As a consequence, their symmetry may have already diverge from a typical tavorite configuration. For example, structural relaxation of $LiLaSbO_4F$, a terminal point in the cluster of rare earth-containing compositions, has led to Sb^{5+} which is supposed to assume a tetrahedral coordination has moved significantly so that it is now in either a five-fold or six-fold instead coordination. Looking into the component lattice parameter values, the increasing trend found in cell volume with increasing M ionic size for the majority of compositions can be traced back to lattice parameters b and c. Meanwhile, the discontinuous plot in cell volume is noted to be primarily contributed by lattice parameter c.

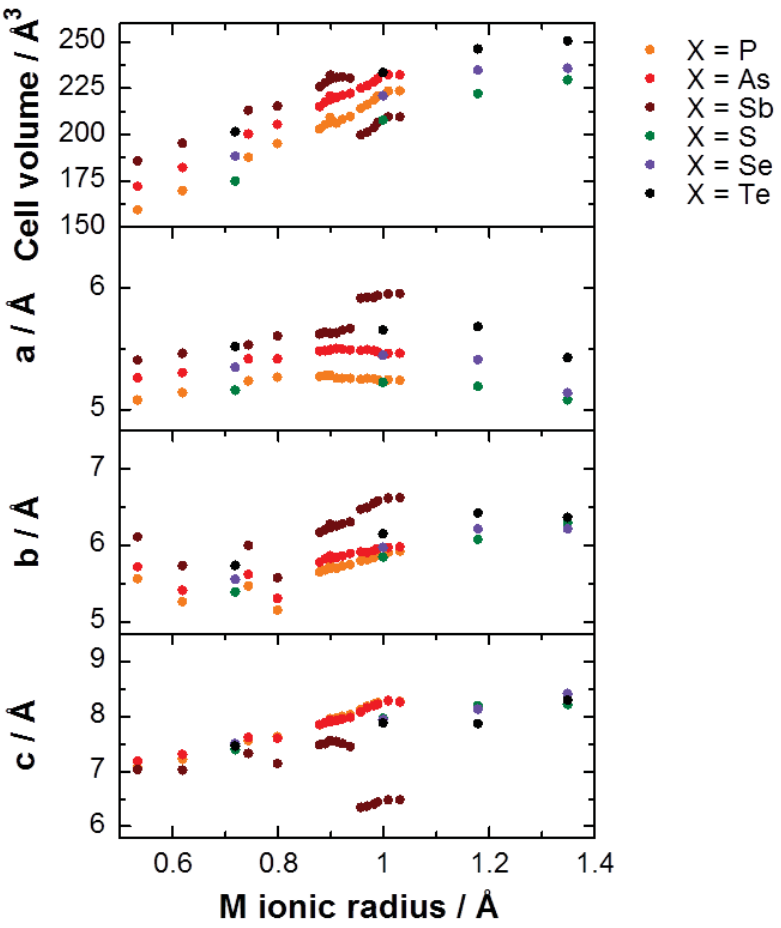

Figure 4-4. Structural data across the olivine $LiMXO_4F$ search space: (a) cell volume, (b) lattice parameter a, (c) lattice parameter b, and (d) lattice parameter c of the DFT-relaxed structures, sorted according to X tetrahedral cation.

4-4-2. Li ion diffusion within the tavorite framework

The Li ion hopping energy (EA) criterion is again used in the subsequent analysis and evaluation of the tavorite $LiMXO_4F$ space. For this, it is necessary that the different main pathways for Li migration in the tavorite structure are investigated first in order to draw conclusions as to which pathway(s) can be used as representative(s) for the calculation of EA. In connection to this, two compositions are studied, namely: $LiAlPO_4F$ and $LiMgSO_4F$; these two materials are reported in the ICSD database. The relevant pathways are shown in Figures 4-5a and 4-5b, respectively. Upon inspection, four paths are needed for a complete connectivity and Li long-range diffusion along the open tunnels of the tavorite structure. These paths can be characterized as XO_4-XO4 tetrahedral face pair sandwich path (path 1 in Fig. 4-5a, path 1 in Fig. 4-5b, path 4 in Fig. 4-5a, path 3 in Fig. 4-5b) and MO_4F_2-MO_4F_2 octahedral face pair sandwich path (path 2 in Fig. 4-5a, path 2 in Fig. 4-5b, path 3 in Fig. 4-5a, path 4 in Fig. 4-5b). Starting at one Li site, there are four neighboring unique jump sites are available for a moving Li, i.e., two along [100] and another two along [010]. When the energy profiles of these paths are plotted, a comparison can be made in order to identify highly unlikely paths, bottleneck paths, and highly favorable paths. The results are displayed in Fig. 4-5 for the two investigated materials. The potential energies at several points along the projected migration distance are plotted and the highest point determines the value of EA for a particular path. In both $LiAlPO_4F$ and $LiMgSO_4F$, the pathway which passes the XO_4-XO_4 tetrahedral face pair sandwich are found out to be strongly penalized for Li migration due to the high EA values (0.89-1.34 eV) while the pathway via MO_4F_2-MO_4F_2 octahedral face pair sandwich has lower EA values (<0.55 eV). This suggests that Li mobility should proceed mainly in one dimension (1D), i.e., path 2-path 3-path2-… zigzag along [001] in $LiAlPO_4F$ (Fig. 4-4a) and path 2-path 4-path 2-… zigzag along [111] in $LiMgSO_4F$ (Fig. 4-4b). In addition, the bottleneck of this 1D pathway is determined by path 2 in both compositions with values of 0.55 and 0.20 eV, respectively. The difference in the estimated EA in the two topologically identical paths (path 2 and path 3 in $LiAlPO_4F$, path 2 and path 4 in $LiMgSO_4F$) comprising the 1D channel can be ascribed to the staggered configuration of MO_4F_2 octahedra that delimits cavities and the Li disordering between two half-occupied sites. Interestingly enough, this 1D-type diffusion is also observed in olivine-type materials [25-26], particularly the $LiFePO_4$ composition which is reported to

demonstrate ultrafast charging and discharging capabilities [27].

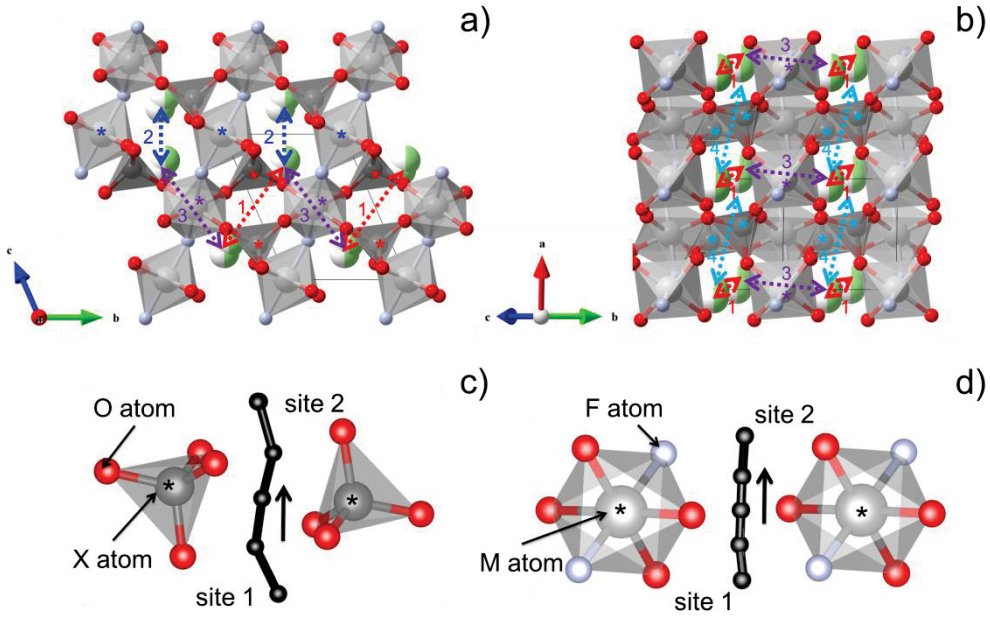

Figure 4-5. Planar view on a) (100) plane and b) (011) plane for the tavorite structure. Possible Li paths are shown as colored dashed lines. The local environment can be distinguished as passing through: c) XO_4-XO_4 tetrahedral pair (path 1 and path 4) or d) MO_4F_2-MO_4F_2 octahedral pair (path 2 and path 3).

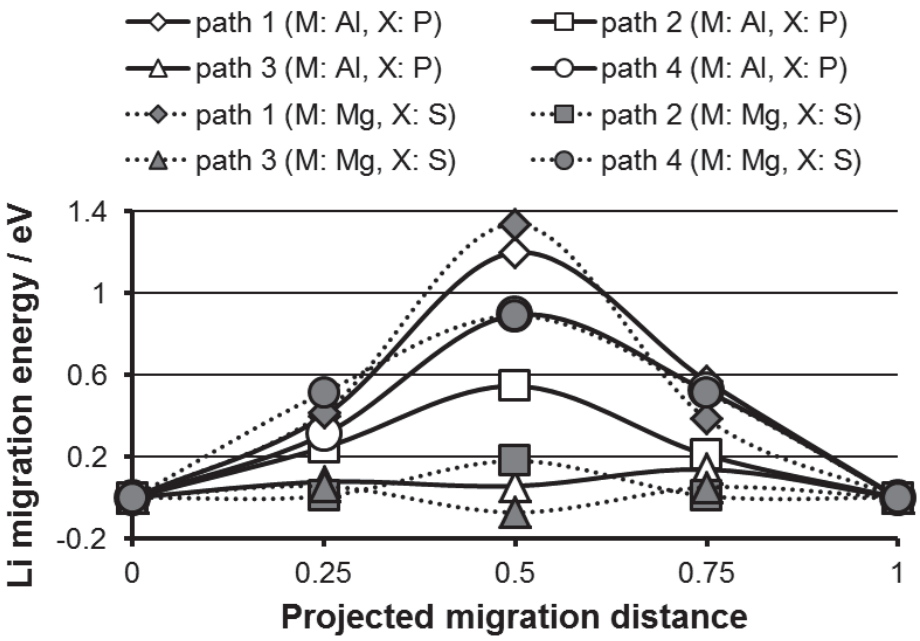

Figure 4-6. Energy profiles of ICSD-derived $LiMXO_4F$ compositions (from NEB method).

Preliminary analysis of the crucial factors for EA within the tavorite structure is carried out using the ICSD-reported $LiAlPO_4F$ and $LiMgSO_4F$. The simple increase in local tunnel size (from AlO_4F_2 pair to MgO_4F_2 pair) should decrease the short-range repulsive interaction arising from electron cloud overlap in the jump vicinity; Al-Al and Mg-Mg distances for the bottleneck path 2 are 5.15 and 5.41 Å, respectively. Another factor is the effect of strong bond directionality in XO_4 tetrahedra (from PO_4 to SO_4). Table 4-1 highlights the Born effective charge tensor data for the cations in $LiAlPO_4F$ and $LiMgSO_4F$. Nominal charges of Li, M, and X are +1, +3 (+2), and +5 (+6), respectively. For Li and M cation, Born effective charges (diagonal values) are relatively close to their nominal values which suggest strong ionic character of the Li/M-O bond. For Li cation, the charge is almost isotropic which is reflective of its low polarizability [28]. For M cation, the average effective charge is higher than its nominal charge and this can be owed to the polarizability of M and its partial covalent interaction with the oxide ion [29-30]. However, this is not the case for X cation in which the effective charge is significantly lower than nominal charge; this case indicates strong covalency in the X-O bond [31-32]. Tuning this covalency of the bonds in the polyanion may increase anion electronic polarizability and may reduce

Coulombic interaction effect between Li ion and the lattice. With the lower average Born effective charge for S^{6+} cation in $(SO_4)^{2-}$ than in P^{5+} cation $(PO_4)^{3-}$ polyanion relative to their nominal charges, the former is expected to have a stronger covalent character than the latter for bonding with oxide ion. Also, this degree of covalency in S-O bond should minimize more the interaction for the migrating Li with the lattice as the electron cloud from oxide ion in MO_4F_2 (c.f. path 2) are drawn more towards $(SO_4)^{2-}$ polyanion. This bond directionality should then as well directly affect sterically the MO_4F_2 octahedra via displacement of common and corner-shared oxide ions. Hence, weighing among the two factors mentioned for the two investigated materials, polyanion covalency is suggested as one of the major contributors towards EA variation.

Table 4-1. DFT-calculated Born effective (dynamic) charge (a. u.) tensors for cations in tavorite-type $LiAlPO_4F$ and $LiMgSO_4F$.

$LiAlPO_4F$				$LiMgSO_4F$			
Li	1.24	-0.04	0.04	Li	1.28	-0.02	-0.03
	-0.07	1.12	0.06		-0.08	1.03	-0.07
	0.04	0.09	1.06		-0.10	-0.07	1.07
Al_1	3.60	0.05	0.15	Mg_1	2.51	-0.02	-0.14
	0.11	2.84	-0.06		0.10	1.99	0.07
	-0.11	-0.46	3.04		0.14	0.41	2.17
Al_2	2.64	-0.18	-0.03	Mg_2	1.84	-0.14	0.04
	-0.02	3.70	-0.11		-0.03	2.64	0.13
	-0.37	0.12	3.17		0.31	-0.05	2.08
P	3.36	-0.04	-0.32	S	3.33	-0.02	0.26
	-0.12	3.24	-0.07		-0.08	3.08	0.04
	-0.08	-0.02	3.33		0.07	-0.01	3.27

The relevant equation for the Li ion diffusion coefficient for Li ion jumpis given by the equation [33-34]:

$$D = gv^{*}d^{2}\exp\left(\frac{-EA}{kT}\right) \quad (4\text{-}28)$$

where g is a geometric factor which is assumed to be unity, v^{*} is the Li ion jump pre-exponential factor which can be estimated by analyzing the potential profile curvature, d is the specific jump distance, k is the Boltzmann's constant, and T is the temperature of the system. Assuming T = 300 K, diffusion coefficient values for path 2 is around 10^{-12} and 10^{-5} cm^2/s for $LiAlPO_4F$ and $LiMgSO_4F$, respectively. These are also comparable with experimental measurements for a typical $LiCoO_2$ cathode which is in the range 10^{-11} – 10^{-13} cm^2/s [35-36]. A similar tendency is reported as well in previous studies conducted for transition metal-based tavorites [8, 9]. However, ME by impedance spectroscopy for $LiMgSO_4F$ was reported to be about 0.94 eV [11] which is sufficiently larger than the calculated bulk ME of 0.20 eV. This may be due to the following factors: i) some intrinsic defects which may cause blocking effects on the conduction path such as Li-M anti-site pair, or ii) penalty arising from Li vacancy creation which may be is a prerequisite before the actual Li ion conduction process could occur. As a whole, the conduction mechanism should be close to the predicted one and ME should be dominated by contribution from Li vacancy creation in conductivity measurements [37]. It may be beneficial to dope with aliovalent cations, targeting the M octahedral site in order to increase Li vacancies. Candidate dopants would be similar sized cations (≤ 1.15 factor of radius) such as Si^{4+} (0.4 Å), and Ge^{4+} (0.53 Å) for Al^{3+} (0.54 Å) and Sc^{3+} (0.75 Å), Al^{3+} (0.54 Å), Ga^{3+} (0.62 Å), and In^{3+} (0.8 Å) for Mg^{2+} (0.72 Å). We intend to carry out this doping strategy in order to activate the predicted bulk Li conductivity in these materials.

4-4-3. Prediction model building for EA

Structural information-related variables are extracted for the entire tavorite-type $LiMXO_4F$ search space (see Figure 3-2) for EA model building. For model training supervision, NEB-derived EA values based on the identified bottleneck pathway (path 2, see section 4-4-2) for a sample of stabilized compounds (20 M−X pairs) were calculated. The input variables extracted from DFT-relaxed unit cells can be categorized under the following: lattice parameters, Bader charges, Born effective charges, intra-polyhedron parameters, and inter-polyhedron parameters. For simplicity, the different input variables in here will be hereafter called original variables (OVs). The formalism for EA can then be constructed by neural network; for a model with a single hidden layer, the equation is similar to equation 4-1:

$$\mathrm{EA}_l = \sigma^{(2)}\left(\sum_{k=1}^{K} w_{2kl}\sigma^{(1)}\left(\sum_{j=1}^{J} w_{1jk}X_j + \theta_j\right) + \theta_k\right). \quad (4\text{-}29)$$

Details regarding the OVs are listed in Table 4-2. Visual representation for the inter-polyhedron-based variables within the tavorite structure is displayed in Figure 4-6.

Table 4-2. Description and code assignment for the different original variables taken from relaxed $LiMXO_4F$ unit cells.

Symbol	Description
a	lattice parameter a
b	lattice parameter b
c	lattice parameter c
alpha	lattice angle alpha
beta	lattice angle beta
gamma	lattice angle gamma
Volume	unit cell volume
bader1	M_1 cation Bader charge
bader2	M_2 cation Bader charge
bader3	X_1 cation Bader charge
bader4	X_2 cation Bader charge
bader5	O_1 anion Bader charge
bader6	O_2 anion Bader charge
bader7	O_3 anion Bader charge
bader8	O_4 anion Bader charge

bader9	O_5 anion Bader charge
bader10	O_6 anion Bader charge
bader11	O_7 anion Bader charge
bader12	O_8 anion Bader charge
bader13	F_1 anion Bader charge
bader14	F_2 anion Bader charge
bader15	Li_1 cation Bader charge
bader16	Li_1 cation Bader charge
b1	M_1 cation Born effective charge
b2	M_2 cation Born effective charge
b3	X_1 cation Born effective charge
b4	X_2 cation Born effective charge
b5	O_1 anion Born effective charge
b6	O_2 anion Born effective charge
b7	O_3 anion Born effective charge
b8	O_4 anion Born effective charge
b9	O_5 anion Born effective charge
b10	O_6 anion Born effective charge
b11	O_7 anion Born effective charge
b12	O_8 anion Born effective charge
b13	F_1 anion Born effective charge
b14	F_2 anion Born effective charge
b15	Li_1 cation Born effective charge
b16	Li_1 cation Born effective charge
avl1	average bond length of Li_1 octahedron
pv1	polyhedral volume of Li_1 octahedron
di1	distortion index of Li_1 octahedron
qe1	quadratic elongation of Li_1 octahedron
bav1	bond angle variance of Li_1 octahedron
ecn1	effective coordination number of Li_1 ion
avl2	average bond length of Li_2 octahedron
pv2	polyhedral volume of Li_2 octahedron
di2	distortion index of Li_2 octahedron
qe2	quadratic elongation of Li_2 octahedron
bav2	bond angle variance of Li_2 octahedron

ecn2	effective coordination number of Li_2 cation
avl3	average bond length of M_1 octahedron
pv3	polyhedral volume of M_1 octahedron
di3	distortion index of M_1 octahedron
qe3	quadratic elongation of M_1 octahedron
bav3	bond angle variance of M_1 octahedron
ecn3	effective coordination number of M_1 cation
avl4	average bond length of M_2 octahedron
pv4	polyhedral volume of M_2 octahedron
di4	distortion index of M_2 octahedron
qe4	quadratic elongation of M_2 octahedron
bav4	bond angle variance of M_2 octahedron
ecn4	effective coordination number of M_2 cation
avl5	average bond length of X_1 tetrahedron
pv5	polyhedral volume of X_1 tetrahedron
di5	distortion index of X_1 tetrahedron
qe5	quadratic elongation of X_1 tetrahedron
bav5	bond angle variance of X_1 tetrahedron
ecn5	effective coordination number of X_1 cation
avl6	average bond length of X_2 tetrahedron
pv6	polyhedral volume of X_2 tetrahedron
di6	distortion index of X_2 tetrahedron
qe6	quadratic elongation of X_2 tetrahedron
bav6	bond angle variance of X_2 tetrahedron
ecn6	effective coordination number of X_2 cation
inter1	M_2-F_2-M_1 angle
inter2	M_2-O_2-Li_1 angle
inter3	M_2-O_2-X_2 angle
inter4	M_1-F_1-M_2 angle
inter5	F_1-F_2-F_1’ angle (F_1’ at mirror unit cell)
inter6	M_2-F_2-Li_2 angle
inter7	M_1-F_2-Li_2 angle
inter8	M_2-M_2’ distance (M_2’ at mirror unit cell)
inter9	M_2-M_2 distance, third nearest neighbor M_2
inter10	M_2-X_1 distance

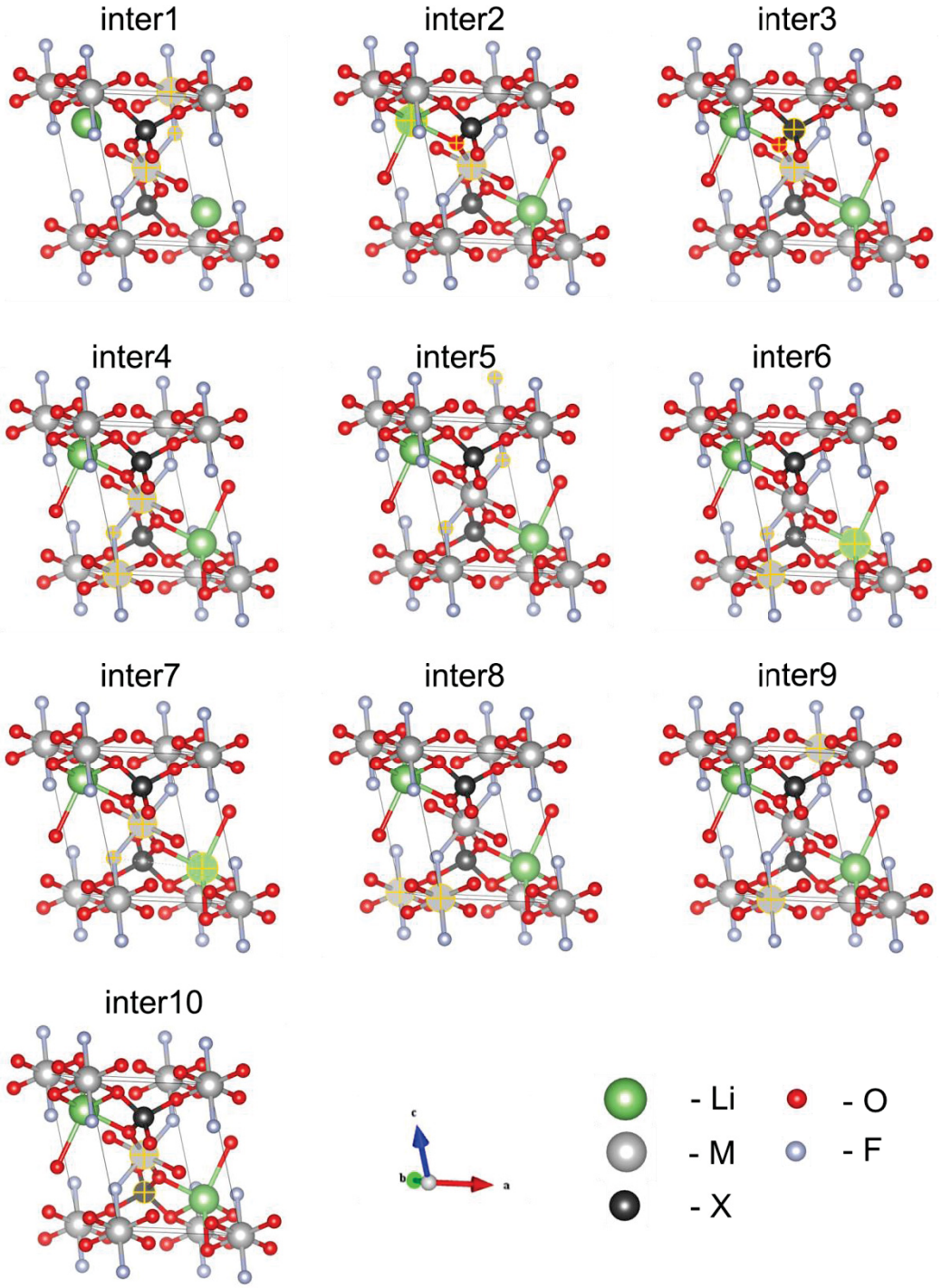

Figure 4-7. Inter-polyhedron parameters within the $LiMXO_4F$ unit cell that were used in EA model building (see Table 4-2 for description). Atoms with highlighted '+' sign within the unit cell form the basis for a particular parameter.

In the present NN modeling, the OVs are linearly combined and squashed by a sigmoid function to form the latent variables (LVs) for the hidden layer which are in turn linearly combined again and squashed to predict the value of the target variable EA. Figure 4-8 depicts the network predictive capability of the 85 (OVs) – 3 (hidden layer nodes) – 1 (EA) layout NN models. The random holdback partitioning was carried out 6 times in order to sample different combinations of training and validation sets. Based on the collected validation statistics, EA for pre-determined bottleneck pathway within the tavorite $LiMXO_4F$ structure can be reasonably predicted by using 3 hidden layer nodes as shown by the best model (DN4); the validation step metrics are R^2 = 0.98 and RMSE = 5.27 x 10^{-2} eV, respectively. The fitting quality for the training and validation steps for the final NN model is shown in Fig. 4-9.

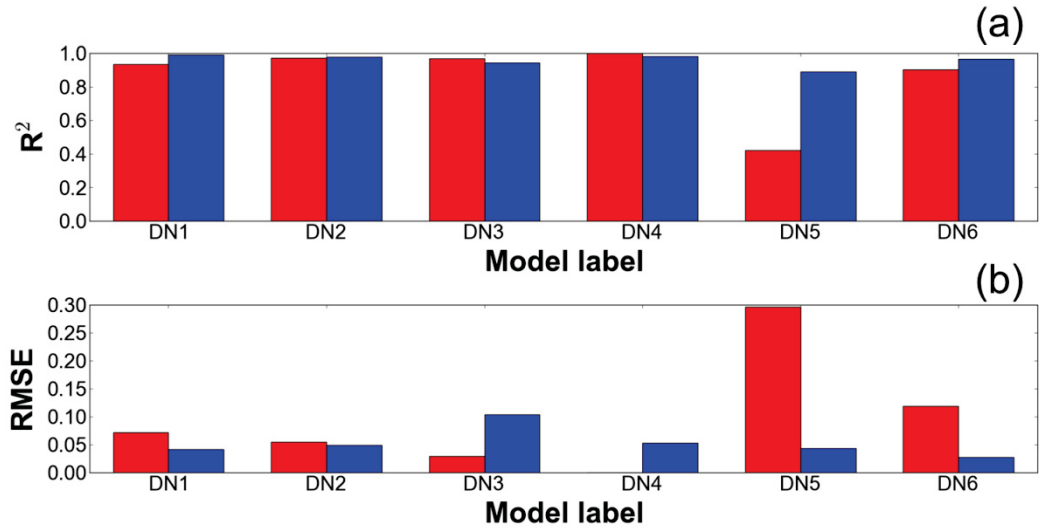

Figure 4-8. Validation statistics for 3-hidden-node NN-based EA prediction models with different training orders (combination of training and validation sets): (a) coefficient of determination R^2 and (b) RMSE values during training (in red) and validation (in blue).

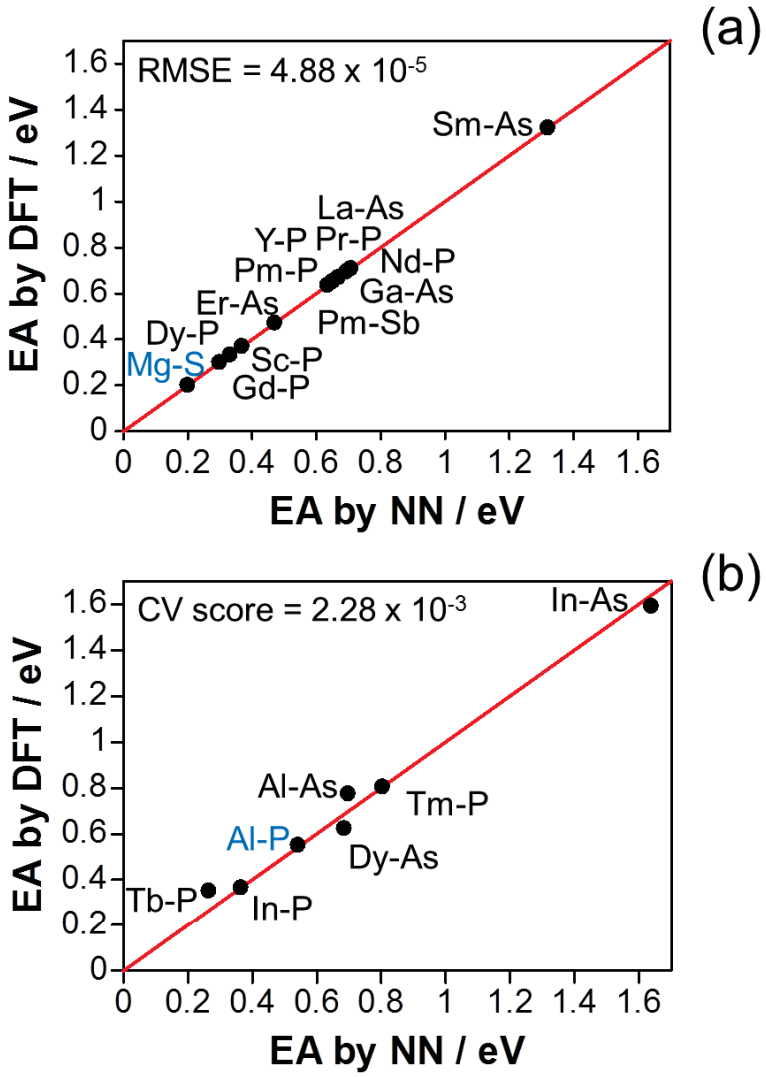

Figure 4-9. Fitting quality of the final NN model (DN4) for EA prediction during a) training and b) validation steps, respectively. Blue points represent composition with published experimental data in ICSD.

Once an acceptable EA prediction model from NN training and validation is determined, EA values for the rest of the compositions can now be predicted at a stroke. Figure 4-8 plots the predicted EA values of the sampled compositions which are sorted according to X cation type. An obvious observation here is the poor correlation of EA with both M and X ionic size parameter. For the screening procedure, candidate materials are determined if their EA values could satisfy the limit condition ≤ 0.30 eV; this is based on the activation energy of perovskite-type (Li, La)TiO_3 which has one of the highest experimental Li ion conductivity value of all the oxides (1×10^{-3} S/cm at 300 K) [38]. Promising compositions, as predicted by the model, include $LiGaPO_4F$ (0.10 eV), $LiGdPO_4F$ (0.30 eV), $LiNdSbO_4F$ (0.15 eV), $LiPrSbO_4F$ (0.23 eV), $LiCeSbO_4F$ (0.10 eV), $LiLaSbO_4F$ (0.20 eV), $LiMgSO_4F$ (0.20 eV), $LiSrTeO_4F$ (0.10 eV), and $LiBaSO_4F$ (0.10 eV). Among these, only the composition $LiMgSO_4F$ (#281119) has been documented in ICSD while the rest are novel compositions.

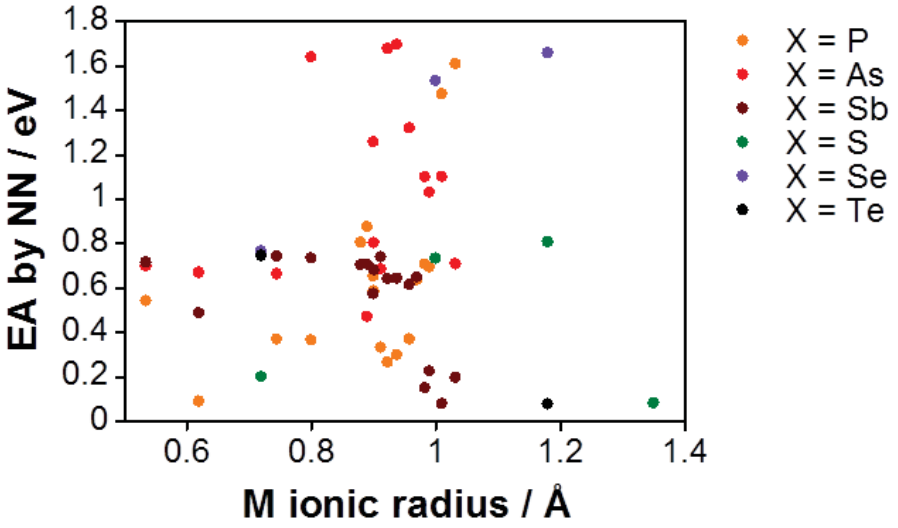

Figure 4-10. NN model-predicted EA for different $LiMXO_4F$ compositions sorted with respect to X cation type.

Aside from the screening of the $LiMXO_4F$ search space, as a part of further characterization, it is also worthwhile to determine the degree of association of the OVs to the value of EA since these insights are especially useful when formulating motivations during material design. NN model incorporates interactions, as necessary, and detecting and interpreting them would not be straightforward due to nonlinearity effects from sigmoid function activation. To qualitatively assess specific interactions, the causal index (CI) plot for the final NN model (DN4) for EA is constructed as displayed in Figure 4-9. In the figure, the main increase in EA is attributed, and by far the largest, to the increase in variable ecn4 (effective coordination number of M cation) with CI value of +2.48 while the main decrease in EA is contributed by the variable di4 (distortion index of the M octahedron) with CI value of -3.15. The strong interaction effects of these two variables with EA can be rationalized by the fact that both of them are direct descriptors of the evaluated path which passes through the MO_4F_2-MO_4F_2 octahedral face pair (see Figure 4-5d). Meanwhile, contributions from the majority of OVs that belong to ion Bader charges (CI values in the range -0.60 – +0.95) and ion Born effective charges (CI values in the range -0.73 – +0.60) are noticeably small, this implies some multicollinearity issues among them, thus leading their weights to be eventually dragged down near to zero by the imposed penalty term (equation 4-23) during the error minimization step. In addition, OVs which are non-varying within the search space of interest are essentially pruned as well in the final model by the said penalty term. An example of this is the Bader charge for Li cations (bader15 and bader16 with CI values of -0.11 and +0.16, respectively), which essentially remained as +1 for all compositions. The reduction of the CI values for the strongly collinear and unimportant inputs is a crucial feature of the present NN model.

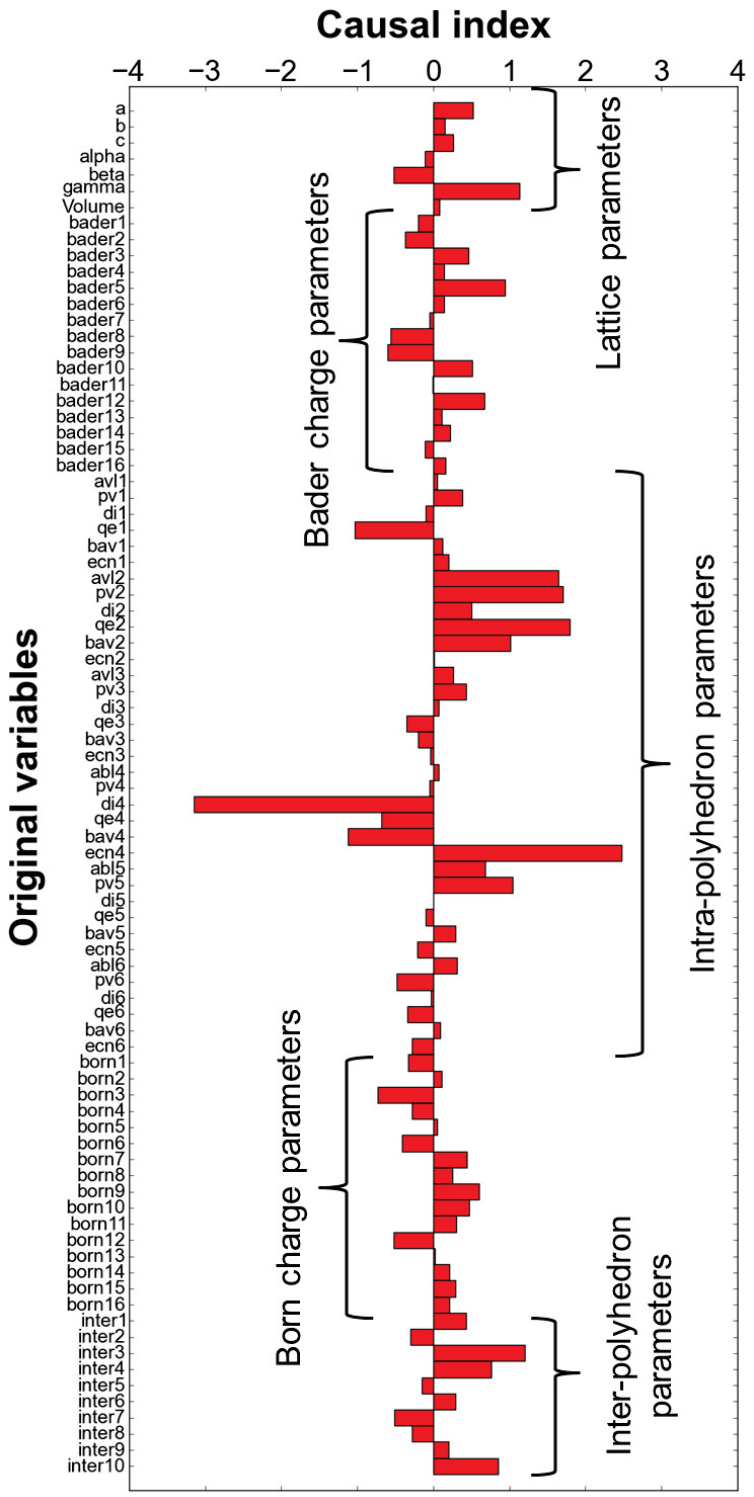

Figure 4-11. Causal index plot of 85 original variables (OVs) taken from the final NN prediction model (DN4) for EA (see Table 4-2 for OV description).

4-5. Conclusions

In summary, a robust model for the prediction of the Li ion hopping energies (EAs) within the tavorite-type $LiMXO_4F$ search space was successfully formulated using a combination of *ab initio*-based methods and NN technique. Specifically, the following results are determined in the study:

1) The strong degree of covalency in the X-O bond which minimizes the interaction for the migrating Li with the lattice, as the electron cloud from oxide ion in MO_4X_2 (c.f. path 2) are drawn more towards $(XO_4)^{2-}$ polyanion, is suggested as one of the critical factors to EA variation.
2) Promising compositions with low EA values (< 0.30 eV) include the ICSD-reported material $LiMgSO_4F$ (0.20 eV), and novel compositions such as $LiGaPO_4F$ (0.10 eV), $LiGdPO_4F$ (0.30 eV), $LiNdSbO_4F$ (0.15 eV), $LiPrSbO_4F$ (0.23 eV), $LiCeSbO_4F$ (0.10 eV), $LiLaSbO_4F$ (0.20 eV), $LiSrTeO_4F$ (0.10 eV), and $LiBaSO_4F$ (0.10 eV).
3) The main increase in EA is attributed to the increase in variable ecn4 (effective coordination number of M cation) while the main decrease in EA is contributed by the variable di4 (distortion index of the M octahedron).

4-6. Future work and direction

The following points are the suggested for the future work of the study:

1) Systematic survey of suitable dopants (low solution energies) for the identified candidate tavorite-type $LiMXO_4F$ solid electrolytes in order to activate their intrinsic fast Li ion conduction.
2) Computational phase stability studies of identified candidate tavorite-type $LiMXO_4F$ compositions.

4-7. Chapter references

1. B. L. Ellis, W. R. M. Makahnouk, Y. Makimura and L. F. Nazar, Nat. Mater., 2007, 6, 749.
2. T. N. Ramesh, K. T. Lee, B. L. Ellis and L. F. Nazar, Electrochem. Solid State Lett., 2010, 13, A43.
3. T. A. Kerr, J. Gaubicher and L. F. Nazar. Electrochem, Solid State Lett., 2000, 3, 460.
4. N. Marx, L. Croguennec, D. Carlier, A. Wattiaux, F. Le Cras, E. Suard and C. Delmas, Dalton Trans., 2010, 39, 5108.
5. R. K. B. Gover, P. Burns, A. Bryan, M. Y. Saidi, J. L. Swoyer and J. Barker, Solid State Ionics, 2006, 177, 2635.
6. F. Zhou, X. M. Zhao and J. R. Dahn, Electrochem. Commun., 2009, 11, 589.
7. N. Recham, J. N. Chotard, J. C. Jumas, L. Laffont, M. Armand and J. M. Tarascon, Chem. Mater., 2010, 22, 1142.
8. R. Tripathi, G. R. Gardiner, M. S. Saiful, L. F. Nazar, Chem. Mater., 2011, 23 2278.
9. T. Mueller, G. Hautier, A. Jain and G. Ceder, Chem. Mater., 2011, 23, 3854.
10. V. I. Simonov and N. V. Belov, Kristallografiya, 1958, 3, 429.
11. L. Sebastian, J. Gopalakrishnan and Y. Piffard, J. Mater. Chem., 2002, 12, 374.
12. K. Hornik, Neural Networks, 1989, 2, 359.
13. G. Kresse and D. Joubert, Phys. Rev. B, 1998, 59, 1758.
14. G. Kresse and J. Furthmüller, Phys. Rev. B, 1996, 54, 11169.
15. G. I. Csonka, J. P. Perdew, A. Ruzsinszky, P. H. T. Philipsen, S. Lebègue, J. Paier, O. A. Vydrov and J. G. Ángyán, Phys. Rev. B, 2009, 79, 155107.
16. ICSD, Inorganic Crystal Structure Database; http://icsd.fizkarlsruhe.de/icsd/, 2006.
17. X. Gonze and C. Lee, Phys. Rev. B, 1997, 55, 10355.
18. H. Jonsson, G. Mills and K. M. Jacobsen, in B.J. Berne, G. Ciccotti, D.F. Coker (Eds.), Classical and Quantum Dynamics in Condensed Phase Simulations, World Scientific, Singapore, 1998.
19. The value of η at each training step is used to compute the direction in which each node weight can be changed to arrive at a more correct output; a value closer to 1. Although it can lead to faster convergence, it can also increase the risk of getting trapped at a local minimum. In this study, a conservative a value of 0.1 is used when updating node weights at every iteration.
20. M. Hassoun, in Fundamentals of Artificial Neural Networks, M.I.T. Press, Cambridge, MA., 1995.
21. H. Zhang, W. Wu, F. Liu and M. Yao, IEEE T. Neural Networ., 2009, 20, 1050.
22. S.-J. Kim, K. Koh, M. Lustig, S. Boyd and D. Gorinevsky, IEEE J. Sel. Topics

Signal Process., 2007, 1, 606.
23. K. Fukumizu and S. Amari. Neural Networks, 2000, 13, 317.
24. K. Baba, I. Enbutu and M. Yoda, in Proceedings of the International Joint Conference on Neural Networks, 1990, 3, 155.
25. D. Morgan, A. Van Der Ven and G. Ceder, Electrochem. Solid State Lett., 2004, 7 A30.
26. M. S. Islam, D. J. Driscoll, C. A. J. Fisher and P. R. Slater, Chem. Mater., 2005, 17, 5085.
27. B. Kang and G. Ceder, Nature Lett., 2009, 458, 190.
28. W. Zhong, R. D. King-Smith and D. Vanderbilt, Phys. Rev. Lett., 1994, 72, 3618.
29. P. Ghosez, J.-P. Michenaud and X. Gonze, Phys. Rev. B, 1998, 58, 6224.
30. M. Veithen and P. Ghosez, Phys. Rev. B, 2002, 65, 214302.
31. R. Jalem, T. Aoyama, M. Nakayama and M. Nogami, Chem. Mater., 2012, 24, 1357.
32. T. Rajkumar, M. Nakayama and M. Nogami, Solid State Commun., 2010, 150, 693.
33. R. Kutner, Phys. Lett., 1981, 81, 239.
34. A. Van Der Ven and G. Ceder, J. Power Sources, 2001, 97-98, 529.
35. M. D. Levi, G. Salitra, B. Markovsky, H. Teller, D. Aurbach, U. Heider and L. Heider, J. Electrochem. Soc., 1999, 146, 1279.
36. Y. I. Jang, B. J. Neudecker and N. J. Dudney, Electrochem. Solid-State Lett., 2001, 4, A74.
37. K.T. Fehr, R. Hochleitner, E. Schmidbauer and J. Schneider, Phys. Chem. Miner., 2007, 34, 485.
38. Y. Inaguma, C. Liquan, M. Itoh, T. Nakamura, T. Uchida, H. Ikuta and M. Wakihara, Solid State Commun., 1993, 86, 689.

Chapter 5. Summary

5-1. Significance of this thesis

Oftentimes, it takes years of research efforts to identify a suitable material for an intended application and optimize it for commercial use. The battery field is no exception to this and progress has been indeed slow due to the vast combinatorial space of chemistries involved in materials design. This thesis develops and argues solutions that would promote a paradigm shift in new battery materials discovery, selection, and evaluation by replacing the conventional trial-and-error approach with more targeted search procedures driven by *ab initio*-based computational modeling and materials informatics. The first topic in this thesis introduces a method of finding the most stable structure for a given starting composition without any *a priori* assumption about the structure itself (except for the elemental constituents); this is the so-called composition-to-structure path solution to materials design. The second topic deals with screening large chemical search spaces of a given structure with a target property-based criterion; this can be referred to as the property-to-composition path solution. These studies highlight solutions to the previously mentioned demerits (see Table 2, section 1-4 of Chapter 1) regarding composition-to-structure and property-to-composition (structure) paths related to new materials search. Overall, the solutions implemented can be easily extended to other systems.

5-2. Achievement of this thesis

In Chapter 2, the evolutionary approach for exploring energy landscapes has been successfully used to determine thermodynamic global minimum and local minimum energy structures for a given composition in cathode Li_xCoO_2. Thermodynamic ground states at x = 1 (layered O3 structure) and x = 0.5 (spinel structure), which have been confirmed experimentally and are reported, were successfully predicted, thus validating the reliability of the present approach. Moreover, new and unreported phases below $x < 0.5$ were predicted to be thermodynamically stable configurations. These phases are

characterized by 1x1 (rutile-like), 1x2 (ramsdellite-like), and 1x3 (ramsdellite-like) tunnels for Li atoms. Also, the method can systematically study reaction routes which could be critical for battery operation.

Meanwhile, chapters 3 and 4 demonstrated the efficient screening of the olivine $LiMXO_4$ and the tavorite $LiMXO_4F$ search spaces, respectively, for solid electrolyte application. In those chapters, accurate *ab initio*-based calculations were combined with materials informatics in order to build a target property-based prediction model within a reasonable tradeoff in accuracy. The search criterion used is a material property which is crucial for Li ionic conductivity: the Li ion hopping energy (EA). According to the trained and validated prediction models, potential solid electrolytes (<0.30 eV) within the $LiMXO_4$ search space include $LiMgAsO_4$, $LiScGeO_4$, $LiInGeO_4$, and $LiMgPO_4$, and virtual compositions such as Li(group 13)XO_4 and $LiCaXO_4$. For the $LiMXO_4F$ search space, promising compositions are $LiGaPO_4F$, $LiGdPO_4F$, $LiNdSbO_4$, LiPrSbO4F, $LiCeSbO_4F$, $LiLaSbO_4F$, $LiSrTeO_4F$, and $LiBaSO_4F$. In addition, the specific methods used (multivariate partial least squares and neural networks) also offer another advantage, i.e., the transformation of high dimensional structure-related data into a human readable form that could provide useful insights that could be tested and checked during materials design.

5-3. Future directions of this work

Ultimately, it would be beneficial if a database that organizes the generated and future data from the implementations introduced in this thesis can be constructed and made accessible to the battery community. This collection of materials datasets have the potential to extend its reach and application to other communities and could promote new collaborative approaches for materials discovery, selection, and evaluation. Also, this database should allow its users to contribute back to spur rapid development. This can be done by: i.) opening a web-based forum where users can freely interact and exchange information, ii.) being able to report issues or errors, and iii.) developing tools for analysis and data extraction and interfacing them with the database.

Meanwhile, it is also important to highlight some of the limitations and disadvantages of the proposed schemes in this thesis work that needs to be addressed in the future.

In Chapter 2, the following issues need to be addressed:

1) One of the restrictions for the combined *ab initio* method + evolutionary algorithm is the dimensionality itself. Although the energy calculation part is sufficiently accurate with *ab initio* method, this level of accuracy has the drawback of increasing computational time. Hence, the approach works well with dimensionalities below 100-200, beyond that the curse of dimensionality becomes increasingly dominant.
2) Since one of the main search criteria for the most stable configuration is the degree of order of the structure, *ab initio* + evolutionary algorithm finds it difficult to predict aperiodic and disordered systems.
3) Energy landscapes with an overall shape such as single-funnel landscapes are much more amenable for evolutionary method than multifunnel or, even worse, featureless energy landscapes.

In chapters 3 and 4, the following issue needs to be addressed:

1) The combined *ab initio* + materials informatics approaches developed in this thesis work is limited to the compositional search or screening from a given host structure and cannot be used for the simultaneous evaluation of multiple structure types or partial substitutions. New techniques should be developed for such purposes.

Appendix [1-3]

The use of computational modeling has become important in increasing the basic understanding not only of underlying scientific phenomena in any given experimental findings, but also of various fundamental processes and chemical reactions. Figure S-1 shows the hierarchy in lengthscales and timescales of different computational methods that are currently employed for simulating materials. At the order of 10^{-10} m (1 Å) and 10^{-15} – 10^{-12} s (fs to ps), *ab initio* calculation in DFT framework provides relevant predictions of crystal structure, electronic energetics, and vibrational frequencies. This complements the explanation of temperature and concentration dependence of chemical reaction rates (transition state theory) and atomistic molecular dynamics of materials which commonly proceed in the range of 10^{-9} to 10^{-6} m (nm to μm) and 10^{-9} to 10^{-6} s (ns to μs). Subsequently, access to rate constants and thermodynamic properties allows for macroscopic scale studies (e.g., local microstructures and system morphologies) with standard analytical continuum approaches such as microkinetics, kinetic Monte Carlo, and transport modeling. Finally, these methods operating at larger lengthscales and timescales reveal mechanistic insights and offers validation into the actual performance observed from the material of interest.

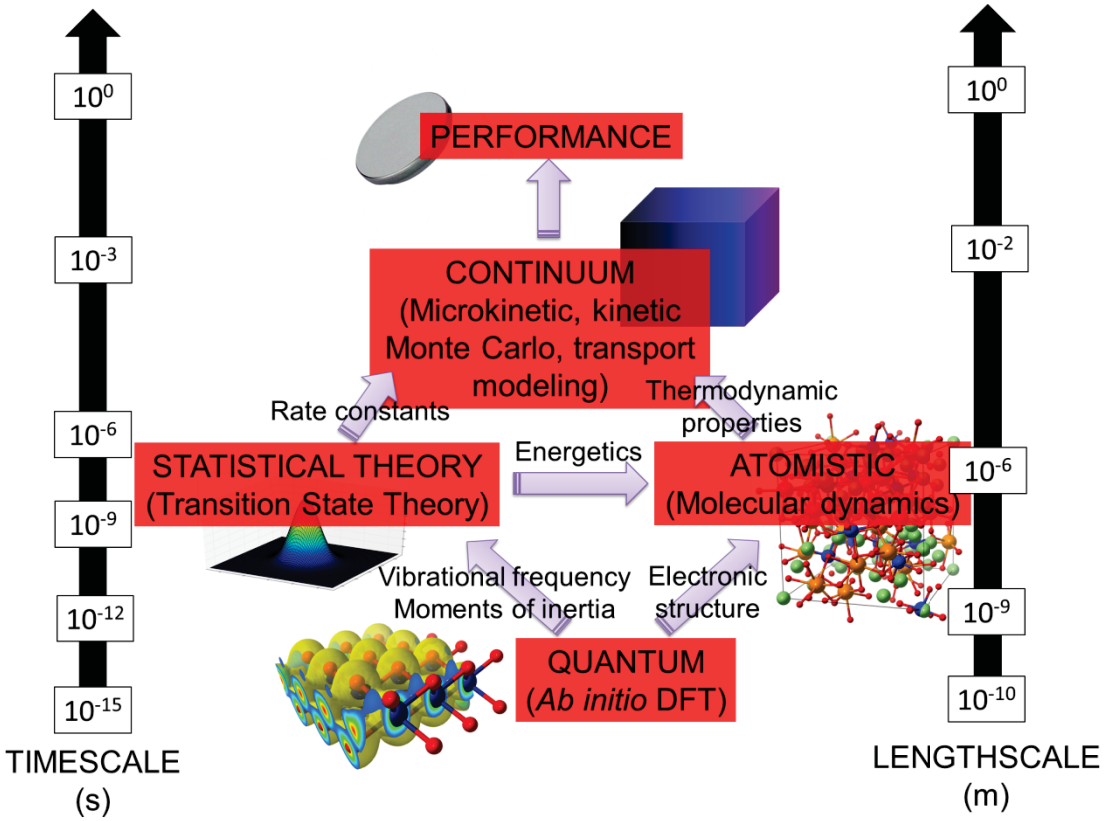

Figure S-1. Computational methods at different timescales and lengthscales for simulating battery materials.

1-2-1. *Ab initio* calculation

The ultimate goal of most *ab initio*-based methods is the approximate solution of the time-independent, non-relativistic Schrödinger equation:

$$\hat{H}\Psi_i(\vec{x}_1, \vec{x}_2, \dots, \vec{x}_N, \vec{R}_1, \vec{R}_2, \dots, \vec{R}_M) = E_i\Psi_i(\vec{x}_1, \vec{x}_2, \dots, \vec{x}_N, \vec{R}_1, \vec{R}_2, \dots, \vec{R}_M) \quad (1\text{-}1)$$

where $\hat{H}$ is the Hamiltonian operator for a molecular system consisting of M nuclei and N electrons in the absence of magnetic or electric fields. $\hat{H}$ is the differential operator representing the total energy:

$$\hat{H} = -\frac{1}{2}\sum_{i=1}^{N}\nabla_i^2 - \frac{1}{2}\sum_{A=1}^{M}\nabla_A^2 - \sum_{i=1}^{N}\sum_{A=1}^{M}\frac{Z_A}{r_{iA}} + \sum_{i=1}^{N}\sum_{j>i}^{N}\frac{1}{r_{ij}} + \sum_{A=1}^{M}\sum_{B>A}^{M}\frac{Z_A Z_B}{R_{AB}} \quad (1\text{-}2)$$

Here, A and B run over the M nuclei while i and j denote the N electrons in the system. The first two terms describe the kinetic energy of the electrons and the nuclei, respectively. The symbol ∇_q^2 is the Laplacian operators in cartesian coordinates and M_A is the mass of nucleus A in multiples of the mass of an electron. The remaining three terms represent the potential part of the Hamiltonian and are assigned as the attractive electrostatic interaction between the nuclei and the electrons and the repulsive potential due to the electron-electron and nucleus-nucleus interactions, respectively. r_{pq} (and in a similar case R_{pq}) is the distance between the particles p and q. $\Psi_i(\vec{x}_1, \vec{x}_2, \dots, \vec{x}_N, \vec{R}_1, \vec{R}_2, \dots, \vec{R}_M)$ is the wave function of the i'th state of the system, which depends on the 3N spatial coordinates $\{\vec{r}_i\}$, and the N spin coordinates $\{s_i\}$ of the electrons, which are collectively termed $\{\vec{x}_i\}$ and the 3M spatial coordinates of the nuclei, $\{\vec{R}_I\}$. The wave function Ψ_i contains all information that can possibly be known about the quantum system at hand. Finally, E_i is the numerical value of the energy of the state described by Ψ_i.

The exact solution of this equation, which will then give access to material properties, is not directly solvable, but through a series of sensible approximations, the electronic structure and the total energy can be calculated with sufficient accuracy.

The first approximation to the Schrödinger equation stems from taking advantage of the significant difference between the masses of nuclei and electrons. The practical consequence is that the nuclei move much slower than the electron and therefore, at least to a good approximation, electrons can be considered as moving in the field of fixed nuclei. This is formally called the Born-Oppenheimer approximation. Since the nuclei are considered to be fixed in space and are immobile, their kinetic energy is zero and the potential energy due to nucleus-nucleus repulsion is a constant value. Thus, the complete Hamiltonian in equation 1 can be reduced to the so-called electronic Hamiltonian of the form:

$$\hat{H}_e = -\frac{1}{2}\sum_{i=1}^{N}\nabla_i^2 - \sum_{i=1}^{N}\sum_{A=1}^{M}\frac{Z_A}{r_{iA}} + \sum_{i=1}^{N}\sum_{j>i}^{N}\frac{1}{r_{ij}} = \hat{T} + \hat{V}_{Ne} + \hat{V}_{ee}. \quad (1\text{-}3)$$

The solution of the Schrödinger equation with $\hat{H}_e$ is the electronic wave function Ψ_e and the electronic energy E_e. Ψ_e depends on the electron coordinates, while the nuclear coordinates enter only parametrically and do not explicitly appear in Ψ_e. The total energy E_{total} is then the sum of E_e and the constant nuclear repulsion term, i.e.:

$$\hat{H}_e\Psi_e = E_e\Psi_e \quad (1\text{-}4)$$

and

$$E_{total} = E_e + \sum_{A=1}^{M}\sum_{B>A}^{M}\frac{Z_A Z_B}{r_{AB}} \quad (1\text{-}5)$$

The attractive potential exerted on the electrons due to the nuclei (the expectation value of the second operator $\hat{V}_{Ne}$ in equation 3 is the external potential in density functional theory, and will be described in details in the following section. It should be noted though that this external potential is not necessarily limited to the nuclear field but may include external magnetic or electric fields, etc.

Unfortunately, there is no strategy yet developed to solve the Schrödinger equation exactly, especially for determining Ψ_i. However, there is a recipe for systematically approaching the wave function of the ground state Ψ_0, i.e., the state which delivers the lowest energy E_0. This recipe is called the variational principle which states that the energy computed from a guessed Ψ is an upper

bound to the true ground state energy E_0:

$$E_0 = \min_{\Psi \to N} E[\Psi] = \min_{\Psi \to N} \langle \Psi | \hat{T} + \hat{V}_{Ne} + \hat{V}_{ee} | \Psi \rangle \quad (1\text{-}6)$$

where $\Psi \to N$ indicates that Ψ is an allowed N-electron wave function. A search over all acceptable functions is obviously an impossible task. Variational principle can be applied to subsets of all possible functions and from there best approximation to the exact wave function can be obtained. However, the exact wave function itself cannot be identified when restricting the search to a subset unless it is included in the subset, which in turn is an extremely improbable case. The ground state energy then becomes a functional of the number of electrons N and the nuclear potential V_{ext}:

$$E_0 = E[N, V_{ext}] \quad (1\text{-}7)$$

Another approximation which serves as the corner stone of almost all conventional wave function-based *ab initio*-based methods is the Hartree-Fock approximation. As previously implied, it is impossible to search through all acceptable N-electron wave functions. In the Hatree-Fock scheme, a suitable subset is defined, which consists of approximating the N-electron wave function by an antisymmetrized product of N one-electron wave functions $\chi_i(\vec{x}_i)$. This product is called a Slater determinant, Φ_{SD}:

$$\Phi_{SD} = \frac{1}{\sqrt{N!}} \det\{\chi_1(\vec{x}_1)\ \chi_2(\vec{x}_2) \dots \chi_N(\vec{x}_N)\} \quad (1\text{-}8)$$

where the one-electron functions $\chi_i(\vec{x}_i)$ are called spin orbitals, and are composed of a spatial orbital $\phi_i(\vec{r})$ and one of the two spin functions, $\alpha(s)$ or $\beta(s)$. However, the relationship between the spatial distribution of the electrons as provided by the electron density and their velocities is difficult to establish, thereby leading to the calculation of kinetic energy with very poor accuracy. The Kohn-Sham approach solves this problem by concentrating on computing as much as can be the true kinetic energy. The remainder of the contribution to the kinetic energy is then dealt with in an approximate manner and combined with the exchange-correlation term. Instead of interacting electrons, a non-interacting

reference system is used whereby an effective potential is introduced into the Hamiltonian:

$$\hat{H}_S = -\frac{1}{2}\sum_i^N \nabla_i^2 + \sum_i^N V_S(\vec{r}_i) \quad (1\text{-}9)$$

This Hamiltonian operator does not contain contributions from electron-electron interactions, the ground state wave function represented by a Slater determinant will have to be switched from Φ_{SD} and χ to Θ_S and φ, respectively, in order to underline the new quantities:

$$\Theta_S = \frac{1}{\sqrt{N!}}\det\{\varphi_1(\vec{x}_1)\ \varphi_2(\vec{x}_2) \dots \varphi_N(\vec{x}_N)\} \quad (1\text{-}10)$$

1-2-2. Density functional theory

Density Functional Theory (DFT) is presently the most successful and the most promising approach to compute the electronic structure of matter. In DFT, the system of interacting electrons is mapped onto an effective non-interacting system with the same total density. The ground-state energy of an N-electron system is a function only of the electron density $\rho(\vec{r})$. The electrons are represented by one-body wave functions, satisfying the Schrödinger-like equations given by:

$$\left[-\nabla^2 + V_N(\vec{r}) + V_c[\rho(\vec{r})] + V_{xc}[\rho(\vec{r})]\right]\Psi_i(\vec{r}) = E_i\Psi_i(\vec{r}),\ i = 1,2,\dots,N \quad (1\text{-}11)$$

The first term stands for the kinetic energy of a system of non-interacting electrons, the second is the potential due to all nuclei, the third is the classical Coulomb energy (Hartree term), and the fourth is the exchange and correlation potential which contains the non-classical effects of self-interaction correction, exchange and correlation, and a portion belonging to the kinetic energy. The exact form of this is fourth term is unknown and is approximated, one approach for determining this is through generalized gradient approximation (GGA) which denotes the form for functionals appropriate for slowly varying densities; the exchange-correlation energy is:

$$E_{xc}^{GGA}[n_\uparrow, n_\downarrow] = \int d^3r f(n_\uparrow, n_\downarrow, \nabla n_\uparrow, \nabla n_\downarrow) \quad (1\text{-}12)$$

where $n_\uparrow$ and $n_\downarrow$ are spin densities and *f* represents the functionals.

Most *ab initio*-based methods also use functions called pseudopotentials which explicitly include only valence electrons in the calculation and replace the nuclear potential and chemically inert core electrons with an effective potential. This leads to the valence Kohn-Sham equations of the form:

$$[T + V(r, r') + V_H(n_v) + V_{xc}(n_v)]\phi_i^v(r) = \epsilon_i \phi_i^v(r) \quad (1\text{-}13)$$

The pseudopotential $V(r, r')$ has to be chosen such that the main properties of the atom are reproduced. This approximation is assumed valid provided that the core electrons do not participate in chemical bonding. Since pseudo-wave functions are smooth and modeless, plane wave basis sets can be used which allows for a straightforward calculation of forces acting on atoms and stresses on the unit cell according to the Hellmann-Feynman theorem:

$$F = -\langle \Psi_0 \left| \frac{\partial H}{\partial R} \right| \Psi_0 \rangle \quad (1\text{-}14)$$

The pseudopotential form is illustrated in Figure S-2.

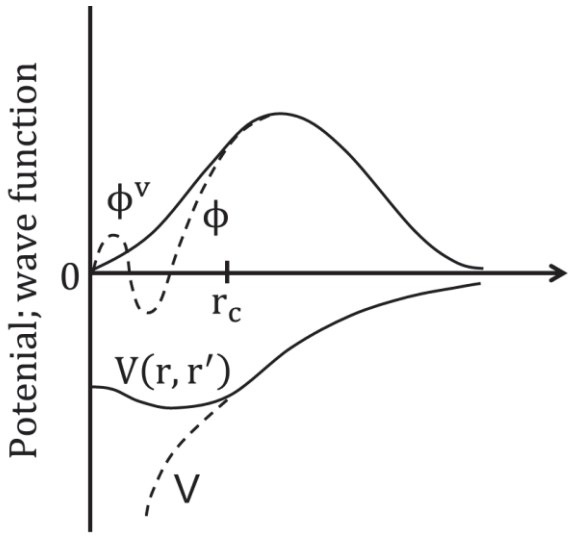

Figure S-2. Schematic representation of pseudopotential $V(r, r')$, pseudo-orbital function ϕ^v. The all-electron potential V and orbital function ϕ, respectively, are altered inside a core radius r_c.

1-2-3. Crystal structure optimization

As there is no analytic solution to the electronic Schrödinger equation, a simpler wave function is instead used as suggested in the Hartree-Fock approximation. This then allows for a numerical solution to the problem. The self-consistent field (SCF) method is used for this purpose which is an iterative method that involves selecting an approximate Hamiltonian, solving the Schrödinger equation to obtain a more accurate set of orbitals, and then solving the Schrödinger equation again with these until the results converge or meet some predefined threshold. This SCF scheme is shown in more details in the flowchart in Figure S-3.

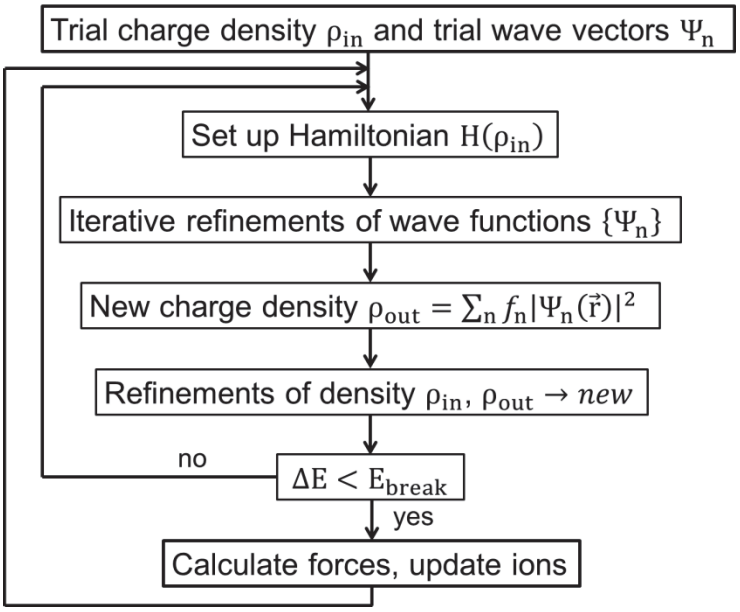

Figure S-3. Flowchart showing the self-consistent field (SCF) method for the solution of electronic Schrödinger equation.

1-2-3. Li ion migration by nudged elastic band (NEB) method

One target property that is used as a criterion for fast Li ion conduction is the migration energy barrier associated with the diffusing Li ions within their host structures. The determination of this energy barrier can be imagined as a problem related to the identification of a lowest energy pathway for a rearrangement of a group of atoms from one stable configuration to another. The potential energy maximum along this path is the saddle point energy which gives the migration energy barrier or the transition state (Figure S-4). The actual distance between two stable sites (Site 1 and Site 2) is the migration reaction coordinate.

A method for finding the minimum energy path (MEP) between a pair of stable states is the nudged elastic band (NEB) method as shown in Figure S-5. In the NEB method, a string of images or geometric configurations is used to describe the reaction pathway. These configurations are connected by spring forces to ensure equal spacing along the path and are relaxed to the MEP through a force projection scheme. If atoms get close to each other, a geometric repulsive force is used to push these atoms apart, resulting in a band with lower initial forces. Spring forces act along the band and the potential forces act perpendicular to the band. In order to make the projection of these forces, the tangent along the path $\hat{\tau}_i$, which connects to the neighboring configuration, is defined. The NEB force $\vec{\mathrm{F}}_i^{\mathrm{NEB}}$ on configuration i contains two independent components:

$$\vec{\mathrm{F}}_i^{\mathrm{NEB}} = \vec{\mathrm{F}}_i^{\perp} + \vec{\mathrm{F}}_i^{\mathrm{S}||} \tag{1-24}$$

where $\vec{\mathrm{F}}_i^{\perp}$ is the force component perpendicular to the band due to the potential:

$$\vec{\mathrm{F}}_i^{\perp} = -\nabla(\vec{\mathrm{r}}_i) + \nabla(\vec{\mathrm{r}}_i) \cdot \hat{\tau}_i \hat{\tau}_i, \tag{1-25}$$

and $\vec{\mathrm{F}}_i^{\mathrm{S}||}$ is the parallel spring force to the band:

$$\vec{\mathrm{F}}_i^{\mathrm{S}||} = k(|\vec{\mathrm{r}}_{i+1} - \vec{\mathrm{r}}_i| - |\vec{\mathrm{r}}_i - \vec{\mathrm{r}}_{i-1}|)\hat{\tau}_i \tag{1-26}$$

where k is the spring constant.

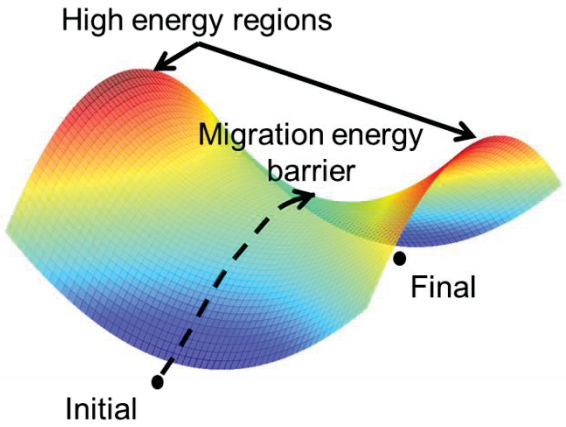

Figure S-4. Sample of potential surface showing the minimum energy path between two stable sites and passing via saddle point (migration energy barrier). Surface portion in blue and red are low energy and high energy regions, respectively.

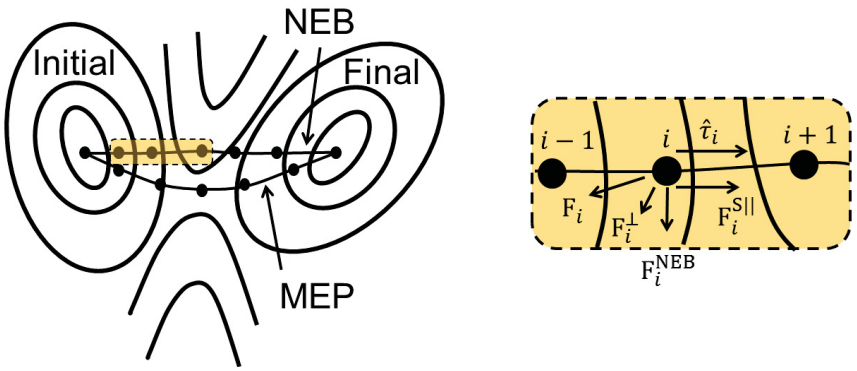

Figure S-5. Schematic illustration of the nudged elastic band (NEB) method. The NEB force F_i^{NEB} has two components: $F_i^{S||}$ which acts along the tangent $\hat{\tau}_i$ and $F_i^{\perp}$ which is a perpendicular force due to the potential. The force F_i is the unprojected force due to the potential.

References

1. D. Frenkel and B. Smit, in Understanding Molecular Simulation: From Algorithms to Applications, Computational Science Series, Volume 1, Academic Press, CA, USA, 2002.
2. W. Koch and M. C. Holthausen, in A Chemist's Guide to Density Functional Theory, Second Edition, Wiley-VCH, Weinheim, DE, 2001.
3. D. Sheppard, R. Terell and G. Henkelman, J. Chem. Phys., 2008, 128, 134106.

Publications related to this thesis

Chapter 2

1. Randy Jalem, Yuhei Mochiduki, Kunihiro Nobuhara, Masanobu Nakayama and Masayuki Nogami
   "Global minimum structure search in Li_xCoO_2 composition using a hybrid evolutionary algorithm"
   Physical Chemistry Chemical Physics, 2012, 14, 37, 13095.

Chapter 3

1. Randy Jalem, Takahiro Aoyama, Masanobu Nakayama and Masayuki Nogami
   "Multivariate Method-Assisted *Ab Initio* Study of Olivine-Type $LiMXO_4$ (Main Group M^{2+}–X^{5+} and M^{3+}–X^{4+}) Compositions as Potential Solid Electrolytes" Chemistry of Materials, 2012, 24, 7, 1357.
2. Randy Jalem, Masanobu Nakayama and Toshihiro Kasuga
   "An Efficient Rule-Based Screening Approach for Discovering Fast Lithium Ion Conductors Using Density Functional Theory and Artificial Neural Network, Journal of Materials Chemistry A, 2013, in press.

Chapter 4

1. Randy Jalem, Masanobu Nakayama and Toshihiro Kasuga
   "Lithium Ion Conduction in Tavorite-Type $LiMXO_4F$ (M-X: Al-P, Mg-S) Candidate Solid Electrolyte Materials"
   Solid State Ionics, 2013, in press.

Publications not related to this thesis

1. Masanobu Nakayama, Randy Jalem and Toshihiro Kasuga
   "Electronic Structure of Spinel-type $LiNi_{1/2}Ge_{3/2}O_4$ and $LiNi_{1/2}Mn_{3/2}O_4$ as Positive Electrodes for Rechargeable Li Ion Batteries Studied by First-Principles Density Functional Theory"
   Solid State Ionics, 2013, in press.
2. Randy Jalem, Yoshihiro Yamamoto, Hiromasa Shiiba, Masanobu Nakayama, Hirokazu Munakata, Toshihiro Kasuga and Kiyoshi Kanamura
   "Concerted Migration Mechanism in the Li Ion Dynamics of Garnet-Type $Li_7La_3Zr_2O_{12}$"
   Chemistry of Materials, 2013, 25, 425.
3. Nguyen Viet Long, Michitaka Ohtaki, Tong Duy Hien, Randy Jalem and Masayuki Nogami
   "A comparative study of Pt and Pt–Pd core–shell nanocatalysts"
   Electrochimica Acta, 2011, 56, 9133.
4. Nguyen Viet Long, Michitaka Ohtaki, Tong Duy Hien, Randy Jalem and Masayuki Nogami
   "Synthesis and characterization of polyhedral and quasi-sphere non-polyhedral Pt nanoparticles: effects of their various surface morphologies and sizes on electrocatalytic activity for fuel cell applications"
   Journal of Nanoparticle Research, 2011, 13, 5177.
5. Randy Jalem, Ryosuke Koike, Yong Yang, Masanobu Nakayama and Masayuki Nogami
   "Electrochemical Characterization of a Porous Pt Nanoparticle Nanocube-Mosaic and Their Electrocatalytic Properties"
   Nano Research, 2011, 4, 746.
6. Nguyen Viet Long, Michitaka Ohtaki, Masaya Uchida, Randy Jalem, Hirohito Hirata, Nguyen Duc Chien and Masayuki Nogami
   "Synthesis and characterization of polyhedral Pt nanoparticles: Their catalytic property, surface attachments, self-aggregation and assembly"
   Journal of Colloid and Interface Science, 2011, 359, 339.
7. K. Tanaka, G. Lakshminarayana, Randy Jalem and Masayuki Nogami
   "Preparation and characterization of proton conducting phosphosilicate glass membranes with different catalyst layers for low-temperature H2/O2 fuel cells"
   Journal of Alloys and Compounds, 2010, 506, 902.

8. Nguyen Viet Long, Nguyen Duc Chien, Masaya Uchida, Takashi Matsubara, Randy Jalem and Masayuki Nogami
"Directed and random self-assembly of Pt-Au Nanoparticles"
Materials Chemistry and Physics, 2010, 124, 1193.
9. Masayuki Nogami, Ryosuke Koike, Randy Jalem, Go Kawamura, Yong Yang and Yukichi Sasaki
"Synthesis of Porous Single-Crystalline Platinum Nanocubes Composed of Nanoparticles"
The Journal of Physical Chemistry Letters, 2010, 1, 568.

Acknowledgments

I would like to express, first and foremost, my deepest and sincerest gratitude to my thesis advisor, Professor Masanobu Nakayama. His persisting support from the intellectual, personal and financial side has fueled me tremendously in finishing this thesis work. His pursuit of scientific knowledge, communication of ideas, and logical yet practical reasoning has inspired me to forge a path of my own in research.

I am grateful to my thesis committee, Professors Yuji Iwamoto and Kenichi Kakimoto, for their useful insight and suggestions which led to the significant improvement of my thesis.

I am also grateful to Prof. Toshihiro Kasuga for his support in my research work.

NITECH is also acknowledged for the financial support.

I would like to thank Prof. Masayuki Nogami for accepting me in his laboratory during my Master's study.

I would like to personally thank all the present and previous members of Nakayama group for sharing their knowledge, talent and ideas, and for engaging with me in fruitful discussions. I appreciate the efforts made by Mr. Hiromi Oshima and Mr. Hiromasa Shiiba as they patiently taught me how to carry out calculations and modeling of materials. I also thank the rest of members, namely: Mr. Takashi Okajima, Mr. YoshihiroYamamoto, Mr. Suguru Chizawa, Mr. Taisuke Tsushima, Mr. Takahiro Aoyama, Mr. Tomoake Nakamura, Mr. Satoshi Tokuda, Mr. Yuhei Mochiduki, Mr. Yuta Hara, Mr. Masato Miwa, Mr. Takuya Horie, Mr. Masayuki Kato, Mr. Shota Hotta, Mr. Hiroyuki Ishizaki, Ms. Sakiho Wakimura, Mr. Yasuyuki Morishita, Mr. Ryosuke Natsume, Mr. Takayuki Oshiro, Mr. Norimitsu Nishimura, and Mr. Wen-Zhong Xie.

I warmly thank Ms. Kiyoko Furumai and Ms. Kumiko Murase for their help and assistance during the entirety of my stay in Nakayama group.

Finally, to my family, I dedicate this work to them, as they were the ones who were always there, believing in my dreams and constantly encouraging me to finish this chapter in my life's journey.